1-1-2014

Engineered Materials to Measure and Regulate Cell Mechanotransduction

Brandon Lou Blakely
University of Pennsylvania, brandon.l.blakely@gmail.com

Engineered Materials to Measure and Regulate Cell Mechanotransduction

Abstract
The extracellular environment plays a key role in a wide array of cellular functions including migration, tissue formation, and differentiation. This thesis overviews the design of a molecular sensor to measure cellular forces and a hydrogel system to engineer angiogenic sprouting. We developed molecular force probes (FPs) that report traction forces of adherent cells with high spatial resolution, can be linked to virtually any surface, and do not require monitoring deformations of elastic substrates. FPs consist of DNA hairpins conjugated to fluorophore-quencher pairs that unfold and fluoresce when subjected to specific amounts of force. In chapter two we overview the synthetic strategies to produce these FPs from solid-state synthesis. We then demonstrate the chemical and physical characterization of these FPs. These data show that the FPs can be designed rationally from existing knowledge of the force-responsiveness of DNA hairpins. Chapter three summarizes our methods to affix these FPs to solid substrates to measure cellular traction forces. The silane chemistry to conjugate these FPs to glass coverslips is reported in detail. Then, the results of converting the fluorescence of these FPs to force values is given along with biological validation. We find using this method that cellular tractions are exerted at the distal ends of focal adhesions. In chapter four we present a versatile bioactive PEG hydrogel to study angiogenesis. This material is MMP-degradable and cell-adhesive. We show a microfabrication strategy to micromold these gels to pattern angiogenic sprouting from ex vivo tissue explants.

Degree Type
Dissertation

Degree Name
Doctor of Philosophy (PhD)

Graduate Group
Bioengineering

First Advisor
Christopher S. Chen

Keywords
Adhesion Biology, Angiogenesis, Bioengineering, Biomaterials, Mechanotransduction

Subject Categories
Biomedical | Cell Biology | Engineering

ENGINEERED MATERIALS TO MEASURE AND REGULATE CELL MECHANOTRANSDUCTION

Brandon Lou Blakely

A DISSERTATION

in

Bioengineering

Presented to the Faculties of the University of Pennsylvania

in

Partial Fulfillment of the Requirements for the

Degree of Doctor of Philosophy

2014

Supervisor of Dissertation

_____

Christopher S. Chen

Professor, Bioengineering

Graduate Group Chairperson

_____

Jason A. Burdick, Professor, Bioengineering

Dissertation Committee

Yale E. Goldman, Professor, Physiology

Jason A. Burdick, Professor, Bioengineering

Arjun Raj, Assistant Professor, Bioengineering

ENGINEERED MATERIALS TO MEASURE AND REGULATE CELL MECHANOTRANSDUCTION

For Han

ACKNOWLEDGMENTS

I would like to thank my advisor Chris Chen for his support and guidance through my time earning a PhD. Also, I thank my committee members Dr. Yale Goldman, Dr. Jason Burdick, and Dr. Arjun Raj for their insight and encouragement.

I also thank the researchers whose credit I share for this work: Christoph E. Dumelin from David Liu's lab, Peter C. Anthony and Van K. Nguyen from Steven Block's lab, and Colin K. Choi and Brendon M. Baker from Chris Chen's lab for chapters two and three. Also, I thank Jordan S. Miller, Colette J. Shen, Wesley R. Legant, Jan D. Baranski, and Britta Trappmann for their contributions to the data presented in chapter four.

To past and present lab members of the Chen lab, I also owe special thanks for the supportive environment they fostered. I am especially thankful for the advice and wisdom shared by senior members of the lab: Jordan Miller, Wes Legant, Ravi Desai, Colin Choi, Michele Wozniak, Jeroen Eyckmans, and Britta Trappmann.

My family and friends offered the most important contribution through their love and comfort. My mom and Jack extended their support from across the country. Most importantly, my wife, Han Chen, made all of this possible by being there each and every day. I look forward to continuing to share our lives together.

ABSTRACT

ENGINEERED MATERIALS TO MEASURE AND REGULATE CELL MECHANOTRANSDUCTION

Brandon L. Blakely

Christopher S. Chen

The extracellular environment plays a key role in a wide array of cellular functions including migration, tissue formation, and differentiation. This thesis overviews the design of a molecular sensor to measure cellular forces and a hydrogel system to engineer angiogenic sprouting. We developed molecular force probes (FPs) that report traction forces of adherent cells with high spatial resolution, can be linked to virtually any surface, and do not require monitoring deformations of elastic substrates. FPs consist of DNA hairpins conjugated to fluorophore-quencher pairs that unfold and fluoresce when subjected to specific amounts of force. In chapter two we overview the synthetic strategies to produce these FPs from solid-state synthesis. We then demonstrate the chemical and physical characterization of these FPs. These data show that the FPs can be designed rationally from existing knowledge of the force-responsiveness of DNA hairpins. Chapter three summarizes our methods to affix these FPs to solid substrates to measure cellular traction forces. The silane chemistry to conjugate these FPs to glass coverslips is reported in detail. Then, the results of converting the fluorescence of these FPs to force values is given along with biological validation. We find using this method that cellular tractions are exerted at the distal ends of focal adhesions. In chapter four we present a versatile bioactive PEG hydrogel to study angiogenesis. This material is MMP-degradable and cell-adhesive. We show a microfabrication strategy to micromold these gels to pattern angiogenic sprouting from *ex vivo* tissue explants.

TABLE OF CONTENTS

LIST OF TABLES

LIST OF ILLUSTRATIONS

CHAPTER 1

Introduction

1.1 The Role of Cellular Mechanics in Cell Behaviors

Historically, soluble chemical signals have been investigated for their role in affecting cellular biological processes ranging in scales from enzyme regulation to cellular phenotypes (Dobrescu, 1998). However, cells attach, spread, and remodel their physical environment by generating force, and these forces and the characteristics of the ECM itself are important for cell phenotype (Hynes, 2009). Following actin polymerization-driven lamellipodia protrusion, myosin II contraction of the actin cytoskeleton drives the propulsion of the cell body during migration (Lauffenburger and Horwitz, 1996). The interplay between cell forces and gene regulation underpin crucial developments during tissue formation and embryogenesis including cell sorting, axis formation, tissue folding, and branching (Mammoto and Ingber, 2010). In endothelial cells, the degree of traction forces regulates growth and proliferation (Nelson et al., 2005; Pirone et al., 2006). The magnitude of cellular traction force also acts as a cue for differentiation of stem cells (McBeath et al., 2004). ECM properties influence cellular signaling (Eliceiri and Cheresh, 2001; Short et al., 1998), and genes expressed during tissue formation affect ECM adhesion and degradation (Bell et al., 2001; Su et al., 2008). Using integrins, combinations of heterodimeric (18 α and 8 β) surface-bound subunit proteins, cells bind to the ECM, stimulating or inhibiting proliferation depending on the integrin type (Avraamides et al., 2008; Desgrosellier and Cheresh, 2010; Drake et al., 1995). ECM binding or internal signals activate integrins to cluster. Other signaling molecules are recruited, including focal adhesion kinase (FAK), Src, small GTPases

including RhoA, and Ras within structures known as focal adhesions (FAs) (Avraamides et al., 2008). FAs allow cells to sense environmental stiffness, ligand density and spacing, and dimensionality (Geiger et al., 2009a). In fact, the abnormal expression of $\alpha_V\beta_3$ in tumor endothelium enhances VEGFA signaled sprouting, and this has led to novel anti-cancer therapeutics (Desgrosellier and Cheresh, 2010; Friedlander et al., 1995).

Besides integrins modulating biochemical signaling, cell spreading directly regulates their behavior. Cells plated on different densities of ECM proteins range in shape from rounded, intermediate, and fully spread, corresponding to responses of apoptosis, tissue formation, and proliferation respectively (Folkman and Moscona, 1978; Ingber, 1990; Ingber and Folkman, 1989a). Use of microfabrication technology has allowed the control of cell-shape on islands of saturating levels of ECM protein, where the same trends were observed, establishing cell shape as an important cellular signal (Chen et al., 1997; Dike et al., 1999).

ECM stiffness also plays a role in phenotype. Similar to adhesion, cells on both 2D surfaces of fibronectin (FN) or crosslinked collagen or polyacrylamide gels, to control for ligand density, display a transition from tissue formation to proliferation when cultured on softer (less than 1kPa Young's modulus) versus stiff substrates (>10kPa) (Klein et al., 2009; Kuzuya et al., 1998; Pelham and Wang, 1997; Vailhé et al., 1997). Similar trends arise in 3D gels (Deroanne et al., 2001; Levental et al., 2009; Provenzano et al., 2009).

Many of the effects of ligand density, cell shape, and substrate stiffness are due to the resultant cell-exerted tension. FAs act as a tension dependent bridge between integrins, signaling proteins, and the actin cytoskeleton (CSK) (Berrier and Yamada, 2007; Zhang et al., 2008). The structure of FAs is hierarchical, transitioning from an adhesive layer to a force transmission layer conveying physical information including

tension to cells, suggesting that molecular scale force is an important consideration for their formation and function (Kanchanawong et al., 2010b). The interplay of proliferation and VEGFA-mediated angiogenesis with cell spreading has been linked to RhoA and FAK activity due to CSK tension (Bhadriraju et al., 2007b; Huang et al., 1998; Ingber et al., 1995; Mammoto et al., 2009; Mammoto and Ingber, 2009). Spreading and substrate stiffness also causes cells to increase their contractility both in 2D and 3D contexts, providing evidence that CSK tension mediates the substrate rigidity and spreading phenotype effects (Fu et al., 2010; Legant et al., 2009; Sieminski et al., 2004; Tan et al., 2003). Measuring cellular tension is key to fully understanding a multitude of cell-ECM interactions.

1.2 Physical Basis for Cell Traction Forces

Cells attach and migrate through their environment by exerting forces and sensing the physical characteristics of the ECM. Integrin binding and FAs are the molecular machinery cells used to navigate their surroundings. Upon binding to their target ligands, integrins undergo a conformational change promoting clustering (Burridge and Chrzanowska-Wodnicka, 1996). The binding of ligands recruits FA proteins such as talin, α-actinin, paxillin, vinculin and actin. The clustering in and of itself promotes the recruitment of FA signaling proteins such as FAK and tensin (Miyamoto et al., 1995). Studies culturing cells on surfaces dispersed with gold nanoparticles conjugated with adhesive ligand, allowing one integrin binding per particle, showed that particle spacing, and by extension activated integrin spacing in FAs, of more than 73 nm strongly inhibited proper cell spreading and FA formation (Arnold et al., 2004; Cavalcanti-Adam et al., 2007). Talin binds to the cytoplasmic domain of integrins to both activate integrins and recruit other proteins including vinculin (Calderwood et al., 2013). Vinculin acts a key intermediary between FAs and the actin cytoskeleton and its conformational change is

widely suspected to act as a ‘clutch’ between extracellular tension and actin stress fibers (Grashoff et al., 2010; Hu et al., 2007b). Phosphorylation of paxillin, a binding partner of vinculin, serves to enhance paxillin’s scaffolding function for other FA proteins including FAK (Bellis et al., 1995; Laukaitis et al., 2001; Richardson et al., 1997; Schaller and Parsons, 1995). Besides vinculin, actin binds to several FA proteins, either to provide molecular recourses or due to the different functional purposes of these proteins. For instance α-actinin, in contrast to vinculin’s role in adhesion maturation, helps to recruit actin stress fibers to nascent adhesions (Burridge and Chrzanowska-Wodnicka, 1996). Talin and kindlin are especially important proteins linking integrins to the actin cytoskeleton as they are required for FA formation (Geiger et al., 2009a). In total, these various proteins that comprise FAs act as different functional modules such as integrin signaling, force-induced signaling changes, and an actin binding layer connecting FAs to actin stress fibers (Kanchanawong et al., 2010a).

In addition to generating the forces cells need to migrate, FAs themselves and the cell cytoskeleton respond to these forces to provide cells sensing capabilities of their environment. There is a positive feedback loop between FA formation and the primary force-generating machinery of the cell cytoskeleton: actin polymerization and myosin II motor proteins generating actin sliding (Burridge and Chrzanowska-Wodnicka, 1996). At the leading edge of the cell, the lamellapodia contains the earliest adhesion precursors, focal complexes, which recruit nucleators of actin polymerization such as Arp2/3 and formins mDia1 and mDia2 (Geiger et al., 2009a). These actin polymerization nucleators induce actin branches from preexisting filaments to push the cell membrane outward and are regulated by WAVE/Scar and Wasp signaling (Pollard and Borisy, 2003). Upstream of WAVE/Scare and Wasp are the GTPases Rac and Cdc42 respectively (Vicente-Manzanares et al., 2005). The lamellapodial actin is on the ventral side of the cell

membrane above a less dynamic lamella actin layer, and focal complexes at the cell edge form preceding the application of force by myosin motors in more distal regions of the cell (Giannone et al., 2007). Focal complex formation at the cell edge involves α-actinin templating independent of myosin and suggests that primarily the mechanical force of actin polymerization influences the initiation steps of adhesion formation (Choi et al., 2008; Hu et al., 2007b). The activity of cytoplasmic myosin II is regulated by phosphorylation of myosin light chains (MLC) by MLC kinase (MLCK), and the tails of myosin II associate to form coiled-coiled structures (Sellers, 2000). FA signaling activates the GTPase RhoA and, through its effecters Rho kinase (ROCK) and MLCK, leads to an increase in cellular tension by increasing myosin II activity (Vicente-Manzanares et al., 2005). The balance between Rho and Rac is achieved by differential signaling of integrins in mature adhesions, favoring Rho activity, and nascent adhesions, favoring Rac (DeMali et al., 2003). Myosin driven tension helps recruit FAK, which phosphorylates paxillin to recruit vinculin leading to adhesion maturation (Pasapera et al., 2010). As adhesions mature they become the origin of large bundled actin stress fibers crosslinked with myosin and α-actinin. Initially dorsal stress fibers form, anchored to one adhesion, before evolving into ventral stress fibers, anchored to two adhesions, sometimes reaching nearly the length of the cell and generating large traction forces (Burridge and Wittchen, 2013).

Besides FAs and actin, other elements of the cytoskeleton underlie cells' ability to alter and sense their mechanical environment. The formation of stress fibers is most likely due to isometric tension between their anchors at adhesions evidenced by the enhancement of stress fibers upon pharmacologically disrupting microtubules (Burridge and Chrzanowska-Wodnicka, 1996). This is because other components of the CSK such as microtubules may contribute a resistive compressive force (Ingber, 1997). Integrins

and FA adhesion proteins are also connected to these non-actin CSK structures including intermediate filaments, permitting forces to propagate through long length-scales (Janmey et al., 2009). Further, the crosslinking of actin along with the structural contributions given by microtubules and intermediate filaments give rise to the effect that the CSK is mostly 'strain stiffening' or that the elastic modulus increases with increasing strain (Gardel et al., 2008). Thus cellular tractions impart global effects on both cellular signaling and mechanics.

1.3 Methods to Measure Cellular Traction Forces

The first method to measure cellular traction forces was developed by Albert Harris (Harris et al., 1980) whereby cells were cultured on a cross-linked silicon rubber. The elastic deformations caused by cellular tractions generated wrinkles on the surface. While this study demonstrated that single cells generate pulling forces, quantitation of this phenomenon was crude. To allow more precise force measurements, similar silicone surfaces where fixed at the perimeter to prevent wrinkling while adding beads as fiduciary markers that simultaneously tracked lateral displacements of these silicone surfaces (Lee et al., 1994). Using a molded silicone substrate, Balaban *et al.* were able to measure the forces of single adhesions by observing the deflection of micropatterned molds (Balaban et al., 2001). Such experimental systems allowed the mapping of displacements to calculated traction vector fields, a technique termed traction force microscopy (TFM). Polyacrylamide gels, due to superior optical transparency and the ease of altering the stiffness to physiologic ranges (10-100 kPa) by choosing the crosslinker concentration, supplanted silicone gels (Dembo and Wang, 1999; Stricker et al., 2010). Computational advances made in TFM include transforming the discretized Green's function in Fourier space to simplify the calculations (Sabass et al., 2008) and confocal bead tracking to relax the assumption that tractions are exclusively in-plane of

the gel surface to describe normal cell pulling and compressive forces (Delanoe-Ayari et al., 2010; Franck et al., 2011; Legant et al., 2013). While TFM has emerged as the most widely adopted method to measure forces, these measurements are indirect and necessitate the removal of the cells from the elastic substrate to obtain the unstressed state. This rules out real-time force measurements over longer time-points. Additionally, the inverse of the Boussinesq equations describing the deformation of a half elastic space require computational assumptions to arrive at a unique solution, either that the forces are localized only at visualized adhesions (Balaban et al., 2001; Stricker et al., 2010) or that the solution balances accuracy while minimizing some metric of complexity (Dembo and Wang, 1999; Legant et al., 2013). One approach to measure cell forces directly utilized micro-machined silicon cantilevers to detect the perpendicular dislocation of the levers upon cell binding (Galbraith and Sheetz, 1997). Our lab has established elastomeric micropost array substrates (mPADs) to study and manipulate stiffness for measurements of single cell forces and a macropost system for large cellular aggregates (Fu et al., 2010; Legant et al., 2009; Sniadecki et al., 2007; Sniadecki and Chen, 2007; Tan et al., 2003). This bed of elastic cantilevers provides direct real-time force measurements but constrains the size of the adhesions to the area of the posts. Additionally, FAs possess a notably detailed molecular architecture, but these techniques do not lend an ability to investigate how molecular scale forces impact FA form and function due to a lack of resolution. Some of these methods are overviewed in Figure 1.1.

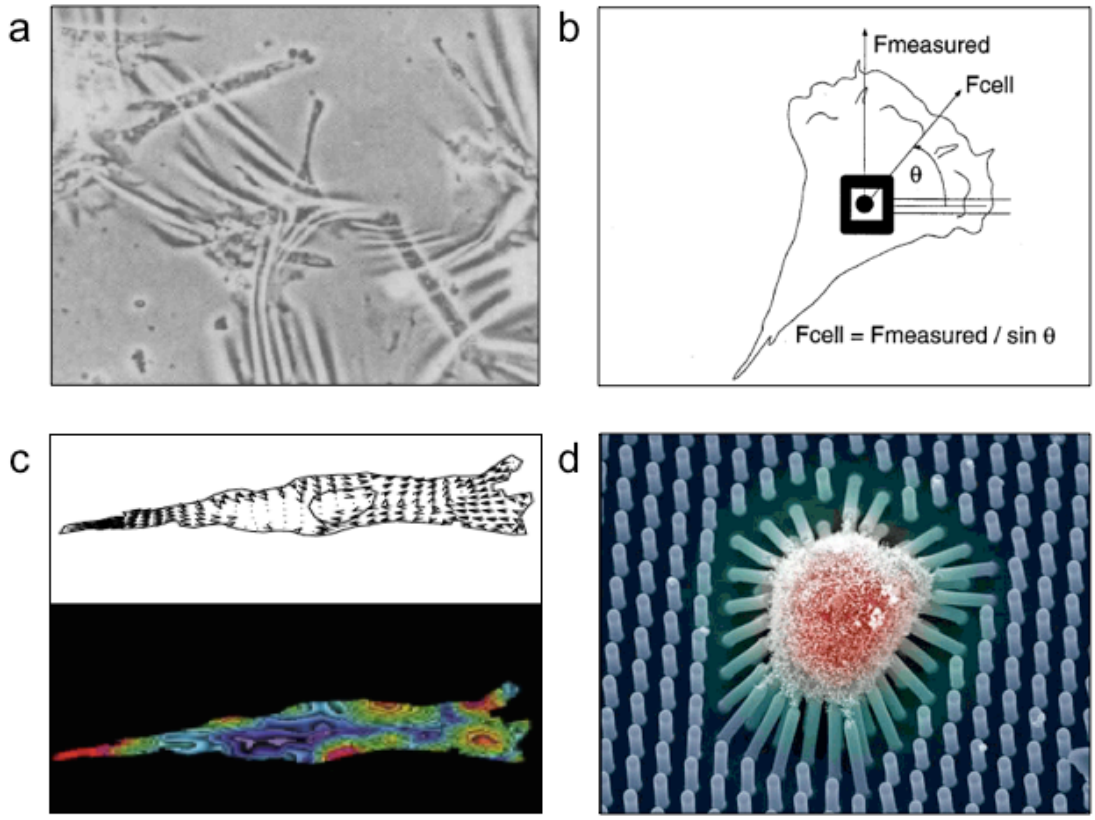

Figure 1.1. Methods to measure cellular traction forces.

(a) Cells cultured on thin silicone films induce wrinkling to give qualitative estimates of forces. Image reprinted from (Harris et al., 1980). (b) Microfabricated cantilevers are deflected by migrating cells to give a direct force measurement. Image reprinted from (Galbraith and Sheetz, 1997). (c) Fluorescent beads dispersed in transparent polyacrylamide gels serve as fiduciary markers whose displacements from the relaxed state can be inverted to obtain the traction field exerted by the cells. Image reprinted from (Beningo and Wang, 2002a). (d) Cells cultured onto elastomeric microposts horizontally deflect the posts giving a direct measure of the tangential forces. Image reprinted from (Fu et al., 2010).

1.4 Molecular Methods to Measure Forces

At this smaller molecular scale, many biological molecules including enzymes and structural proteins such as elastin, tenascin, and FN respond to cell-force through altered activity, mechanics, fibrillogenesis, adhesivity, and revealing of cryptic signaling motifs (Bustamante et al., 2004; Craig et al., 2001; Jones and Jones, 2000; Rosenbloom et al., 1993; Smith et al., 2007). Researchers have begun attempting to recreate or manipulate these natural molecules' force-responsiveness to affect these cell responses (Grieshaber et al., 2009; Martino et al., 2009; Ng et al., 2007; Zhuang et al., 2009). Other advances include membrane bound enzymes or polymer brushes that alter their activity or absorbance in response to force (Azzaroni et al., 2006; Bunsow et al., 2010; Mertz et al., 2009). Polymers that change color due to force-induced changes of either non-covalent or covalent bonds (mechanophores) are the latest generation of synthetic force reporters (Azzaroni et al., 2006; Davis et al., 2009; Kim and Reneker, 1993; Mertz et al., 2009; Nallicheri and Rubner, 1991), whose force behaviors can be explicitly calculated from the behavior of their monomers (Akbulatov et al., 2012). While novel and interesting, force induced covalent chemistry requires forces several orders of magnitude beyond cellular tractions (Ribas-Arino et al., 2009).

Recent advances have been made using polymer worm-like chain (WLC) systems to measure forces within and outside of cells. Many of these studies employ the strategy of using fluorescence resonance energy transfer (FRET) as a distance measurement between the two ends of a flexible long polymer, either synthetic or peptide, that can freely move end-to-end. Grashoff *et al.* created a genetic construct of the FA protein vinculin with the head and tail domain separated by an elastic WLC protein flagelliform from spider silk. The elastic linker was flanked by a FRET pair whereby higher FRET efficiency indicated lower tension and *vice versa*. This study lent

credence to the model that vinculin is the 'clutch' for adhesion assembly as tension across vinculin precedes adhesion stabilization. While highly elucidating regarding the tension across vinculin during adhesion formation, this system is difficult to extend to other proteins, crucial since vinculin is far from the only protein to experience force within the cell, and this study does not address the tension between the cell and its outside environment. Alternatively, another study used the polymer polyethylene glycol (PEG) as the WLC to separate a FRET pair. This provided a force map during the events of endocytosis of a cell membrane receptor upon binding its target ligand (Stabley et al., 2012).

1.5 Angiogenesis Regulation by Adhesion

As described, cellular forces are important to many biological processes, but perhaps most dramatically evident during morphogenetic process such as the bending, folding, and extension that occur during body and tissue development. One specific process that our research group studies is angiogenesis, wherein new capillary blood vessels are formed.

Every tissue is dependent on a functional, multi-scale vasculature to enable transport between cells and their environment for metabolic activity (Granger et al., 1975). To meet these needs, new vessels must grow and coordinate in a guided fashion (Goldman, 2008; Jain, 1999). Vessel growth occurs *in vivo* during both embryonic vasculogenesis, the coordinated association of vascular progenitor cells into structures prior to large vessel development (Coultas et al., 2005), and angiogenesis, including developmental and dynamic sprouting of vessels from the preexisting vasculature (Adams and Alitalo, 2007). During development, angiogenesis is a highly structured process whereby the locations, sizes, and patterns of developing vessels are under tight genetic, environmental, and intercellular control (Blum et al., 2008; Childs et al., 2002).

During post-natal angiogenesis, the oxygen requirements of cells dictate the growth and sprouting of new capillaries to form capillary beds, which allow nutrient exchange (Fong, 2008).

While angiogenesis is of vital importance to understanding development or wound healing, much of the current research has been limited to aberrant or pathological angiogenesis. Tumor development and diabetic retinopathy are two primary examples of chronic diseases in which inhibition of angiogenesis is being pursued as a means toward disease treatment (Madan and Dahut, 2009; Mauriz and Gonzalez-Gallego, 2008; Pandya et al., 2006; Tonra and Hicklin, 2007). There is also mounting evidence that angiogenic processes play a pivotal role in the onset of atherosclerosis (Moulton, 2006). Due to these clinical challenges, much of the research efforts regarding angiogenesis are concerned with blocking or abrogating this physiologic process. However, there is a growing interest in harnessing pro-angiogenic manipulations for treatment of ischemia or cardiac infarction (Ahn et al., 2008; Fortuin et al., 2003; van Weel et al., 2008). More recently, there has been a great deal of research effort towards the treatment and replacement of failed tissue or organs using pre-defined cell-seeded tissue engineering scaffolds, which control and direct tissue morphogenesis (Lutolf and Hubbell, 2005). However, since cells must be within about 200 μm of vasculature for nutrient and waste transport, developing means to vascularize these scaffolds is critical for the field to advance (Goldman, 2008). Whether in the context of treating disease or of designing viable large-scale artificial tissue scaffolds, detailed knowledge of the mechanisms of angiogenesis is urgently needed.

Cellular adhesion to the ECM also directly regulates angiogenesis. Historically, it was first observed that endothelial cells (ECs) grown on 2D surfaces coated with ECM proteins responded to low, intermediate, and high ECM surface densities independent of

growth factors through apoptosis, tubulogenesis, or proliferation respectively (Ingber and Folkman, 1989b). While this demonstrated that the degree of adhesion might play a role in influencing the various processes of angiogenesis, the potential importance of rounded cell morphology on ECM sparse substrates, was not well understood. Then, future worked showed, using microfabrication techniques to spatially define cell spreading area, that rounded cells underwent apoptosis and spread cells increased their proliferative response even if overall density of ECM was constant (Chen et al., 1997). While this work showed that geometric control altered cellular behavior, future work showed that analogous principles apply for higher-level angiogenesis structure formation. By patterning human capillary ECs in patterned stripes, Dike and colleagues showed that ECs grown on stripes of intermediate densities of adsorbed ECM protein underwent apoptosis on very narrow stripes (<10μm), proliferation on wide stripes (>2000μm), and differentiated to form tubes at intermediate widths (~1000μm) (Dike et al., 1999). This study was later extended to ECs grown on surfaces of PEG diacrylate hydrogels functionalized with the adhesive RGDS peptide sequence. This work also showed that intermediate densities of RGDS (20mM) enabled angiogenesis, but that excessively high concentrations of RGDS (>100mM) inhibited tubulogenesis (Moon et al., 2009). This thesis will describe the development of a PEG material to study and manipulate *in vitro* angiogenesis through altering adhesiveness and geometry.

1.5 Overview of Thesis

The aforementioned studies have demonstrated the importance of forces exerted by cells upon the extracellular matrix pertaining to a variety of crucial functions. The knowledge advanced by existing methods to measure cellular tractions including TFM and macropost systems have provided invaluable detail into how cells migrate and regulate their force generation. However, as the molecular complexity of adhesions

becomes appreciated, efforts to find means to investigate forces at finer spatial resolution become warranted. While WLC chain molecular systems have been employed to measure forces fluorescently, the signal resolution is inherently diminished due to the nature of the probes. In this work, our motivations to utilize DNA hairpins as cell force reporters will be detailed. DNA hairpins offer a digital signal to measure force fluorescently at the molecular level, while in aggregate, they provide analogue measures of cell forces in real-time.

In **Chapter 2** we will demonstrate our strategies to synthesize these DNA force probes. The use of solid-state DNA synthesis will be overviewed along with the specific design challenges we overcame. Further, we will characterize these force probes both chemically and physically. Using dual optical trapping, the response of these force probes to actual mechanical force at the molecular level will be demonstrated.

In **Chapter 3** the strategies to functionalize these force probes onto glass surfaces will be overviewed. Then we will show the methods of culturing live mammalian cells on surfaces functionalized with force probes to fluorescently report cellular tractions in real time. The biological validation of this strategy will be overviewed along with a way of calibrating fluorescent signal to force values. Finally, the biological discoveries made using these new force probes will be described.

In **Chapter 4** we will present a novel PEG-based hydrogel to engineer *ex vivo* angiogenesis. The base of these gels will be MMP-sensitive acrylamide PEG gels synthesized from step-growth polymerization. Pendant PEG groups with the peptide sequence CGRGDS will allow cell attachment. These bioactive PEG gels will be micromolded into specific geometries to confine angiogenic sprouting from chick aortic arch explants.

CHAPTER 2

Development of Molecular Force Probes

2.1 Introduction

Chapter one detailed several examples of molecular force sensitivity in both natural and engineered molecular systems. As an alternative to peptide and polymer WLC approaches, we sought to utilize another class of biomacromolecules whose force-responsiveness has been extensively characterized: DNA. The force probes used in our studies are artificially synthesized DNA hairpins. The first section of this chapter will begin with an overview of the molecular studies of DNA molecules' response to force, the standard strategy to synthesize oligonucleotides using solid-state synthesis, and a more detailed description of the experimental approach used in our studies to characterize the force responsiveness of our force probes.

2.1.1 Molecular Studies of DNA Force-responsiveness

Advances in measuring the molecular force-responsiveness of individual DNA molecules make this one of the most rigorously defined force responsive natural materials (Bockelmann, 2004). In 1992 the force response of a single DNA strand was studied for the first time, subjected to a constant magnetic force up to 30pN, while later methods discovered the new 60pN force-generated S-DNA, perhaps important for the function of the RecA enzyme (Cluzel et al., 1996; Smith et al., 1996; Smith et al., 1992). Coiling DNA molecules and measuring the effects of force versus extension allowed deeper understandings of the mechanisms behind topoisomerase (Smith et al., 1996;

Strick et al., 2000). Unzipping double-stranded (dsDNA) demonstrated that nucleotide (nt) sequence determined the forces needed (Essevaz-Roulet et al., 1997).

Internal, self-complementary sequences within DNA oligomers generate loop structures through hydrogen bonding. This phenomenon underpins the widely employed molecular-biology tool, fluorescent molecular beacons (MBs), to report the presence of a complementary sequence (Tyagi and Kramer, 1996). A fluorophore and quencher pair, functionalized to the ends of a DNA hairpin, is in sufficient proximity to quench fluorescence when the MB hairpin is folded. Binding a complementary DNA sequence breaks intramolecular hydrogen bonds, enabling fluorescent detection, specific enough for PCR or intracellular mRNA and single nucleotide polymorphism (SNP) detection (Santangelo, 2010).

Critically for this work, hairpins are also inducibly unfolded by force. Single-molecule manipulation has demonstrated that this is best modeled as a two-state system between folded and unfolded, where the ratio of the two states is directly related to force as given in a simple Arrhenius model (Li et al., 2006; Liphardt et al., 2001; Mossa et al., 2009; Rief et al., 1999; Woodside et al., 2006a; Woodside et al., 2006b). This is contrasted with dsDNA or ssDNA, which is best modeled as an elastic polymer with a defined stiffness (Conroy and Danilowicz, 2004). The elastic bending of DNA strands has been used to design FRET based probes of DNA bending-forces during annealing of DNA loops (Shroff et al., 2005; Shroff et al., 2008).

Intriguingly, the forces measured for DNA hairpin state transitions can be varied from approximately 5pN to 50pN, depending on stem length, GC content, and the ionic strength of solution (Anthony et al., 2012a; Woodside et al., 2006b), while the forces required to break the non-covalent bond between integrins and various ECM proteins fall within a range of 30pN to 140pN depending on the measurement approach and cell type

(Kong et al., 2009; Sun et al., 2005). Thus, hairpins allow a means to measure force, whereby the distribution of hairpins within a given state, folded versus unfolded, provides a measure of the local tension in their environment. The scheme shown in Figure 2.1, using RGD functionalized fluorescent hairpins is unique and advantageous to other FRET based force probes, as it allows measurement of cell-ECM forces in real-time in a digital and sequence-tunable manner. Here we develop a library of molecular mechanosensors that will be encoded by matching DNA hairpin intramolecular binding energies with specified fluorescent dyes.

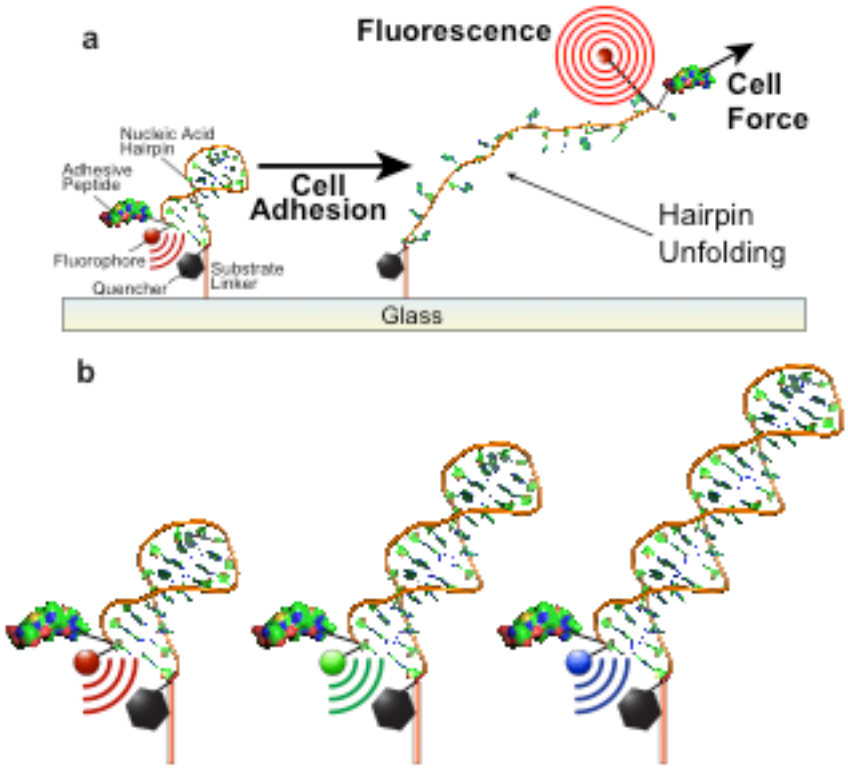

Figure 2.1. DNA Force Probes

(a) Schematic depiction of the FPs. A DNA hairpin is functionalized with a fluorophore-quencher pair, covalently conjugated by its 3' end to a solid substrate, and conjugated at its the 5' end, via a PEG spacer, to the integrin-binding peptide RGD. Upon the

application of sufficient force to unfold the hairpin, the fluorophore separates from the quencher and fluoresces. (b) We have synthesized a multicolored library of these force probes. Altering the sequence permits tuning of the force of unfolding.

2.1.2 Solid-State Synthesis of DNA

The large size of biomolecules, such as peptides and DNA, present great challenges towards strategies to synthesize them in the laboratory. For peptide synthesis, the development of solid-state synthesis bypassed the need to synthesize, purify, and characterize each reactant step in generating a large polypeptide. Just as importantly, the approach allows full automation. Similarly, solid-state strategies are used to synthesize oligonucleotides. The preeminent standard approach to synthesizing DNA and RNA fragments is the cyanoethyl phosphoramidite method (Greco and Tor, 2007). In this technique, DNA is synthesized in the 3’ to 5’ direction, the opposite of natural nucleotide synthesis. The 3’ end of the initial base is attached to the solid resin, and the phosphoamidite on the next nucleoside works as an activated phosphate to react with the 5’ OH group of the solid-bound precursor to extend the backbone of the growing chain. Unreacted 5’ OH groups are capped with acetic anhydride (AA) to prevent deletion mutations. The OH groups of the added nucleosides are protected with 4,4′-dimethoxytrityl (DMT) which is orthogonal to the protection of any amino groups on the bases. After cleavage from the resin, the bases are deprotected either in concentrated ammonia or more mild conditions described later. The overview of this process is shown in Figure 2.2.

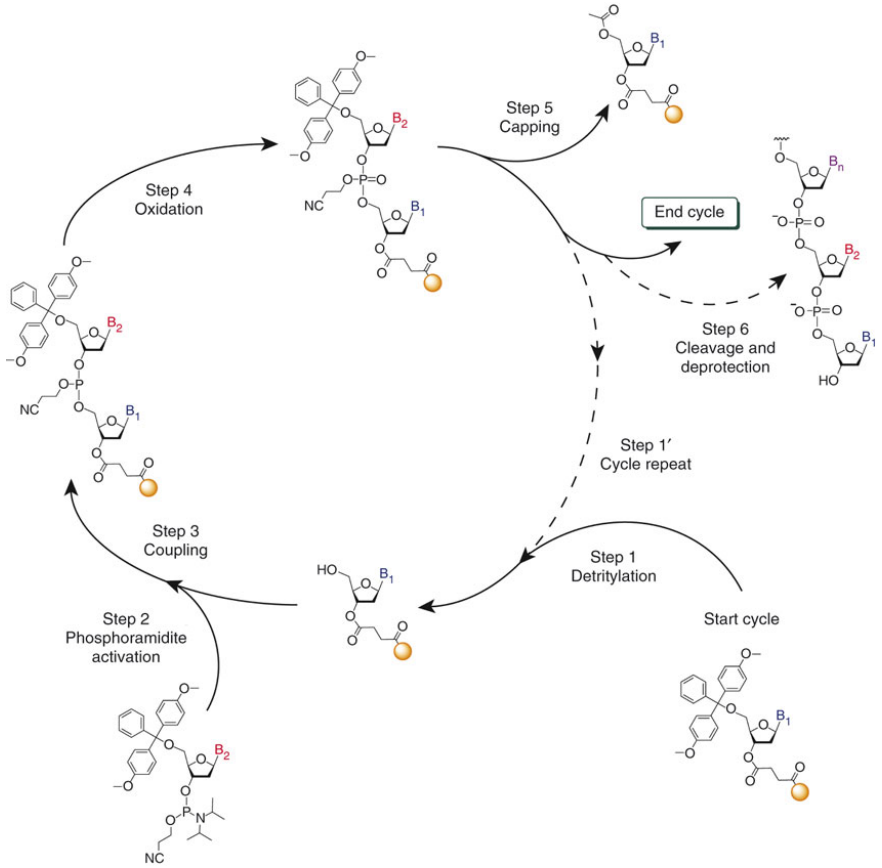

Figure 2.2. Overview of DNA Solid-State Synthesis.

Scheme of cyanoethyl phosphoramidite oligonucleotides synthesis. The initial base is on a solid resin with the OH group protected by DMT. The additional nucleotides are then added with phosphates activated with phosphoramidite. After oxidation of the phosphorus, unreacted moieties are blocked with AA. After cleavage from the resin, the bases are deprotected in concentrated ammonium hydroxide. Image reprinted from (Greco and Tor, 2007).

Further chemical modifications were needed to produce DNA-based force probes. To allow for cell attachment, the DNA was functionalized with the RGD peptide to allow for cell attachment. RGD is an integrin ligand (Ruoslahti and Pierschbacher,

1986). At the 5' end of the force probes, the fluorophore was conjugated followed by a thiol group to react with a succinimide-maleimide crosslinker to then conjugate the amine of the GGRGDS peptide to allow for cell attachment. At the 3' end of the DNA, the quencher was conjugated followed by a PEG spacer and a thiol group to allow for surface conjugation of the final force probe. The details of the synthesis scheme are shown in Figure 2.3.

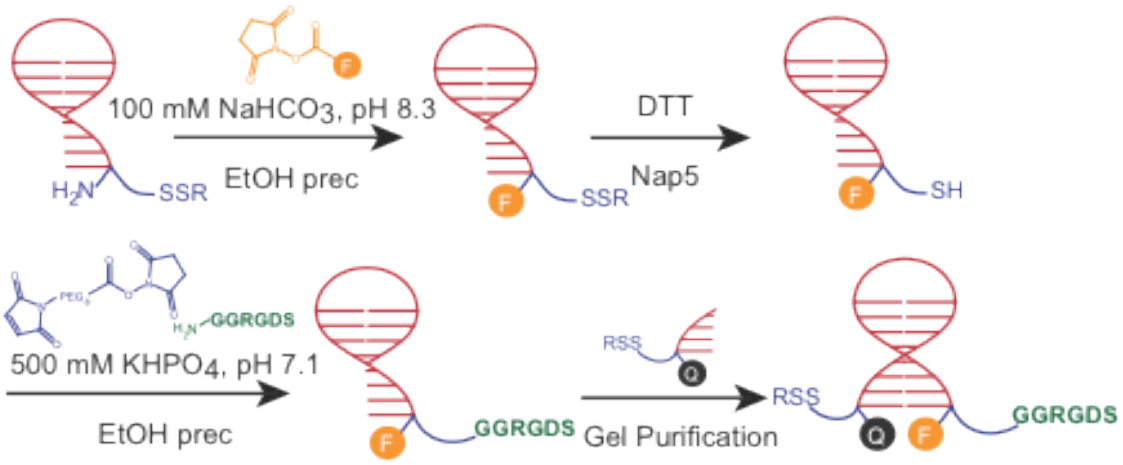

Figure 2.3. Detailed chemical scheme for synthesis of FPs.

FPs were synthesized using solid-phase synthesis in two fragments. The 3′ end contained a free thiol and the 5′ end of the other fragment was conjugated to the GGRGDS peptide. After purification, the fragments were ligated.

2.1.3 Passive Dual Optical Trap Apparatus

The physical characterization of our force probes was done using a dual optical trap apparatus. Polarizable objects, in this case dielectric styrene beads, can be trapped in highly focused laser light (Neuman and Block, 2004). Near the focus, any displacement of the bead is reacted upon by a nearly linear increase in force (positive

spring constant). However, the further away from the focus that the bead travels, the lower the spring constant becomes until a force maximum is reached. Beyond this point, the spring constant of the trap becomes negative until a distance is reached at which the trapping force is zero. Dual trapping utilizes this phenomenon by employing two traps of different strengths. In the weaker trap, the bead is moved into the zero stiffness region, in which small displacements lead to essentially constant force. The bead in the stronger trap is within the linear range, so while the force is clamped (constant force) in the weaker trap to record displacement, the force can be read in the stronger trap (Figure 2.4)

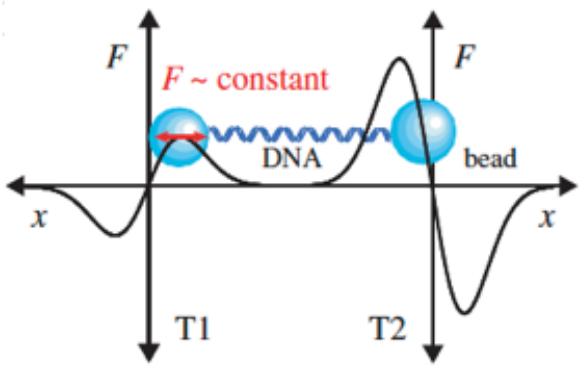

Figure 2.4. Energy Profile of Dual Optical Trap.

In the geometry of the dual optical trap, the bead in the weaker trap (T1) is moved farther from the focus of the trap to a quasi-zero-stiffness region as shown in the F-x curve. The other bead in the stronger trap (T2) is nearer to the focus, where small deviations from the center leads to an approximately linear increase in force. Image reprinted from (Greenleaf et al., 2005).

(Greenleaf et al., 2005). The higher temporal and spatial resolution of this passive clamping technique makes it possible to probe the force responsiveness of very rapidly

occurring processes such as hairpin unfolding (Woodside et al., 2008). In this arrangement, a DNA hairpin is captured via two single stranded ~1 kb DNA handles. One handle is bound to a 600 nm styrene bead via a biotin:avidin linkage and the other handle to a 730 nm styrene bead via a digoxigenin:antidigoxigenin linkage. The 600 nm bead is held in a weaker laser trap. It is this technique that has provided much understanding of DNA and RNA unfolding energetics in response to force. (Anthony et al., 2012a; Frieda and Block, 2012; Woodside et al., 2006a; Woodside et al., 2006b; Woodside et al., 2008). In the case of DNA hairpins, it's been found that the hairpins do transition from a folded to an unfolded state in a highly sharp energetic two-state manner that is highly dependent on the sequence and any structural defects such as mismatched base pairs (Woodside et al., 2006a). When constant force is applied to hairpin, there is a magnitude of force at which the hairpin spends equal time in the folded and unfolded state, which is referred to as the $F_{1/2}$.

In this work, we sought to demonstrate via optical trapping that our force probes behave as DNA hairpins molecularly in response to physical forces as has been characterized previously (Woodside et al., 2006b). Specifically, we were concerned that additional modifications to the hairpins to render them force probes, such as the fluorophore-quencher pair would impact the force needed to unfold the hairpins or the two-state nature of the transition. Specifically, we found that additional PEG spacers between various functional groups were needed for successful cellular experiments (see chapter 3), and the fluorophore-quencher pair has been shown to affect hairpin unfolding thermodynamics (Tyagi and Kramer, 1996). Finally, while most molecular force characterization studies have been performed in standard buffers, the need to culture cells in a unique medium was also a possible source of corruption of the hairpin unfolding energetics (Anthony et al., 2012b).

At the inception of this work, to select which sequences to utilize for our force probes, we chose to utilize sequences that had been previously characterized for the response to unfolding from force (Woodside et al., 2006b). However, we chose a new nomenclature reflective of the force-responsiveness of the hairpins. For example, the sequence 20R25/T4 in Woodside et al. (Woodside et al., 2006b) had a measured $F_{1/2}$ of approximately 10.6 pN. We renamed this molecule for the $F_{1/2}$ value to become 'Force Probe 11' or FP11. To see how our nomenclature differs from Woodside et al. (Woodside et al., 2006b) see Table 2.3. We synthesized one force probe with a previously uncharacterized sequence with a measured $F_{1/2}$ value of approximately 8 pN, so this molecule was referred to as FP8.

2.2 Objectives

The goal of this stage of our work was to synthesize and characterize our DNA force probes. These molecules were then to be used to measure the traction forces of living cells in real-time fluorescently. Optimizing the synthesis strategy was recursive with surface conjugation discussed in chapter 3. Success or failure during those studies was used to inform the molecular design of the force probes. Upon synthesis, the next steps were characterization, both chemical and physical. To summarize, the point-by-point objectives were as follows:

1. Synthesize the DNA force probes by solid-state synthesis.
2. Chemically characterize the DNA synthesis for purity and functionality.
3. Physically characterize the force probes by performing dual optical trapping.

2.3 Materials and Methods

2.3.1 Synthesis of Force Probes

Synthesis of GGRGDS. The GGRGDS peptide was synthesized on a Tribute instrument (Protein Technologies) on a 300 µmol scale using standard Fmoc peptide

synthesis protocols, Fmoc-L-Ser(tBu)-Wang resin (Chem-Impex) and 1.5 mmol amino acid/HBTU cartridges (Protein Technologies). After cleavage from the solid support and removal of protective groups from the side chains using trifluoroacetic acid/phenol/water/triisopropylsilane (88/5/5/2), the peptide was precipitated with ether and purified by high-pressure liquid chromatography (HPLC, Agilent Technologies 1100 series) on a Kromasil 100-5-C18 column (21.2 x 250 mm) by running a 0.1% trifluoroacetic acid solution for 5 min and subsequently increasing the organic phase to 20% acetonitrile over 30 min.

Synthesis of force probes for cellular experiments. For each force probe, two DNA fragments (A and B) were synthesized on 1 mmol scale on a PerSeptive Biosystems Expedite 8909 DNA synthesizer, using commercially available standard base monomers and sequence modifiers. The larger fragment A contained a 5′ protected thiol modifier (Thiol-Modifier C6 S-S, Glen Research), followed by an amino modifier (Fmoc Amino-Modifier C6 dT, Glen Research) and either nucleotides 1-34 of the hairpin sequence for FP11 and FP19, or nucleotides 1-19 for FP8. Alternatively, fluorescently labeled fragments were synthesized using a fluorophore containing phosphoramidite (6-Fluorescein Serinol Phosphoramidite, Cy3™ Phosphoramidite, TAMRA-dT, Glen Research). The smaller fragment B contained the remaining nucleotides of the force probe at the 5′ end, followed by a quencher (Epoch Eclipse™Quencher Phosphoramidite, Glen Research; BBQ-650®-dT CEP, Berry & Associates; BHQ-1-dT), a PEG spacer (Spacer Phosphoramidite 18, Glen Research) and a 3′ protected thiol modifier (3′ Thiol Modifier C6 SS CPG, Biosearch Technologies). Fragments under 20 nucleotides in length were synthesized with cleavage of the final trityl group on resin. Following solid phase synthesis, final cleavage from the solid support and the removal of protecting groups were carried out by treatment with aqueous ammonium hydroxide and

methylamine (1:1) at 65°C for 20 min. For TAMRA-containing DNA sequences, an UltraMILD deprotection scheme was deployed, following the manufacturer's instructions. The oligonucleotides were purified by reverse-phase HPLC (Agilent Technologies 1200 series), using a linear gradient from 100 mM triethyl ammonium acetate to 100% acetonitrile at 45 °C on an Eclipse XBD C18 column (5 mm, 9.4 x 250 mm, Agilent), and lyophilized. If appropriate, the trityl group was removed by the addition of 3% trifluoroacetic acid, followed by precipitation with 10% v/v 3 M NaOAc, pH 5 and 300 % v/v ethanol.

Where appropriate, fragments A were labeled with fluorophore by incubating 100 nmol oligonucleotide and 1 mmol fluorophore (5-carboxyfluorescein N-succinimidyl ester, Sigma; Alexa Fluor 546 succinimidyl ester; Life Technologies; Alexa Fluor 647 succinimidyl ester; Life Technologies) for 18 hr at 25 °C in 200 mM aq. $NaHCO_3$, pH 8.3. Excess fluorophore was removed by ethanol precipitation of the oligonucleotide-fluorophore conjugate. The peptide was appended to the 5' thiol modification as follows: 100 mM dithiothreitol (DTT) was added to the oligonucleotide in 50 mM Na_2HPO_4, pH 8 at 25 ºC for 30 min to cleave the 5′ S-S bond. The reaction was purified by size exclusion chromatography using a NAP-5 column (GE Healthcare Life Sciences) and ethanol precipitation. 100 nmol of the thiol-containing oligonucleotide was stirred with 2 mmol $SM(PEG)_8$ (Thermo Scientific), 10 mmol GGRGDS, and 5 mmol tris(2-carboxyethyl)phosphine (TCEP) in 500 mM KH_2PO_4, pH 7.1, for 18 hr at 25°C. The reaction was purified by ethanol precipitation, followed by a NAP-5 column. Purity was analyzed by liquid chromatography-mass spectrometry (LC/MS). If the relative coupling yield was below approximately 50%, the peptide conjugation reaction was repeated. Fragments B were 5′ phosphorylated by incubating 200 nmol oligonucleotide with 100 U T4 PNK (NEB) in 1x T4 DNA ligase buffer (NEB) for 8 hr at 37°C, followed by

inactivation of the enzyme for 20 min at 65°C. The completeness of the phosphorylation reaction was analyzed by LC/MS.

Labeled fragments A and B were ligated by mixing 50 nmol and 70 nmol, respectively, in 1x T4 DNA ligase buffer. For the unstructured (US) control sequence, another 100 nmol DNA splint was added to anneal and ligate the two fragments together. The mixture was heated to 94°C for 5 min followed by incubation at 25°C for 15 min. After melting and annealing the fragments, 8000 U T4 DNA ligase (NEB) was added and then incubated for 16 h at 25°C. Subsequently, the reaction mixture was ethanol precipitated, dissolved in 80% formamide, and purified by denaturing gel electrophoresis on a 10% TBE/urea gel (Criterion, Bio-Rad) at 65°C. The desired bands were cut from the gel and the DNA was extracted twice by addition of 300 mM NaCl, followed by filtration to remove gel debris and ethanol precipitation. The purity of the product was analyzed by LC/MS. If necessary, gel purification was repeated. Cleavage of the 3′ S-S bond was performed with 100 mM DTT in 50 mM Na_2HPO_4, pH 8 at 25 ºC for 30 min, followed by gel filtration using a NAP-5 column (GE Healthcare Life Sciences). A different synthesis scheme was deployed for the fluorescein-labeled unfolded control construct, US-Fluorescein. It was synthesized on solid support as a single piece with an amino modifier at the 5’ end (5'-Amino-Modifier 5, Glen Research), followed by fluorescein (6-Fluorescein Phosphoramidite, Glen Research), the oligonucleotide sequence, the epoch eclipse quencher, and the 3′-protected thiol modifier (3′ Thiol Modifier C6 SS CPG). After cleavage and work-up as described above, the peptide was appended by incubation of 50 nmol oligonucleotide with 800 nmol bis-NHS crosslinker (BS(PEG)9, Thermo Scientific) in 100 mM KH2PO4, pH 7.1 at 25°C for 30 min, followed by addition of 8 µmol GGRGDS and incubation at 25°C for 18 hr. Work-

up and thiol deprotection procedures were performed as described above. The purified force probes were analyzed by LC/MS, quantified by UV spectroscopy, and lyophilized.

2.3.2 Chemical Characterization of Force Probes

Liquid chromatography - mass spectrometry of force probes. Oligonucleotides were analyzed by LC/MS using a Waters Aquity UPLC coupled to a Waters Q-TOF Premier instrument. 10 pmol sample was run using a linear gradient from 6 mM triethylammonium bicarbonate to 100% methanol over 5 min on an Aquity UPLC BEH C18 column (1.7 µm, 2.1 mm x 100 mm, Waters) at a constant flow rate of 150 µL/min. Electrospray ionization was used with a capillary voltage of 3 kV, a sampling cone voltage of 40 V; the detector was operated in negative-ion mode.

Melting curves of force probes. Force probes were assayed at a 100–500 nM concentration in PBS or 0.2x PBS, 6 M urea on a CFX-96 Real-Time System with a C1000 Thermal Cycler (Bio-Rad). After an initial refolding step for 2 min at 94°C followed by 5 min at 25°C, the probes were gradually heated to 94°C while the fluorescence was observed using the predefined settings for FAM (fluorescein labeled force probes), HEX (Alexa 546, Cy3, and TAMRA labeled force probes), Cy5 (Alexa 647 labeled force probes). The exact buffer conditions for the various force probes was as follows:

- FP11-Fluorescein: 73 ^{o}C in PBS (53 ^{o}C in 100 mM Na2HPO4, 7 M urea, pH 7.1)
- FP11-Alexa546: 73 ^{o}C in PBS
- FP11-Alexa647: 72 ^{o}C in PBS
- FP8-Fluorescein: 66 ^{o}C in PBS
- FP8-Alexa647: 64 ^{o}C in PBS (42 ^{o}C in 1/5 PBS, 6.4 M urea)
- FP19-Fluorescein: >100 ^{o}C in PBS (85 ^{o}C in 100 mM Na2HPO4, 7 M urea, pH 7.1)
- FP19-Alexa647: >100 ^{o}C in PBS (87 ^{o}C in 1/5 PBS, 6.4 M urea)

- US-Fluorescein: -
- US-Alexa546: -
- US-Alexa647: -

2.3.3 Physical Characterization of Force Probes

Synthesis of force probes for optical tweezers experiments. The synthesis of FPs used for the determinations of opening force was carried out analogously to the method described above. Fragment A contained a 5′ adaptor sequence for annealing with complementary sequences, as described previously(Anthony et al., 2012a), followed by a PEG spacer (Spacer Phosphoramidite 18), fluorescein (6-Fluorescein Phosphoramidite, Glen Research) and either nucleotides 1-34 of the hairpin sequence for FP11, or nucleotides 1-19 for FP8. Fragment B contained the remaining nucleotides of the force probe at the 5′ end followed by the quencher (Epoch Eclipse™Quencher Phosphoramidite), a PEG spacer (Spacer Phosphoramidite 18) and a 3′ adaptor sequence. HPLC purification, phosphorylation and ligation were performed as described above.

Characterization of force probes with optical tweezers experiments. Unfolding forces, distances, and $F_{1/2}$ values were measured as described previously (Anthony et al., 2012a; Woodside et al., 2006b) using dual-beam single-molecule optical tweezers. Briefly, a 5’ overhang (2,018 bp) handle functionalized with digoxigenin was prepared by PCR with M13mp18 plasmid acting as a template. The 3’ overhang (1,044 bp) handle was similarly prepared with biotin functionalized at the end without an overhang using the plasmid pALB3 as the template. After annealing with the hairpins, the handle-hairpin constructs were incubated with 600 nm-diameter styrene beads coated with avidin and 730 nm-diameter styrene beads coated with anti-digoxigenin. The dumbbell mixture was then put into a glass chamber and mounted onto the optical trap microscope. The trap

consisted of two infrared trapping beams guided by acousto-optic deflectors. The light scattered by the beads was detected by position diodes to provide information to two detecting beams. Constant force was applied to allow the hairpin to transition from folded to unfolded. This data was then filtered and used to reconstruct the unfolding energetics. An iterated deconvolution was performed to remove thermal defects (Woodside et al., 2006b).

2.4 Results

2.4.1 Synthesis of Force Probes

The successful synthesis of the hairpin force probes was confirmed by mass spectrometry. In total, ten FPs, with opening forces ranging from 8.1-19.3 pN, were synthesized from different combinations of hairpins and fluorophores (

Table 2.1).

Table 2.1. Synthesized force probes that were used in cellular experiments, and their calculated and observed molecular weights (MW).

Force probe and conjugated dye	**MW** (calc.)	**MW** (obs.)
FP11-Fluorescein	16,458	16,462
FP11-Alexa 546	17,304	17,305
FP11-Alexa 647	17,202	17,203
FP8-Fluorescein	10,164	10,165
FP8-Alexa 647	11,024	11,027
FP19-Fluorescein	16,482	16,487
FP19-Alexa 647	17,215	17,220
US-Fluorescein	17,797	17,805
US-Alexa 546	19,107	19,111
US-Alexa 647	19,005	19,011

Thermal melting the FPs demonstrated unfolding-induced fluorescence. Several candidate fluorophore-quencher pairs were investigated, based on their spectral overlap and quenching properties, but only combinations containing fluorescein, Alexa 546, or Alexa 647 as the fluorophore and Epoch Eclipse™ Quencher as the quencher produced robust, cell-dependent fluorescent signals. Table 2.2 overviews the unsuccessful and successful fluorophore-quencher pairs in terms of cellular signal. While many of these pairs did not give rise to cellular adhesion signal, they did fluoresce in solution during the melting curve acquisition. Figure 2.5 shows as an example the mass spec and melt curves of FP11- Alexa 546-Eclipse, FP11- Alexa 546-BBQ, FP11- Alexa 647-Eclipse, and FP11- Alexa 647-BBQ. This shows that the failure of the BBQ probes to generate cellular signal is not due to a failure of the synthesis but rather some complication during the surface conjugation.

Table 2.2. Fluorophore-quencher pairs assayed in cellular experiments.

Fluorophore	**Quencher**	**Signal in cellular experiment**
Fluorescein	Epoch eclipse	+
Fluorescein	BBQ-650	−
Cy3	BHQ-1	−
TAMRA	BHQ-1	−
Alexa546	Epoch eclipse	+
Alexa546	BBQ-650	−
Alexa647	Epoch eclipse	+
Alexa647	BBQ-650	−

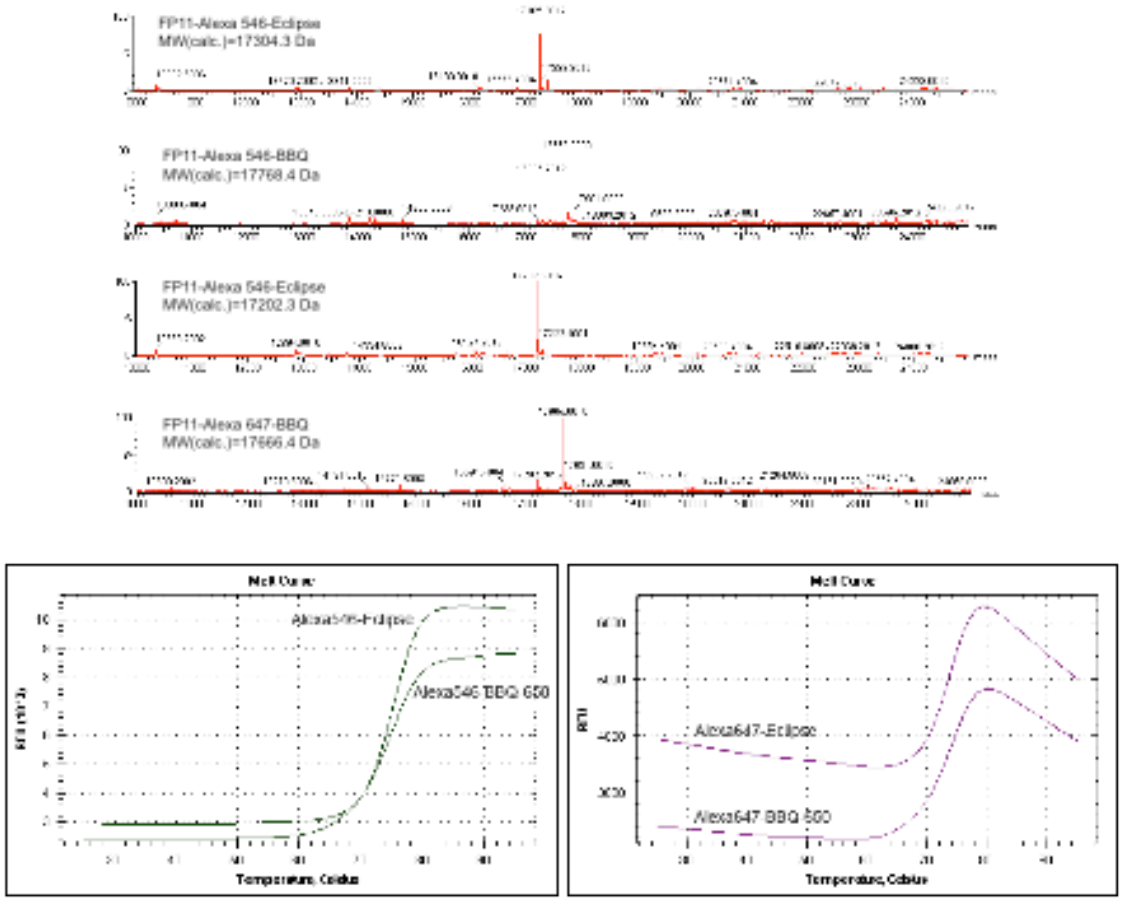

Figure 2.5. Mass Spec and Melt Curves for FP11 Alexa Probes with Different Quenchers.

The mass spectrum of FP11-Alexa 546-Eclipse, FP11- Alexa 546-BBQ, FP11- Alexa 647-Eclipse, and FP11- Alexa 647-BBQ in the top three panels demonstrate successful synthesis despite only pairs with the Eclipse quencher giving cellular traction signal. The melt curves for the FP11 constructs with Alexa-546-Eclipse and Alexa-657-Eclipse (bottom left panel) and the melt curves for the FP11 constructs with Alexa-546-BBQ and Alexa-657-BBW also confirm the unfolding-dependent fluorescence.

Oligonucleotides lacking self-complementarity were used as unfolded controls; by design, these did not produce cell-dependent fluorescence. These sequences had no structure and were thus referred to as unstructured (US). The force probes that gave the most robust signal were the fluorescein constructs. The mass spec and melting curves for the FP8-fluorescein and FP19-fluorescein constructs is shown in Figure 2.6.

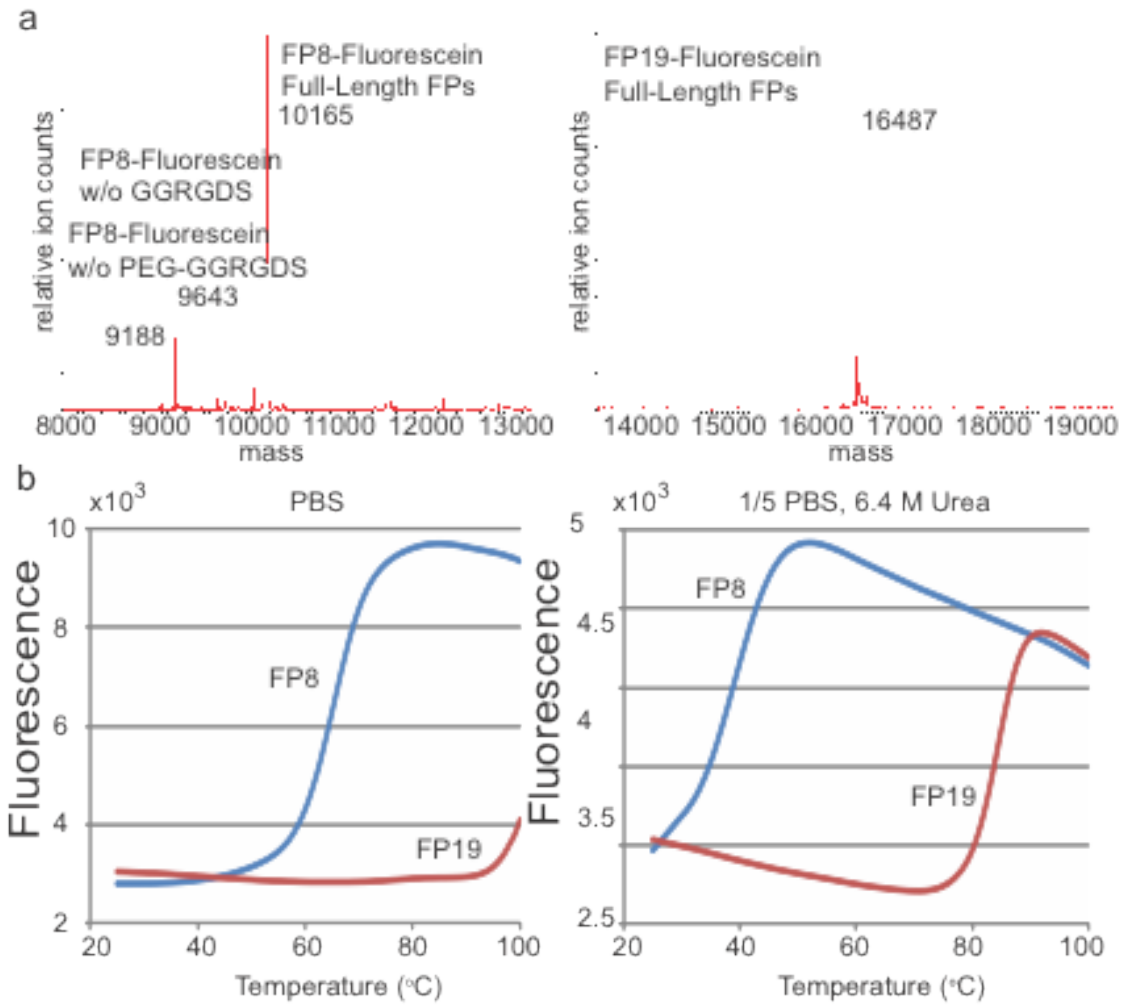

Figure 2.6. Mass spec and Melting Curves for Fluorescein Constructs.

(a) Mass-spec for fluorescein constructs of FP8 (left panel) and FP19 (right panel). (b) Melting-curves for both FP8 and FP19 in PBS (left panel) and 1/5 PBS, 6.4 M urea (right panel).

Figure 2.7 confirms the successful synthesis of both US and FP8 and FP19 with the far-red Alexa dyes.

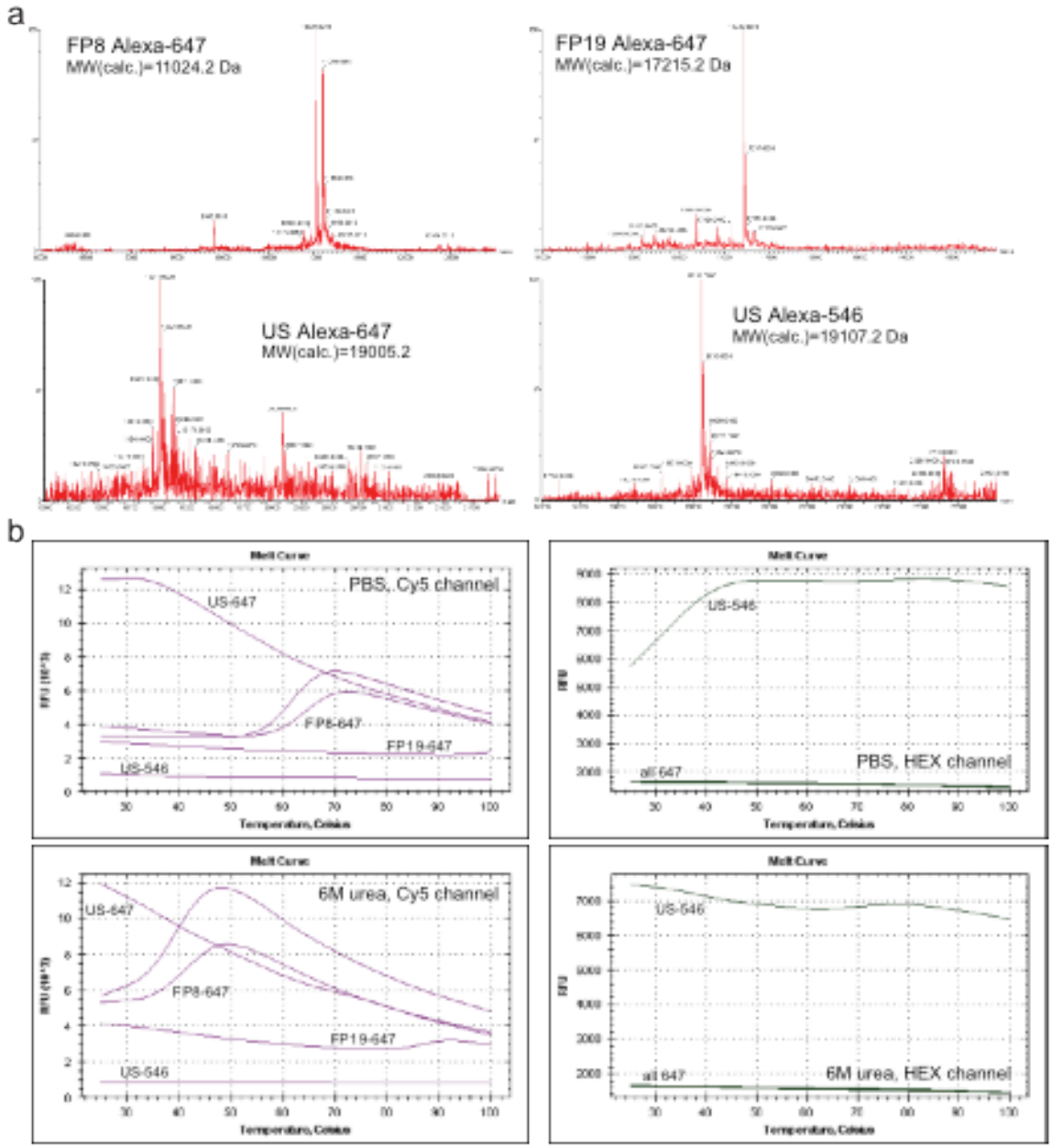

Figure 2.7. Confirmation of synthesis of FP8, FP19, and US with Alexa Red Dyes. (a) LC/MS analysis of FP8 Alexa-647 (top left panel), FP19 Alexa-647 (top right panel), US Alexa-647 (bottom left panel), and US Alexa-546 (bottom right panel) demonstrates measured MW in agreement with calculated MW

Table 2.1). (b) Plot of fluorescence of FPs versus temperature in PBS (top row) and 1/5 PBS with 6 M urea (bottom row) in both the Cy5 fluorescent channel (left column) and in the HEX fluorescent channel (right column).

2.4.2 Physical Characterization of Force Probes

Optical Trap Characterization of Force Probes. We sought to determine whether our chemical modifications of the hairpins affected the force-unfolding energetics. Using dual optical trap apparatus, we measured the force energetics of FP11 and compared our modified force probe to the unmodified hairpin measured previously (this hairpin is labled 20R25/T4 in Woodside et al. (Woodside et al., 2006b)). If the value of $F_{1/2}$ was unchanged, we reasoned that the other sequences we chose to use for a force probe (FP19) would also be reasonably expected to behave as previously characterized. In addition, we also measured the $F_{1/2}$ value of our new sequence FP8. These sequences are summarized in Table 2.3. The experimental geometry is schematically shown in Figure 2.8a.

Table 2.3. DNA sequences of the force probes used in cellular experiments, and their corresponding $F_{1/2}$ values. Duplex regions of sequences are shown in italics.

Force probe name	Sequence	$F_{1/2}$ (pN)
FP11	*AAGTTAACATCTAGATTCTA*TTTT*TAGAAT CTAGATGTTAACTT* (20R25/T4)[b]	11.3[a]
FP8	*CTAGATTCTA*TTTT*TAGAATCTAG*	8.1[a]
FP19	*CGCCGCGGGCCGGCGCGCGG*TTTT*CCG CGCGCCGGCCCGCGGCG* (20R100/T4)[b]	19.3[b]
US	CGGAAGGAATGTAGAATGAGTGAGTGGA TCGTGATGACTGTACAACTAT	not applicable

[a]measured here

[b]data from (Woodside et al., 2006b)

For FP11 and FP8, the $F_{1/2}$ values measured in culture medium were 11.3 ± 0.6 and 8.1 ± 0.7 pN, respectively, and the opening distances were 17.6 ± 0.4 and 8.0 ± 0.2 nm. Because fluorophore conjugation and buffer substitution were not found to significantly affect the folding energetics of FP11 (Figure 2.8b, Table 2.3), the $F_{1/2}$ value for FP19 was taken to be identical to a previously measured value for an unmodified hairpin with the identical sequence (19.3 pN) (Woodside et al., 2006b). Unless otherwise noted, the uncertainties reported here for measured parameters were computed from the statistical standard errors of the means added in quadrature to estimates of the systematic errors in the measurements (Anthony et al., 2012a).

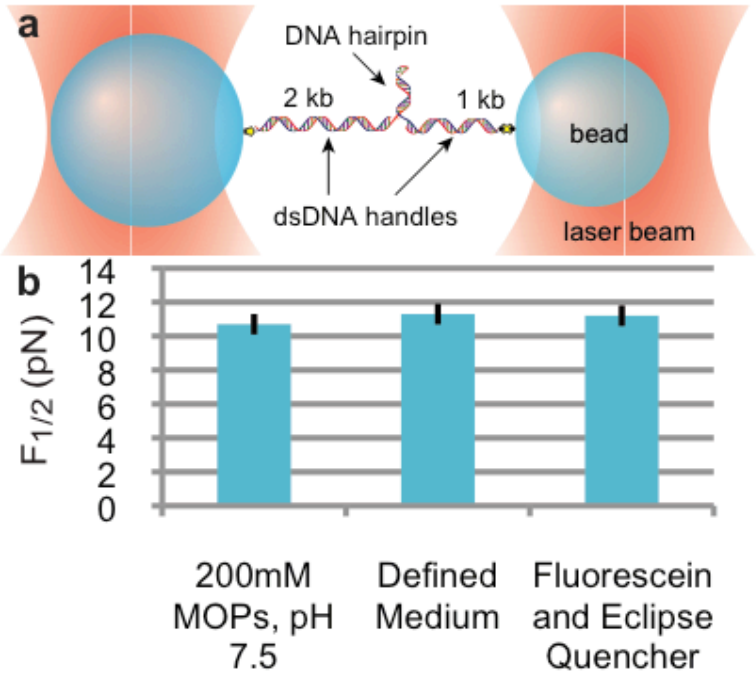

Figure 2.8. Force Characterization of Force Probes.

(a) Schematic of the experimental geometry used to characterize the mechanics of the hairpins. The DNA hairpin is attached at each of it ends to dsDNA handles bound to optically trapped beads (not to scale) in a force-clamped arrangement. (b) Measured $F_{1/2}$

(hairpin opening force) values as a function of media and fluorophore-quencher conjugation (mean ± s.e.m.).

2.5 Discussion

Synthesis of the Force Probes. The synthesis of the force probes was done in two fragments. Fragment A was the larger fragment that consisted of the 5’ end of the force probe followed by either a phosphoramidite fluorophore (fluorescein) or a modified amino base. This was done because the Alexa red dyes (Alexa 546 and Alexa 647) were both susceptible to damage from the deprotection of the bases after cleavage from the resin. So, the amino modified base was used to conjugate the Alexa dyes after cleavage and deprotection, while the fluorescein force probes were synthesized completely on the resin. Red dyes that were not synthesized in this manner, after cleavage, gave rise to non-functional force probes. Fragment B contained the 3’ end of the final force probes at the 5’ end preceded at the 3’ end by the quencher, a PEG spacer with 6 EG units, and a protected thiol for surface conjugation.

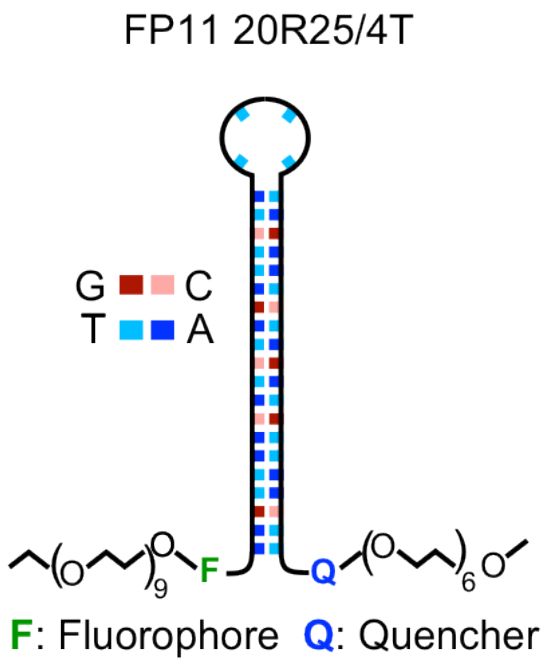

Figure 2.9. Higher Level Schematic Detail.

More detailed schematic of FP11 to illustrates the specifics of the PEG spacers on the 5' and 3' of the hairpin flanking the fluorophore and quencher.

Initial studies of cell plated on surfaces conjugated with force probes without PEG spacers gave high background and no signal. In this study, signal refers to the fluorescent reporting of cellular tractions in structures reminiscent of FAs We presumed that this was caused by some adsorption of the force probes onto the surface and a loss of structure. As a solution, we integrated PEG spacers on either side of the DNA in the force probes. This led to usable force probes (this data is shown in the next chapter). A more detailed chemical schematic of the hairpin with PEG spacers is given in Figure 2.9.

CHAPTER 3

Measurement of Cellular Tractions on 2D Surfaces with DNA Force Probes

3.1 Introduction

Upon synthesis of our DNA force probes, we aimed to affix the force probes at one end to a solid substrate and permit the other end to freely associate with cell integrin receptors. The most straightforward means to do this was to conjugate the hairpins to glass surfaces via silane chemistry. Once a workable means of conjugating to the surface was found, the next step was to culture living mammalian cells onto surfaces presenting these force probes to measure cellular tractions. This introduction will give an overview of methods to conjugate surfaces with DNA followed by a brief overview of the FA proteins we chose to further study during live-cell force measurements.

3.1.1 Surface Conjugation of DNA

DNA microchips allow highly parallel monitoring of gene expression and relies on facile conjugation of up to thousands of DNA strands to solid surfaces in a manner that does not impede complementary sequences from binding (Sanchez Carbayo et al., 2000). Interest in this field provided the bulk of historic motivation to find means to attach DNA oligomers to solid surfaces. Methods to bind DNA to solid surfaces include adsorption, avidin-avidin interactions, and covalent bonds. We initially relied on covalent methods to bind DNA to achieve the highest possible strength of bond between our force probes and solid substrates. Silanes are reactive to glass and PDMS hydroxyl groups and can bear other functional groups to allow further surface modifications. Silanes may

react with hydroxyls through one to three reactive groups. Multifunctional silanes are more stable to hydrolysis but also form multi-layered structures (Yee et al., 1991). However, others have suggested that vapor deposition of these silanes can lead to monolayer formation (Ali et al., 2008; Hong et al., 1994; Ling et al., 2003). Our force probes were designed with thiol groups to react in order to be coupled to a solid substrate. Several groups have explored various ways to conjugate thiol-labeled DNA oligomers to surfaces. One approach is to form a disulfide bond between the DNA and a thiol-bearing silane (Rogers et al., 1999). This has the added benefit of obviating the need for deprotection of the thiol groups (Kumar et al., 2000; Lenigk et al., 2001). However, this bond is labile near physiologic buffers, and others have used hetero-bifunctional crosslinkers with both maleimide and succinimide to react with an amino-bearing silane (Bhatia et al., 1992; Zimmermann et al., 2010a).

3.1.2 Canonical FA Proteins

As described, FAs are complex, multi-protein complexes involving up to 156 proteins engaging in 690 interactions (Zaidel-Bar et al., 2007). Paxillin and vinculin are among the most well studied FA proteins. Paxillin is one of the first FA proteins recruited during FA formation and its phosphorylation serves to enhance paxillin's scaffolding function for other FA proteins (Bellis et al., 1995; Laukaitis et al., 2001; Richardson et al., 1997; Schaller and Parsons, 1995). As FAs form from initial adhesive clusters and grow into focal complexes, the recruitment of vinculin marks the point at which force is generated (Galbraith et al., 2002), which, along with other studies, has helped support the model of vinculin as a tension-sensitive clutch required to permit adhesion maturation (Grashoff et al., 2010; Hu et al., 2007a). To assess whether FP fluorescent signal does correspond to unfolding of hairpins stressed by FA-mediated cell tension, cells transfected with fluorescently tagged paxillin and vinculin were plated on FP

conjugated surfaces. It was expected that there would be overlap between fluorescence reported by our FPs and these FA proteins. Additionally, this provided an opportunity to investigate how force, as measured by the FPs, interplays with the recruitment of these focal adhesion proteins at a molecular level.

3.2 Objectives

At this stage of our study, we aimed to use our synthesized DNA force probes to measure forces of living cells in real time using fluorescent spectroscopy. To achieve this aim, we needed to find the best chemical coupling scheme to attach our DNA force probes to glass as a model substrate. Then we wished to utilize the higher spatial resolution that our method provided to make key insights into cellular adhesion biology as they relate to the forces generated at the cell ECM interface. Finally, we sought to demonstrate that we could extend this method beyond traditional flat two-dimensional substrates. To summarize, the point-by-point objectives were as follows:

1. Chemically couple our force probes to glass.
2. Measure cellular traction forces with the DNA force probes.
3. Using the higher resolution of our method, make insights into adhesion biology as it relates to force.
4. Extend the use of these force probes to a more geometrically challenging setting to measure extra-cellular traction forces.

3.3 Materials and Methods

3.3.1 Functionalization of Glass-Coverslips with Force Probes

FPs were covalently attached to glass surfaces through an aminosilane reagent coupled to a succinimide-PEG-maleimide crosslinker that was reacted with the 3′ end of the hairpins (Figure 3.1) (Zimmermann et al., 2010b). Initial studies with multifunctional

silanes led to high background signals, prompting us to use a monofunctional ethoxy-silane to conjugate only one layer of hairpins to the surface and avoid intramolecular effects or adsorption. Circular coverslips (25 mm dia., #1 thickness) were sonicated in methanol for 5 min and dried in an oven. They were then plasma-cleaned for 5 min (Plasma Prep II, SPI Supplies). 3-(Ethoxydimethylsilyl) propylamine (Sigma) was incubated with the coverslips for functionalization at 3% v/v concentration in 200-proof ethanol along with 10% acetic acid aqueous solution as a catalyst at 3% v/v concentration (Sigma) for 3 hr. The coverslips were then rinsed thoroughly with 200 proof ethanol, dried with nitrogen gas and baked at 110ºC for 1 hr. Functionalized coverslips were stored under argon. Upon further functionalization, the coverslips were submerged in borate buffer (BB, 50 mM sodium borate pH 8.5) for 1 hr to protonate the amino group on the silane. A hetero-bifunctional poly(ethylene glycol) (PEG), which has an amine reactive N-hydroxysuccinimide ester (NHS) on one end, and a thiol reactive maleimide group on the other, was dissolved in anhydrous dimethyl sulfoxide (DMSO) under argon at 250 mM concentration and stored at -20ºC, as per manufacturer's instruction (Thermo Scienitfic) (this crosslinker is henceforth referred to as $SM(PEG)_2$). $SM(PEG)_2$ is very sensitive to hydrolysis, so it was aliquotted and frozen for one-time use. The $SM(PEG)_2$ stock was diluted 10-fold in BB immediately prior to use, and the silane-functionalized coverslips were dried with nitrogen gas and incubated in $SM(PEG)_2$ reaction-buffer for 90 min, then rinsed 4X in sterile DI water. FPs were dissolved in a 100 μM stock concentration in 10 mM Tris-HCl pH 7.85 buffer (TB) (Quality Biologicals) with 1 mM $MgCl_2$ and (Sigma) 1 mM ethylenediaminetetraacetate (EDTA) disodium dihydrate (Gibco) and stored at -20ºC. Prior to conjugation, the FPs were thawed and diluted to 1 μM in the same buffer and heated at 90ºC for 5 min, then cooled to room temperature for 10 min to ensure proper folding. TCEP was added to the DNA at a concentration of 10

mM and incubated for 30 min to reduce the thiol at the 3′ end. The hairpin solution was then transferred to Amicon Filter 0.5 mL Units (Millipore) with a 3 kDa cutoff and spun in a centrifuge at 16,000 g for 30 min to remove TCEP and most of the TB. The tubes were then filled with a coupling buffer (CB), a pH 7.2, 0.1 M sodium phosphate buffer (144.1 mM $Na_2HPO_4 \cdot 7H_2O$ and 7.25 mM $NaH_2PO_4 \cdot H_2O$). The tubes were then centrifuged again at 16,000 g for 30 min to replace the TB with CB. The final volume of the tube was adjusted to match the desired FP concentration during the coupling. The surface concentration was optimized for cell attachment, as both higher and lower surface concentrations resulted in diminished attachment: we found 3 μM FP concentration during coupling incubation to be optimal. Coverslips conjugated with $SM(PEG)_2$ were inserted into Attofluor cell chambers (Invitrogen) for cell seeding and imaging. FPs in CB solution were then added to the coverslips to incubate for 2 hr. After the coupling reaction, the coverslips were rinsed with 0.05% Tween 20 to rid the surface of non-covalently attached DNA, then rinsed 4X with phosphate buffered saline (PBS). Substrates could be stored overnight at 4ºC in TB.

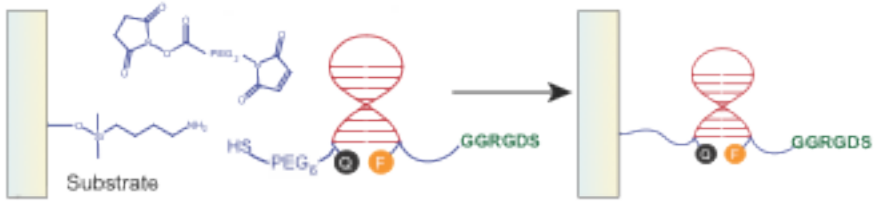

Figure 3.1. Detailed chemical scheme for surface conjugation.

The substrate was functionalized with an amine-presenting silane that was coupled to a succinimide-PEG-maleimide crosslinker that was then reacted with the 3′ end of the hairpins. The presence of conjugated hairpin was confirmed by the fluorescence of surfaces coated with US positive control hairpins.

3.3.2 Imaging and Image Processing

FP and cell images were acquired by total internal reflection fluorescent (TIRF) microscopy, using a Nikon Eclipse Ti base (Nikon Instruments, Inc.), an Evolve EMCCD camera (Photometrics) and with either a CFI Apo TIRF 60x oil (1.49NA) objective or a CFI Plan Fluor 40x oil (1.30NA) objective (Nikon). Live-cell imaging was performed at 37°C and 5% CO2. FP-functionalized coverslips were inserted into Attofluor cell chambers (Invitrogen). Spontaneously immortalized mouse embryonic fibroblasts (MEFs) (Richard Assoian, University of Pennsylvania) or NIH 3T3 cells were trypsinized prior to imaging and resuspended in a defined medium that contained 0.5 mg cell-culture grade BSA (Inivtrogen), 10 µg/mL insulin (Gibco), 50 ng/mL basic fibroblastic growth factor (bFGF) (Invitrogen), 2 µM hydrocortisone (Sigma), 10 µg/mL LPA (Sigma), 1% v/v Penicillin Streptomycin, 1% v/v L-Glutamine, and a phenol-red free, low-glucose DMEM with no riboflavin (Gibco). Fluorescence images were background subtracted, filtered by a Wiener filter to remove shot noise, and band-passed filtered with pass limits reflecting typical sizes for adhesions. The wiener algorithm calculates the mean, µ, and variance, σ^2, around a pixel

$$\mu = \frac{1}{NM} \sum_{n_1, n_2 \in \eta} a(n_1, n_2) \tag{3.1}$$

and

$$\sigma^2 = \frac{1}{NM} \sum_{n_1, n_2 \in \eta} a^2(n_1, n_2) - \mu^2 \tag{3.2}$$

where η is the N by M neighborhood around pixel *a*. The filter is then applied to the pixel using the estimate

$$b(n_1, n_2) = \mu + \frac{\sigma^2 - \nu^2}{\sigma^2}(a(n_1, n_2) - \mu^2) \tag{3.3}$$

where v is the noise variance. In these studies the size of the neighborhood was three by three pixels. Using a MATLAB script, the images were thresholded and quantitative metrics of adhesions were obtained. The calling sequences for these MATLAB scripts begins with the script *FA_main.m* which then calls *FA_info.m*. An algorithm for tracking the trajectories of geometric centroids of adhesions, *track.m* written by John Crocker, was used to follow adhesions as they formed or disassembled. The outline of the cell was obtained either by thresholding images of fluorescence-labeled cells or by manually outlining bright-field images. During cytoskeletal tension agonist or antagonist experiments, cells were allowed to spread for 2 hr before imaging. At the start of imaging, either 10 mM of Y27632 or 10 µg/mL of LPA dissolved in defined medium was added to the live-cell imaging chamber.

3.3.3 Calibration of Pixel Intensity to Force Per Unit Area

To calibrate fluorescence intensity with moles of fluorophore at the glass surface, we saturated a glass coverslip functionalized with a silane fluoroalkane (Trichloro(1H,1H,2H,2H-perfluorooctyl)silane) by adsorbing 50 mg/mL fluorescently labeled BSA for 1 hr, which results in predictable levels of protein and fluorophore on the surface (Sigal et al., 1998). Imaging conditions identical to those used for FP imaging were then used to calibrate pixel intensities to fluorophores per pixel, giving a direct estimate of the number of unfolded FPs within a given pixel. The total force within each pixel was estimated by multiplying the number of fluorophores by the $F_{1/2}$ value of the FP used.

3.3.4 Application of Force Probes to Other Settings

To test the ability of FPs to report cellular traction forces on substrates other than smooth glass, and cell types beyond MEFs, FPs were conjugated to

polydimethylsiloxane (PDMS) surfaces with raised, 1 μm-wide ridges, which induce cells to align along their principal direction. PDMS templates containing raised 1 μm wide by 1 μm tall troughs were cast from a photoresist-patterned silicon wafer, as previously described (Tan et al., 2003). These templates were used to cast inverse features of raised ridges in a thin layer of PDMS on glass coverslips. Substrates were then plasma-cleaned in a manner similar to the glass (described above) for two min prior to stamping with 3-(Ethoxydimethylsilyl)propylamine (Sigma) followed by rinsing sequentially in 200 proof ethanol, 190 proof ethanol, and PBS. Conjugation of the FPs proceeded in an identical fashion as for glass coverslips. Because TIRF was not possible on these substrates, imaging was performed using epifluorescence. FPs revealed polarized localization of traction forces of 3T3 fibroblasts aligned and elongated along the ridge axis, illustrating the potential for assessing forces across multiple types of culture substrates.

3.3.5 Cell Culture and Transfection

NIH 3T3 cells (American Type Culture Collection; ATCC) and MEFs (Rick Assoian, University of Pennsylvania) were maintained in low-glucose DMEM with 5% fetal bovine serum, and 1% v/v penicillin streptomycin (Invitrogen). Vinculin-mRFP or paxillin-mRFP were expressed in MEFs via transient transfection with Lipofectamine (Invitrogen) or TransIT-LT1 (Mirus) according the manufacturer's instructions.

3.4 Results

3.4.1 Surface Conjugation of DNA

Using the unstructured DNA FP (US), the surface conjugation was confirmed via the continuous fluorescence after numerous washes of this linear DNA FP. There was no appreciable signal contribution from the other components of the surface chemistry

including the monofunctional amino silane 3-(Ethoxydimethylsilyl) propylamine (AS) and SM(PEG)$_2$ crosslinker. The potential for the force probes to non-specifically adsorb onto the surface was tested via incubating the DNA with plasma-cleaned glass or with the standard surface but with poisoning of the SM(PEG)$_2$ crosslinker with 2-mercaptoethanol. In none of these cases was there an increase of signal over background Figure 3.2. In contrast to the linear US sequence, hairpin force probes displayed no increased fluorescence above background without the presence of cells (data not shown).

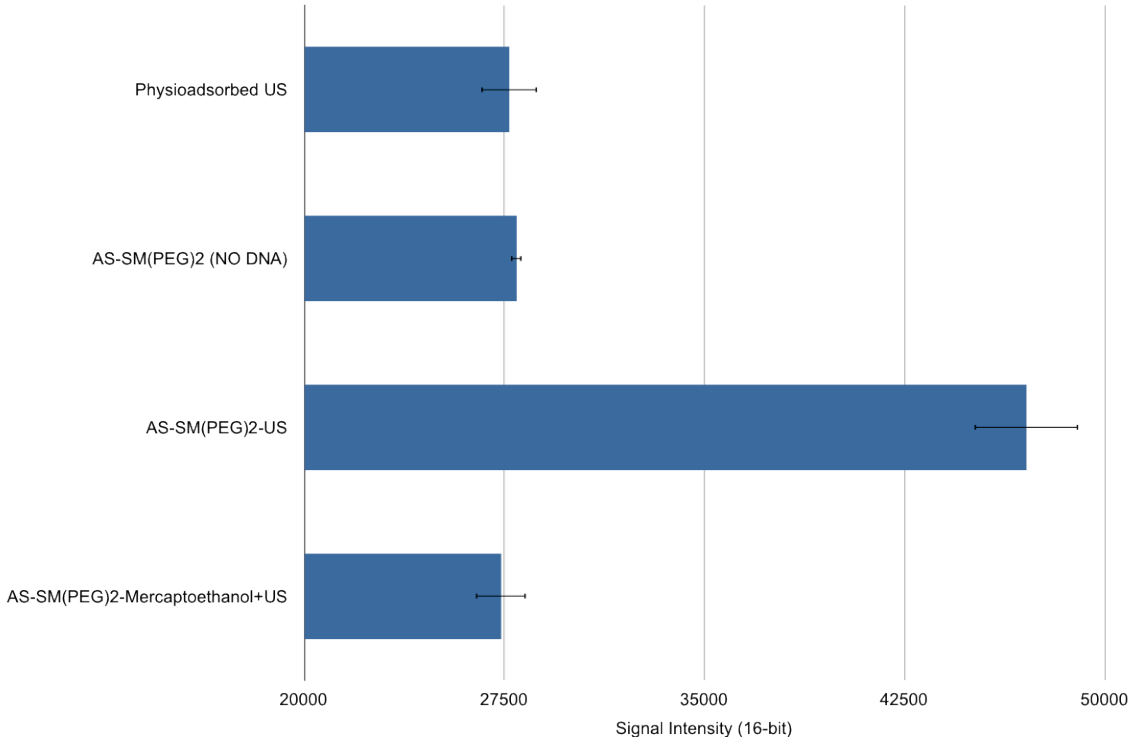

Figure 3.2. Signal Contribution of Each Surface Chemistry Moiety. Fluorescein fluorescence does not increase above background in the case of physioadsorbed linear DNA force probe US-fluorescein to glass (top bar) or with both the amino silane and PEG crosslinker (AS-SM(PEG)$_2$ (No DNA)). The fluorescence is strong in the case of all of the surface chemistry components added with the linear DNA US

probe. When the PEG crosslinker maleimide moiety is poisoned with 2-mercaptoethanol, there is no appreciable increase in fluorescence even after incubating with US.

3.4.2 Live-Cell Imaging

We plated mouse embryonic fibroblasts (MEFs) on FP-conjugated glass substrates and imaged cell-generated force signals via total internal reflectance fluorescence (TIRF) microscopy. Fluorescent signals (values 10- to 25-fold over noise) were detected that were consistent with the sizes, shapes, and locations of FAs (Figure 3.3). Time-lapse imaging revealed that FP fluorescence appeared, shifted, disappeared, and reappeared dynamically, reminiscent of adhesion assembly-disassembly dynamics.

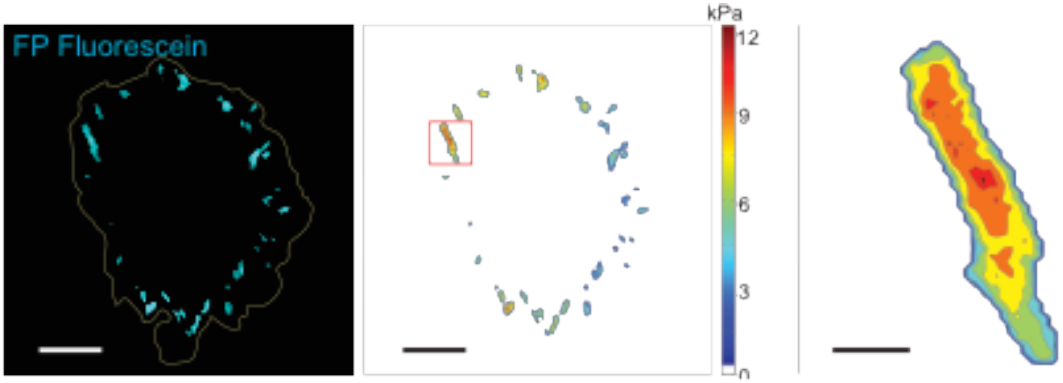

Figure 3.3. Image of MEF attached on FP-coated substrate.

Fluorescent signal from FPs beneath a spread cell (yellow outline) were acquired (left panel), then converted to traction maps calculated from the fluorescence level (middle). The maps show distributions of forces across the cell consistent with the size, shape, and location of FAs. Examination of individual adhesion sites (right) shows a heterogeneous distribution of stress within each site (scale bars: 20 μm, left two panels; 3 μm, right panel.

The fluorescence signal reports the number of unfolded FPs per pixel and therefore may be used to infer traction stress (force per unit area). The resulting stress maps reveal mean traction levels per adhesion on the order of 1 kPa, consistent with previous estimates calculated by assuming that cellular forces were evenly distributed across the area of adhesions (Balaban et al., 2001). These maps also reveal that the spatial distribution of traction stresses between, and within, each FA is strikingly heterogeneous with stresses peaking as high as on the order of 10 kPa (Figure 3.3 right panel).

For image processing, the background was subtracted before a Wiener filter was applied to remove shot noise. Then a band-pass filter was applied to selectively filter objects not conforming to size-characteristics of adhesions. Figure 3.4 gives an overview of this image processing as well as a cross-section of intensity values to clearly show how the images shown were processed before analysis.

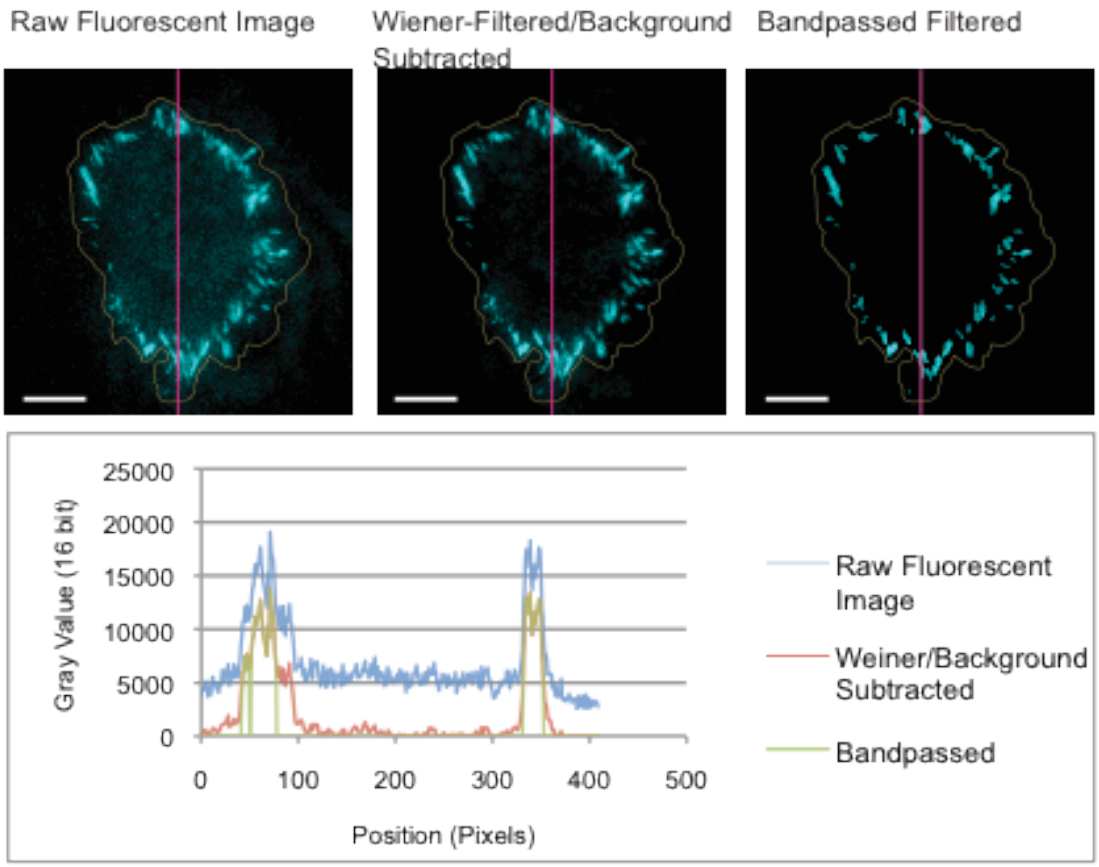

Figure 3.4. Image Processing.

Top row shows work-flow for processing raw images sequentially by removing background signal, Wiener filtering as explained in 3.3.2, and then band-pass filtering for adhesions. Magenta line shows cross-section used to display how signal intensity was altered at each step (bottom graph). Background from unfolded hairpin was not significantly above bare glass (approximately 4000 on a 16-bit scale), and the signal from FA opening of hairpins reached values 10x above background (approximately 50,000 on a 16-bit scale) for our usual imaging conditions (CFI Apo TIRF 60X oil (1.49NA) objective, 500 msec exposures, and a laser intensity of approximately 190 μW at 488 nm wavelength).

To confirm that the signal reported by the fluorescence was due to the specific binding of cell integrin rectors to the RGD peptide of the force probe, negative control force probes were synthesized which contained the same sequence, PEG crosslinkers, and the fluorophore-quencher pair but with no RGD. Cells failed to attach on surfaces coated purely with these negative control probes. So, an equimolar mixture of these negative control force probes and the peptide sequence CGGRGDS was conjugated to the surface. Cells fully spread on these surfaces, but there was no adhesion signal given by the negative control force probes (Figure 3.5).

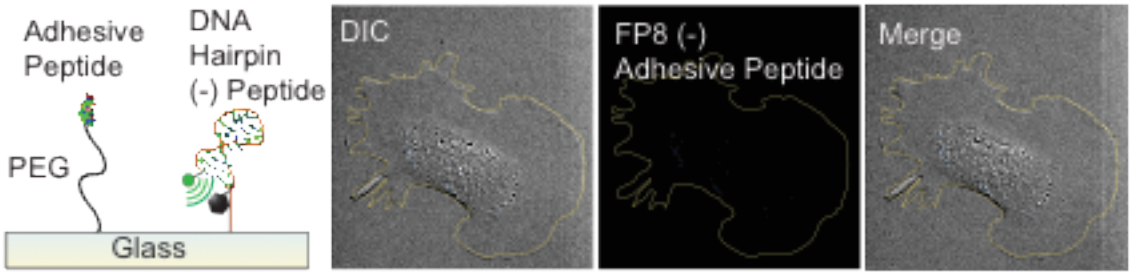

Figure 3.5. Specific RGD-integrin interaction is required for traction force induced FP fluorescence.

A negative control FP was synthesized lacking the RGD peptide. Surfaces coated with just this FP failed to support cell adhesion. To allow for cell adhesion to substrate in the presence of this FP, RGD was coupled to the surface through a PEG crosslinker and mixed with equal molar amounts of the negative control FP. Cells spread readily on these surfaces, but no cell-induced fluorescence was observed. Together, these results confirmed that the only cell adhesive interaction with the FP is through RGD.

Diminished surface density of adhesive integrin ligand decreases the degree of spreading and the forces that cells exert on their surroundings (Bhadriraju et al., 2007a;

Ingber and Folkman, 1989a; Pirone et al., 2006). To confirm that our system replicates this effect we varied the surface concentration of force probes with the adhesive RGD peptide. To control the RGD density linearly, we varied the ratio of our normal force probes to the amount of force probes without the adhesive peptide or fluorophore but with the same thiol moiety for surface attachments. Figure 3.6 shows that as the amount of force probe on the surface was diluted by one-third and one-twelve (1 μM and 0.25 μM compared to the standard 3 μM we used for optimal cell spreading) the cells displayed dimmer and smaller adhesions. The total cell force as measured by the force probes also decreased with the dilution of the RGD peptide. These data give further evidence that the cells spread on these surfaces through the specific interaction between integrin receptors and the adhesive peptides on the force probes.

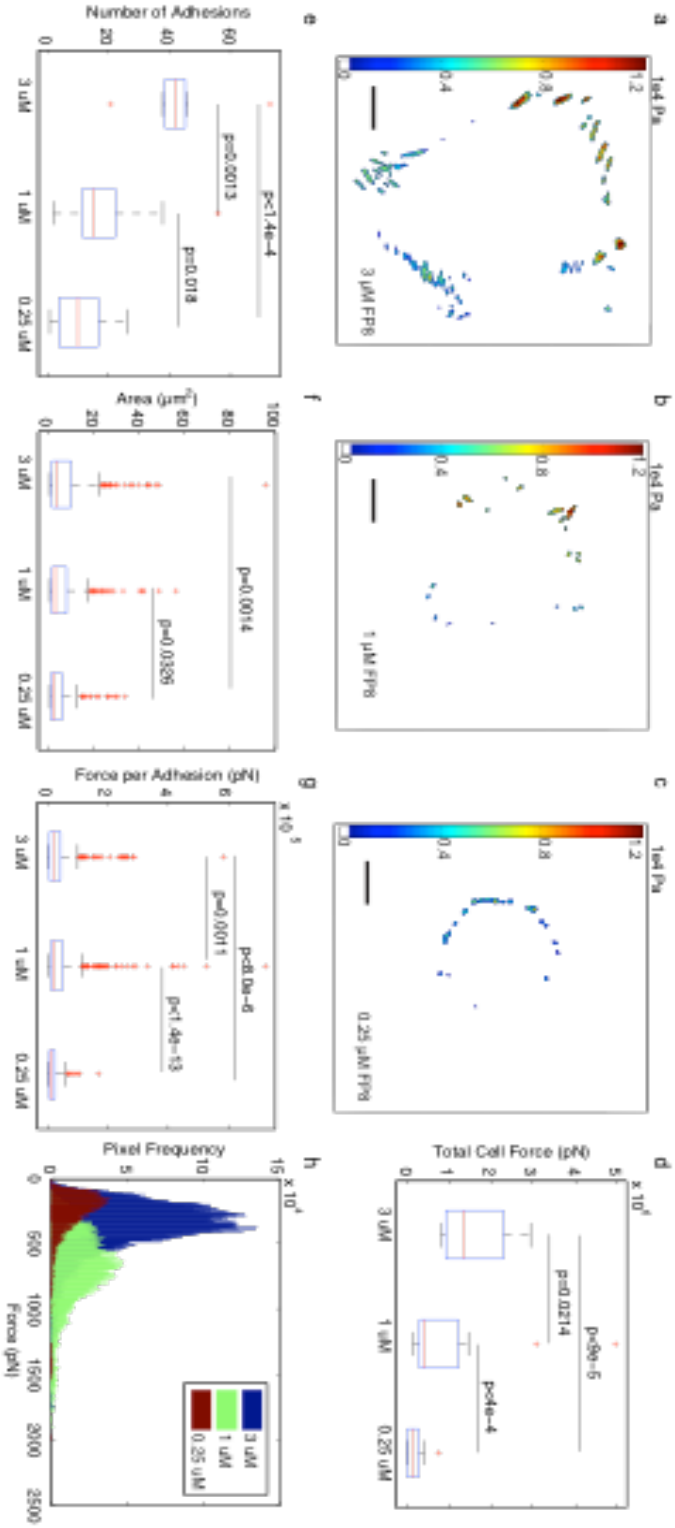

Figure 3.6. FP reported forces decreases with diminished surface concentrations of RGD peptide.

Traction forces reported for cells spread on surfaces conjugated with (a) 3 μM, (b) 1 μM, and (c) 0.25 μM of force probes with RGD. As the amount of force probes with RGD is decreased the (d) total force measured for cells and number of adhesions (e) decreases accordingly. (f) The areas of individual adhesions were not significantly different from between 3 μM and 1 μM, but both were larger than the areas of adhesions of cells cultured on 0.25 μM FP8 surfaces. (g) The force per adhesion was highest for cells cultured on 1 μM concentrations of FP8 and lowest for 0.25 μM concentrations. (h) Histogram of pixel frequency versus force for each concentration shows high force shift of 1 μM concentration (p-value reported from Wilcoxn rank sum test). Red lines in box plot mark the median, and whiskers show the ±2.7σ range.

3.4.3 Force Probe Signal Response to Altering Cytoskeletal Tension

To confirm that the fluorescence signals reflected traction forces, we examined the effects of either suppressing or enhancing cell contractility. Within minutes after the addition of Y-27632, an inhibitor of Rho kinase (ROCK)-mediated contraction (Uehata et al., 1997), traction signals distributed in large adhesions rapidly decayed to dim, smaller punctate signals (Figure 3.7a,b). Conversely, treatment of starved cells with lysophosphatidic acid (LPA), a strong receptor-mediated stimulant of Rho-mediated contraction, led to a rapid enhancement of the fluorescence signal, organized in growing foci again reminiscent of FAs (Figure 3.7b,c). Together, these results suggest that the observed fluorescence signals reflect bona fide changes in cellular traction forces.

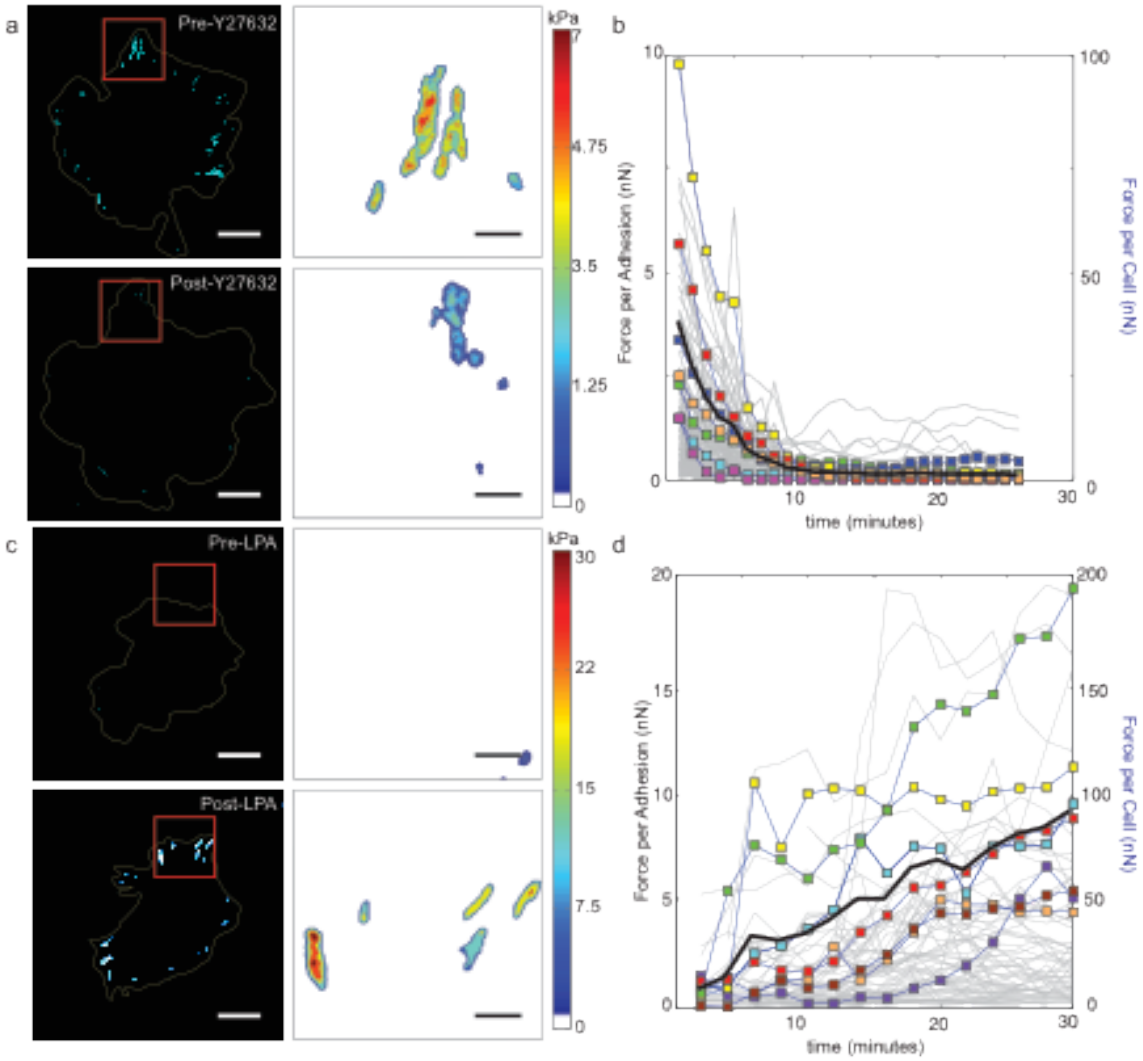

Figure 3.7. Response of Force Probe Signal to Alterations of Cytoskeletal Tension. (a,c) Fluorescence (left) and traction map (right) reported by FPs of cells spread before (top panels) and after (bottom) addition of either the ROCK inhibitor Y27632 (15 min after treatment) (panel a) or LPA (1 hr after treatment), an activator of Rho (panel c) (scale bars: 20 μm; left; 5 μm, right. (b, d) Plots of mean stress per adhesion site as a function of time for individual cells treated with Y27632 (panel b) or LPA (panel d). Individual adhesions (grey lines); individual cells (colored squares and lines); mean of all cells (black solid line).

3.4.4 Imaging Multiple Force Probe Dyes

FPs with different fluorophores (fluorescein, Alexa 546, and Alexa 647) and different $F_{1/2}$ values, ranging from 8.1-19.3 pN, all exhibited similar responses to attached cells, demonstrating the potential for imaging multiple colors independently to report a range of potential forces (Figure 3.8).

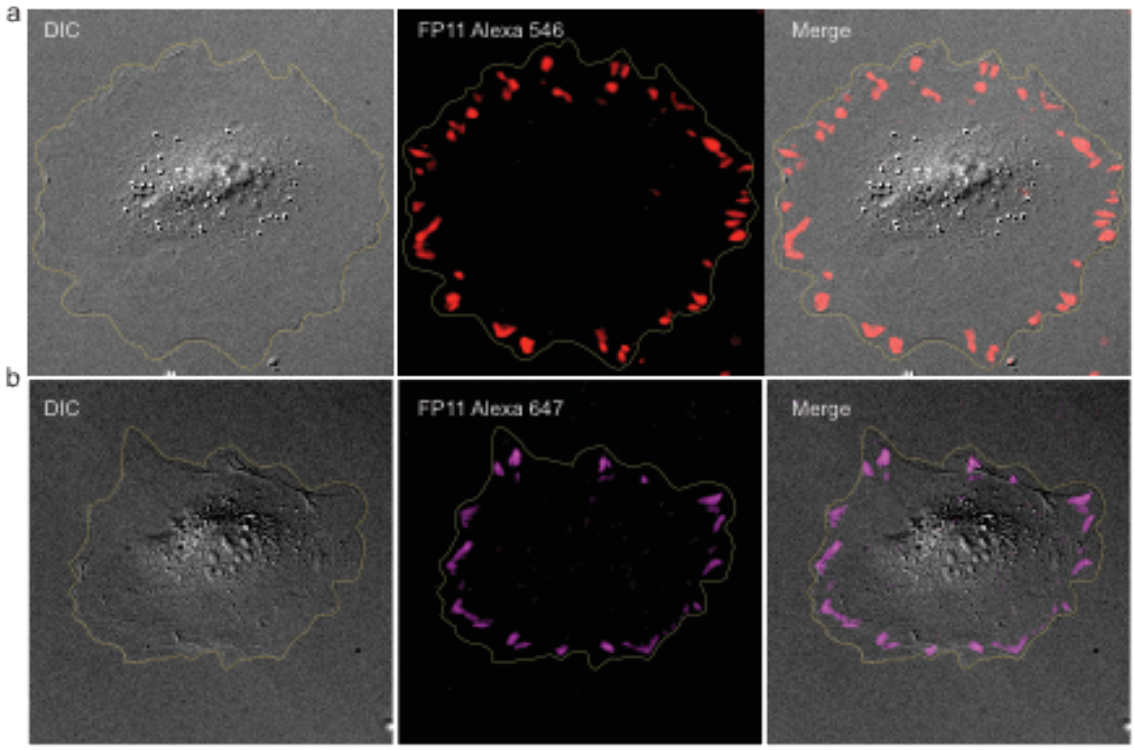

Figure 3.8 FPs conjugated to different dyes are equally functional.
We have developed three FP-dyes. In addition to the fluorescein FPs shown in the main text, we have synthesized fully functional FPs labeled with Alexa 546 demonstrated in (a) and Alexa 647 demonstrated in (b).

We have designed a series of FPs with a range of $F_{1/2}$ values. We sought to investigate whether altering the $F_{1/2}$ values changed the signal intensity accordingly. We

prepared surfaces with ratios of different force probes both in terms of sequences and dyes. One type of surface prepared was conjugated with FP11 with both fluorescein and Alexa 647. Another type of surface was conjugated with FP11-Alexa 647 and FP19-fluorescein. We predicted that the ratio of the fluorescein signal intensity to the Alexa 647 signal intensity would be lower in the case of FP11-Alexa 647 paired with FP19-fluorescein than the case with FP11-Alexa 647 paired with FP11-fluorescein. We found this to be the case as shown in Figure 3.9. When considering the ratio of the $F_{1/2}$ values, an increased factor of 1.72 (19 pN/11 pN) would be expected between the brightness intensity of red versus green pixels with FP11-Alexa 647 paired with FP11-fluorescein compared with the brightness intensity of green versus red pixels with FP11-Alexa 647 paired with FP19-fluorescein. In our case, the ratios of the fitted linear slopes between the red and green signal on FP11-Alexa 647 paired with FP11-fluorescein surfaces versus the FP11-Alexa 647 paired with FP19-fluorescein surfaces was 1.91 (0.39719 in panel Figure 3.9c divided by 0.20785 in Figure 3.9d).

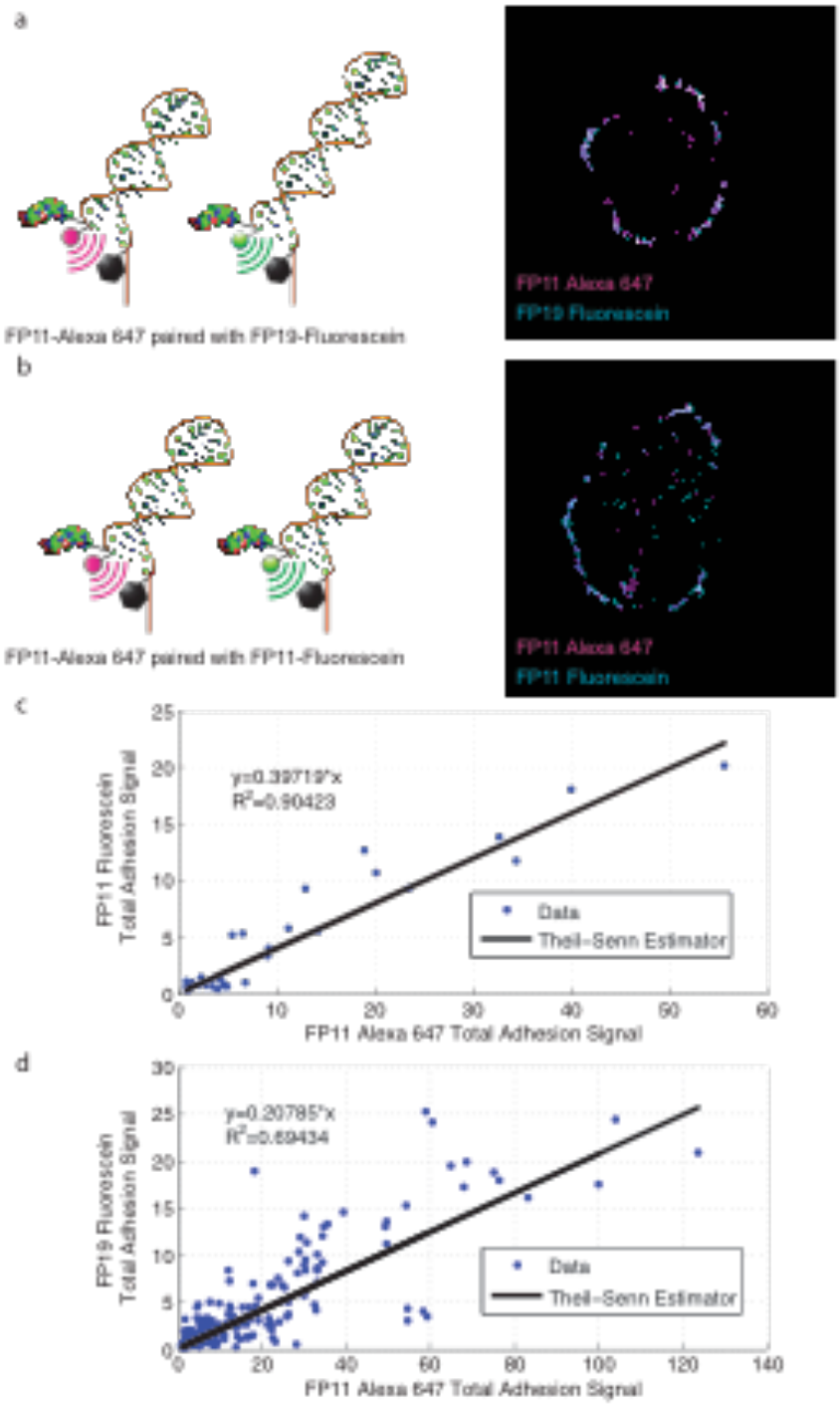

Figure 3.9. Measurement of traction forces using two sequences demonstrates that signal intensity is higher for sequences with lower $F_{1/2}$ values.

(a) Schematic (left) and image (right) of surfaces were conjugated with equal amounts of two FPs: one sequence with an $F_{1/2}$ value of ~11 pN (FP11) labeled with Alexa 647 and another with ~19 pN (FP19) labeled with fluorescein. Images show co-localized adhesion-like traction stress signals in two separate fluorescent channels. The two channels reported different intensity values that result in part from differences in fluorophore and wavelength-dependent optics. (b) To control for these differences, signals were obtained for substrates conjugated with FP11-fluorescein and FP11-Alexa 647 in equal molar amounts. This setup also yielded adhesion-like traction stress signals in two separate fluorescent channels. (c-d) Plot of the intensity of the two colors for each pixel for FP11 Alexa 647 versus FP11 fluorescein (c) and FP11 Alexa 647 versus FP19 fluorescein (d). These pixel values changed linearly with the unfolding strengths of FPs (fits from Theil-Senn Estimator, which plot linear models based on the median slope to minimize the effects of outliers).

3.4.5 Localization of Force Probe Signal in Relation to FA Proteins

Because FPs are single fluorescent molecules, the resolution of traction force measurements is dictated by photon capture efficiency and microscope optics, which can be diffraction-limited. FPs therefore offer a significant improvement in spatial resolution compared to traditional traction force methods, which typically report forces on a scale of several μm (Sabass et al., 2008). In contrast, the system described here computes traction forces from the average fluorescence signal per pixel at a spatial resolution governed by the magnification and the camera (in this work, 200 x 200 nm image pixels).

We transfected MEFs with an expression vector encoding recombinant vinculin, a scaffolding protein that localizes to FAs, fused to red fluorescent protein. We then compared the vinculin distribution to the distribution of traction foci. The locations and geometries of the punctate traction foci correlated strongly with those of FAs (Figure 3.10). Upon closer examination, however, these two signals were not coincident, as the FP foci were consistently slightly more distal from the cell center than those of vinculin. Measuring the centroids of the two signals confirmed that the centers of adhesion, as reported by force, were located ~200 nm closer to the cell edge than the centers of the corresponding adhesions reported by vinculin localization. This localization of force to the distal ends of FAs was confirmed using fluorescent paxillin markers as well as different FP variants (Figure 3.11). Interestingly, whereas all foci of force were associated with adhesions, some FAs did not produce an associated force signal. To explore this phenomenon, we followed the evolution of traction forces and FAs, and observed three distinct classes of adhesions.

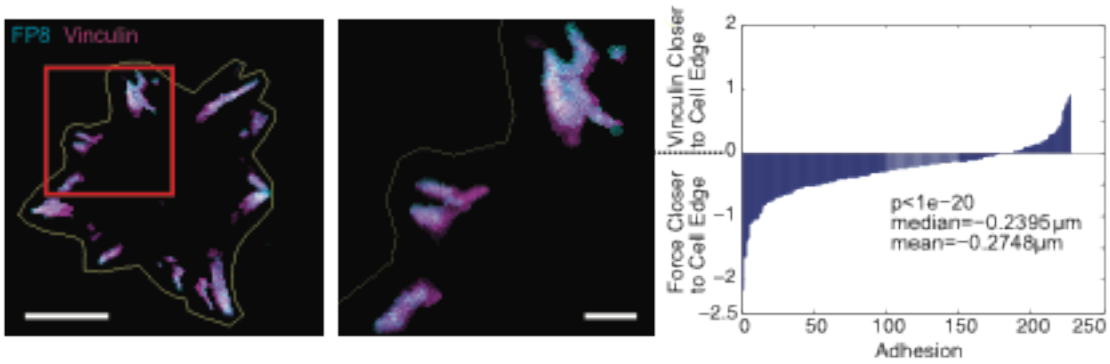

Figure 3.10. Localizations of traction forces with respect to FA proteins. Fluorescence image of FP-coated substrate (cyan) and overlying cell (yellow outline) expressing mRFP-vinculin (magenta). High-magnification inset (middle) illustrates the high degree of co-localization of FA relative to FP-measured tractions, with tractions slightly more distal from the cell center than vinculin. The right panel plots the difference

in distance (in μm) of the geometric centroid from the cell edge of the two signals for selected adhesions. The skew in the distribution reflects a distal bias for tractions relative to adhesions (p-value reported from Wilcoxon signed-rank test of difference between distances of centroids of adhesions from the cell edge as reported by FPs and mRFP-vinculin). Scale bar is 20 μm (left) and 5 μm (center).

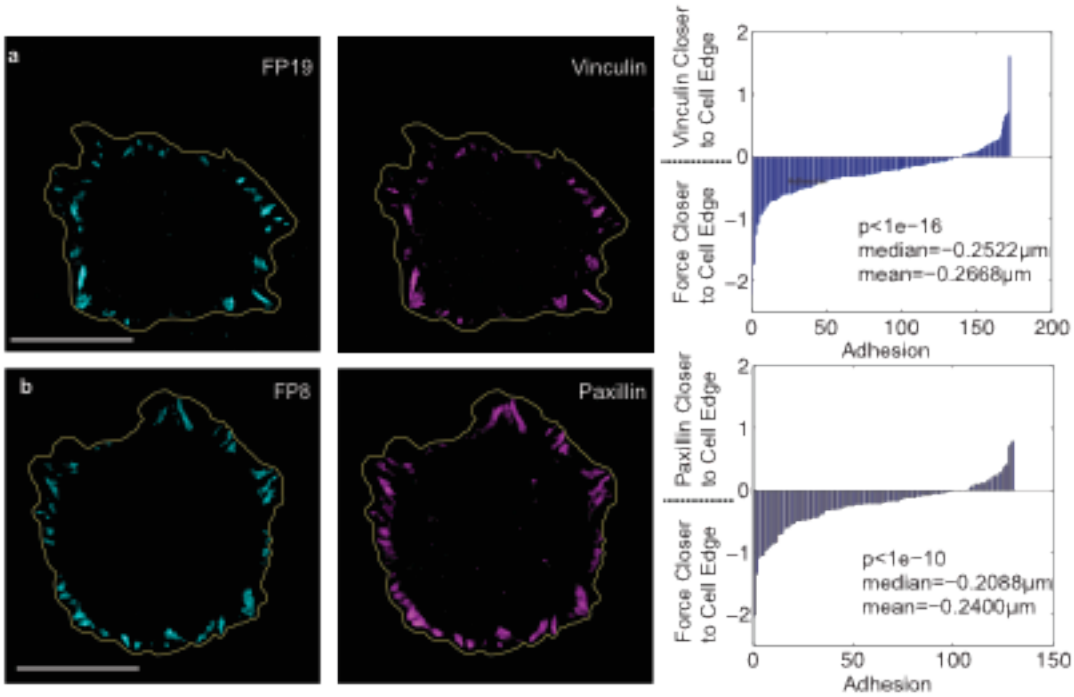

Figure 3.11. Localization of FP-reported stress with different focal adhesion proteins.

Fluorescence of both FPs and transfected cells expressing (a) mRFP-vinculin or (b) mApple-paxillin. Images show the localization of FP-measured tractions to focal adhesions in both cases. The use of different sequences with different $F_{1/2}$ values did not change this localization. The right panel plots the difference in distance (in μm) of the geometric centroid from the cell edge of the two signals for selected adhesions. The

skew in the distribution reflects a distal bias for tractions relative to adhesions (p-value reported from Wilcoxon signed-rank test of difference between distances of centroids of adhesions from the cell edge as reported by FPs and mRFP-vinculin or mApple-paxillin). Scale bar is 20 μm (left) and 5 μm (center).

In one class of adhesions, traction force and vinculin location correlated to a high degree throughout the lifetime of the adhesion zone. For these adhesions, force increased during adhesion assembly and subsided during its disassembly (Figure 3.12 a,b). In a second class, force and vinculin co-localized at the initiation of the adhesion, but as the adhesion continued to grow and extend towards the center of the cell, force remained localized to the distal tip of the elongating adhesion (Figure 3.12 c,d). Finally, in a third class of adhesions, no local variation in force was observed, despite vinculin clustering (Figure 3.12 e,f). Time-lapse studies highlighted the heterogeneity of stress experienced within any given adhesion: some exhibited a single concentrated peak of stress, some showed multiple peaks that appeared, disappeared, merged, or split, and some showed a plateau in stress, with no concentrated peaks. All together, these findings reveal a complex orchestration of cellular forces within FAs.

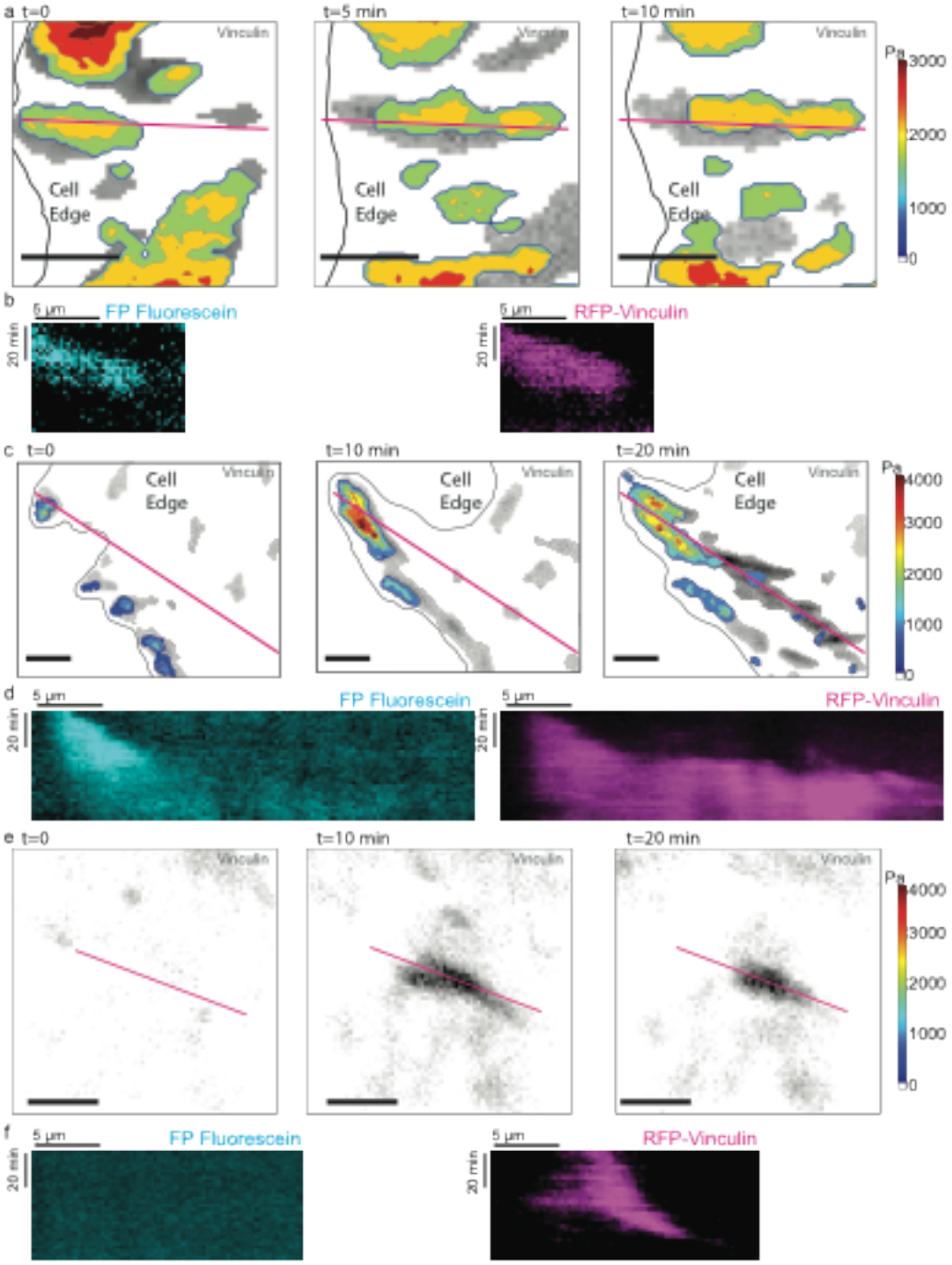

Figure 3.12. Temporal Correlation of traction forces with respect to FA proteins. (a-f) Representative examples of the three classes of adhesions. Images show a sequence over time of the vinculin fluorescence (gray scale) overlaid with the FP-reported stress map (a, c, e). The edge of the cell is illustrated with a black line. Scale

bars are 5 μm. The magenta line indicates the position used for kymographs (b, d, f) showing the evolution of the FP (left) and vinculin (right) signals over time. Vertical scale bar is 20 min; horizontal bar is 5 μm.

Since our DNA force probes offer real-time force measurements, we sought to determine whether the dynamics of adhesion assembly as reported by both the force probes and canonical adhesion proteins would differ. Grashoff et al. reported that diminishing force across vinculin precedes adhesion disassembly (Grashoff et al., 2010). We investigated whether force across cellular integrin receptors onto the extra-cellular environment as reported by our force probes would be temporally correlated with adhesion assembly or disassembly as a time-lag. High-temporal resolution time-course images (imaged every ten seconds) were taken with cells transfected with fluorescently labeled adhesion proteins including vinculin and paxillin. For each adhesion, the 'focal adhesion size index' as defined by Grashoff et al. (mean-intensity multiplied by the area of the adhesion) was measured in both fluorescent channels, the force probe and the fluorescent protein. The time-course was then normalized to the maximum value for each channel and plotted after local regression smoothing using weighted linear least squares and a first-degree polynomial model. The cross-correlation was then calculated. In our studies, these cross-correlation values were found to peak at zero, suggesting correlated signals and no systemic lag-times between force and protein deposition for either assembling or disassembling adhesions and both vinculin and paxillin (Figure 3.13).

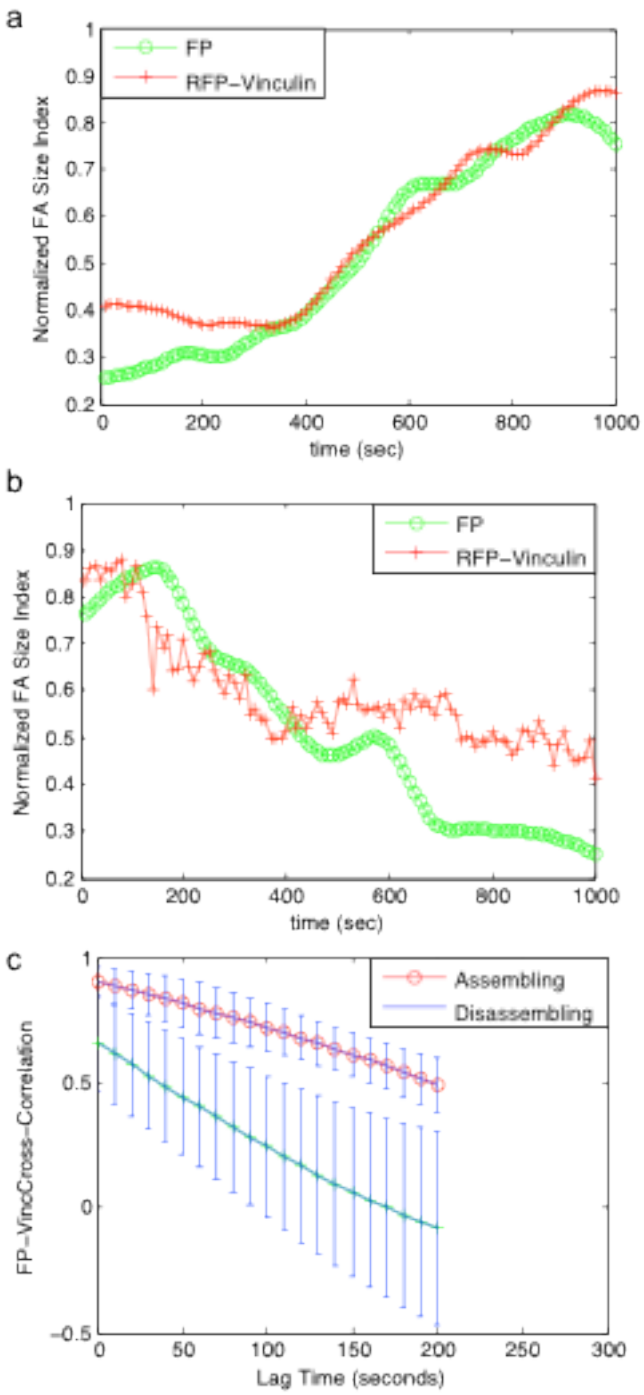

Figure 3.13. Cross-Correlation of Force and Vinculin Dynamics.

Examples of focal adhesion size index for (a) assembling and (b) disassembling adhesion. (c) Cross-correlation coefficient of adhesions peaks at zero indicating no systemic time lag.

3.4.6 Application of Force Probes to Other Settings

PDMS substrates with raised ridges were fabricated and conjugated with FPs in a similar manner as with glass with one variation: the silane was stamped onto the PDMS ridges directly as opposed to reacting in solution. Reacting the silane with the PDMS substrates in solution lead to poor FP functionalization. 3T3 fibroblasts platted on the functionalized PDMS substrates aligned along the ridges with a corresponding alignment of their adhesions as reported by the force probes. This suggests the utility in using these force probes for measuring tractions in physically geometrically complex substrates previously unaccommodating to measuring cell forces using other TFM methods.

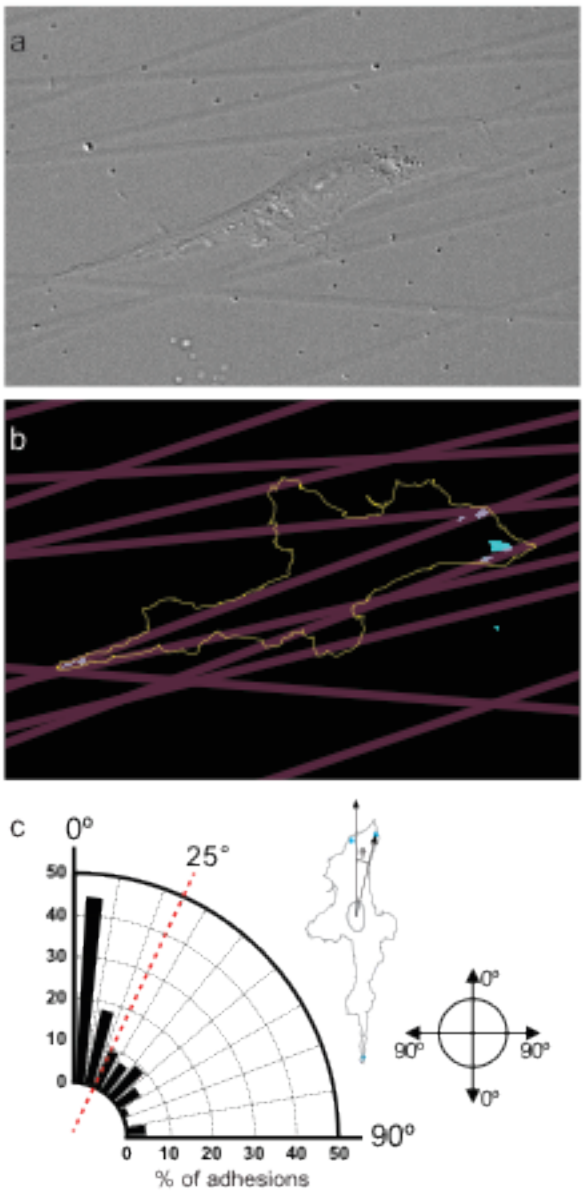

Figure 3.14. Application of FPs on substrates with complex topography.

DIC (a) and thresholded fluorescence (b) images of a polarized fibroblast on substrates composed of raised 2 um wide PDMS ridges stamped with FP8. Cell is outlined in yellow and ridges are false-colored magenta. Scale bar is 10 μm. (c) Angular histogram of the distribution of force-bearing adhesions as reported by FPs with respect to the axis of polarization. The mean angle of n=52 adhesions analyzed was 25º (red dashed line).

3.5 Discussion

Surface Conjugation of DNA. Prior to using a monofunctional amino silane, we sought functionalize the force probes to glass using (3-mercaptopropyl)trimethoxysilane (MTS). MTS is a trifunctional silane which increases reaction time and requires less stringent preparation of the glass (Bhushan et al., 2006). Deprotection of the thiol groups on the force probes requires a reducing agent, and while TCEP does not risk consuming thiol-reactive groups or dimerization such as is the case with dithiothreitol (DTT), it can lead to reductions of pH of a given buffer (O'Donnell et al., 1997). So, we initially sought to avoid deprotection and the need for extensive cleaning of our glass surfaces by vapor depositing MTS and reacting the thiol groups of the force probes directly with the MTS via a thiol exchange buffer similar to the scheme shown in Figure 3.15 (Rogers et al., 1999).

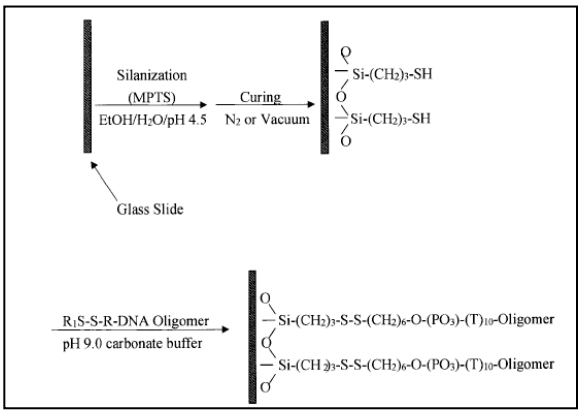

Figure 3.15. Thiol Exchange Conjugation of DNA.

By vapor depositing MTS onto glass and then reacting in a thiol exchange buffer, the use of a reducing agent for deprotection of the force probe thiols is obviated, but at the cost of a less stable bond. Image reprinted from (Rogers et al., 1999).

These surfaces when imaged displayed high background. Cells plated onto glass conjugated using this surface chemistry suffered poor attachment. This was attributable to one of two potential limitations of this method. The first was the potentially liable disulfide bond between the force probes and the surface. Another problem suspected in the early phases of our work was the potential complication of polymerization of the tri-functional silane MTS. While more reactive, these silanes may generate up to 35 Å thick polymerized layers on the surface (Figure 3.16) (E. McGovern and Thompson, 1998). Further, these polymerized layers can bury the functional groups and interfere with the conformation of molecules bound to the surface (Yee et al., 1991). We speculated that the higher background and diminished cellular attachment to these surfaces was due to the loss of DNA structure upon adsorption onto these layers.

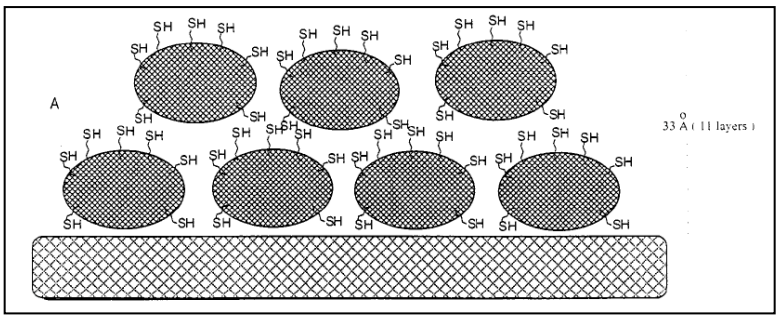

Figure 3.16. Polymerized Layers of Multifunctional Silane.
Trifunctional silanes form multi-layered polymerized films. Image reprinted from (E. McGovern and Thompson, 1998).

Force Measurements of Living Cells. Cell-generated traction forces not only transmit through adhesions to the surrounding extracellular matrix, but also regulate the assembly and signaling of those adhesions (Geiger et al., 2009b; Parsons et al., 2010).

While some studies have demonstrated a correlation between the magnitude of the force and the size of the FA (Balaban et al., 2001; Fu et al., 2010), others have suggested that only smaller adhesions experience high stresses (Beningo and Wang, 2002b). Here, we observe the association of forces with FAs, but in distinct ways. Stricker et al. have shown recently a high correlation between size and force only for growing FAs (Stricker et al., 2011). The improved co-imaging of force and adhesions presented here confirms that relationship, but we find that forces remain tightly associated only with the distal tips of extending adhesions. The distinct spatiotemporal fluctuations of forces within adhesions revealed here may provide new insights into the internal organization and dynamics of these adhesions. For example, such heterogeneities in stress could generate highly localized pockets of force-induced integrin activation (Friedland et al., 2009) or unfolding of focal adhesion proteins (Grashoff et al., 2010), and may play a central role in locally modulating adhesion structure and signaling.

Diminished surface density of adhesive integrin ligand decreases the degree of spreading and the forces that cells exert on their surroundings (Bhadriraju et al., 2007a; Ingber and Folkman, 1989a; Pirone et al., 2006). To confirm that our system replicates this effect we varied the surface concentration of force probes with the adhesive RGD peptide. To control the RGD density linearly, we varied the ratio of our normal force probes to the amount of force probes without the adhesive peptide or fluorophore but with the same thiol moiety for surface attachments. Figure 3.6 shows that as the amount of force probe on the surface was diluted by one-third and one-twelve (1 μM and 0.25 μM compared to the standard 3 μM we used for optimal cell spreading) the cells displayed dimmer and smaller adhesions. The total cell force as measured by the force probes also decreased with the dilution of the RGD peptide (Figure 3.6d). These data give further evidence that the cells spread on these surfaces through the specific

interaction between integrin receptors and the adhesive peptides on the force probes. While the global cell response to the diminished adhesive ligand followed expected trends, we sought to parse the response of traction forces within individual adhesions to further understand the effects of ligand density on cellular adhesion. Cells cultured on 3 μM, 1 μM, and 0.25 μM concentrations of FP8 formed successively less numbers of adhesions at each dilution (covering an approximately fourfold decrease from 3 μM to 0.25 μM), but the areas of these adhesions were diminished only at the lowest concentration (Figure 3.6e,f). Surprisingly, while the adhesions formed by cells on surfaces of 0.25 μM concentration FP8 exerted the lowest tensions, the adhesions formed by cells on 1 μM concentration FP8 surfaces displayed higher total tension per adhesion than the adhesions of cells cultured on 3 μM concentration FP8 surfaces (Figure 3.6g,h).

As a result of the larger number of adhesions formed in cells cultured on 3 μM concentrations of adhesive ligand, the total cell force reached the highest levels between the three concentrations. The intermediate decrease in adhesive peptide to 1 μM lowered the total cell force and number of adhesions modestly relative to a much more completely diminished adhesion formation at 0.25 μM resulting in cells with much less numbers of adhesions with less force recorded per adhesion. However, at the intermediate concentration of 1 μM of adhesive peptide, while cells did form less adhesions and less total cell force, the force per adhesion was actually higher than the forces of adhesions formed by cells on 3 μM concentrations of adhesive peptide. Perhaps the highest concentration of adhesive peptide is more conducive for mature FA formation allowing the total number of adhesions to reach higher quantities, while a moderate adhesive ligand density permits fewer adhesions to cross from the nascent to mature FA threshold. The greater forces of adhesions in this moderate adhesive ligand

density may reach higher levels as the presumably the concentration of available actomyosin filament precursor is then dispersed to fewer mature adhesions, thus increasing their forces.

This study establishes DNA hairpins as versatile molecular reporters to study cellular forces. While other methods to measure traction forces using elastic substrates have been instrumental in establishing the importance of forces, the higher resolution offered by FPs and the ability to attach FPs to arbitrary substrates will further expand our understanding of the contribution of cellular forces to cell adhesion and function.

CHAPTER 4

Micromolded Synthetic Bioactive Poly(ethylene glycol) Scaffolds to Engineer Angiogenesis

4.1 Introduction

In this chapter, we overview the design of a micromolded PEG hydrogel system to engineer angiogenesis. By incorporating bioactive peptides into these gels, cells were able to spread, degrade, and migrate in 3D environments. Using microfabrication techniques, we fabricated 3D patterns to control vessel sprouting from chick aortic arch explants. We sought to investigate whether altering the diameter of bioactive gel channels affected angiogenic sprouting velocity.

4.1.1 Synthetic Hydrogels to Study 3D Systems

Many of the model systems to study cellular physiology to date entail investigating cells cultured on flat substrates. However, cells naturally experience 3D *in vivo* environments, and their behavior and morphology is radically different in 3D, limiting the conclusions of 2D techniques (Cukierman et al., 2001). Tissue morphogenesis is an inherently physical process as cells degrade and migrate through matrix before assembling into multi-cellular structures both in development (Farge, 2003; Martin et al., 2009; Rauzi et al., 2008) and during angiogenesis (Kniazeva and Putnam, 2009). Synthetic materials offer greater flexibility for designing scaffolds with controlled growth factor delivery, as well as cellular environments (Lutolf and Hubbell, 2005). Hydrogels based on the FDA approved material PEG, a bio-inert hydrogel with hydration properties similar to native tissue, are especially common in the tissue-engineering field.

Incorporating the fibronectin fragment RGD peptide or collagenase-sensitive peptide linkers can render PEG adhesive and degradable (Elbert and Hubbell, 2001; Hern and Hubbell, 1998; West and Hubbell, 1999). Degradable and adhesive PEG based materials with and without bound growth factors have been explored for tissue regeneration (Gobin and West, 2002; Lutolf and Hubbell, 2003; Lutolf et al., 2003; Mann et al., 2001a; Mann et al., 2001c).

4.1.2 3D Patterning of Hydrogel Scaffolds

Over the past twenty years, the use of microfabrication technology has allowed the study of 2D geometries and their effects on cell function (Weibel et al., 2007). Now, researchers in both basic biology and tissue engineering are exploring techniques to pattern in three-dimensions (Lutolf, 2009). In the context of angiogenesis, microfluidic-generated layers of collagen gels seeded with endothelial cells, smooth muscle cells, and fibroblasts were produced in an effort to mimic the intima, media, and adventitia of a vessel wall respectively (Tan and Desai, 2003). Others have even used 3D printing technology in an effort to produce scaffold vasculature prior to implantation (Mironov et al., 2003).

Synthetic, photopolymerizable hydrogels, such as poly(ethylene glycol) diacrylate (PEGDA), are an especially useful platform to explore patterning cellular environments. One approach is to generate gradients of some bioactive molecule in a gel precursor solution prior to polymerizing to align or direct cell migration on the surface (Burdick et al., 2004; DeLong et al., 2005; Jeon et al., 2002). Elastomeric stamps can generate 3D topographical structures, known as capillary force lithography, by molding the gel precursor prior to polymerization (Khademhosseini et al., 2004). Finally, other groups have used photo-activated chemistries and highly focused lasers to generate patterns in synthetic hydrogels (Kloxin et al., 2009).

By placing a mask with opaque regions between the light source and the gel precursor solution, polymerization can be restricted only to regions of the gel exposed to light. This approach was first used to make defined 3D architectures of PEGDA gels as small as 5μm to encapsulate cells or to prevent adsorption of cells and proteins (Liu and Bhatia, 2002; Revzin et al., 2001; Suh et al., 2004). By polymerizing layers of gels in defined patterns, cell-sized wells to control cell placement and differentiation have been developed (Mapili et al., 2005). Commercially available liquid crystal display (LCD) screens offer an alternative to photomasks with dynamic computer-aided control (Itoga et al., 2004a, b). Sequential layering of 2D patterned gels has produced complex liver tissue structure analogs (Tsang et al., 2007). Others have utilized 2D photomask patterns with variations in light intensity to generate either surface modifications or to extend down through the three-dimensional bulk of the gel (Hahn et al., 2005; Hahn et al., 2006b). Using this method, groups have patterned specific regions of cell attachment sites. First, a bio-inert PEG gel is polymerized, then, an RGD peptide-conjugated PEG-acrylate moiety is allowed to soak the surface or perfuse into the bulk gel. Upon light-induced polymerization with the chosen photomask, and subsequent washing of unbound molecules, the adhesive peptide is then immobilized in only regions of the gel exposed to light.

While 2D lithography patterns can be extended through the entire thickness of 3D constructs, two-photon lithography offers true 3D patterning technology of any arbitrary design at cellular scales. By using very high intensity focused beams of light, two photons of longer wavelength that arrive virtually at once can excite a fluorophore to an energy state normally reached when excited by photons of shorter wavelength. As this quantum event is proportional to the square of the laser intensity, only extremely focused light is sufficient, giving unparalleled spatial fidelity in fluorescence or light

mediated chemistry. Due to the high intensities of laser light needed, excitation events are pulsed 10^{-13} seconds every 10^{-8} second long interval (Zipfel et al., 2003). While originally used for microscopy, this technique has been expanded to generate 3D structures of photopolymerized polymers (Cumpston et al., 1999; Denk et al., 1990). West and colleagues have also extended this approach to PEG hydrogels, as well as Anseth et al. in conjunction with bio-compatible 'click' chemistries (DeForest et al., 2009; Hahn et al., 2006a; Lee et al., 2008). Similar to the generation of patterns using 2D lithography, in the two-photon laser scanning lithography method, an inert PEG gel is polymerized and then infused with some bioactive moiety.

4.2 Objectives

We desired to synthesize a PEG hydrogel to manipulate and study angiogenesis. Specifically we sought to determine how micromolded gel geometries affected angiogenic sprouting. As a base material we synthesized PEGDA and PEG Diacrylamide (PEGDAAm). We used a Michael-Type addition scheme to react bis-cysteine MMP-sensitive peptides with PEGDAAm and generate large molecular weight step-growth polymers. In a second photopolymerization step, these gel precursors were crosslinked with Acrylate-PEG-CGRGDS to generate cell adhesive and MMP-degradable gels. Using microfabrication approach, we patterned angiogenic sprouting from chick aortic arch tissue explants into different width channels. To summarize our objectives in this study were:

1. Synthesize PEGDAAm and PEGDA peptide conjugated precursors.
2. Generate microfabricated 3D patterns to pattern sprouting from aortic arch tissue explants.

4.3 Materials and Methods

4.3.1 Synthesis of poly(ethylene glycol) diacrylate (PEGDA)

Triethylamine (TEA; 2 molar excess to PEG) and acryloyl chloride (4 molar excess to PEG) were reacted with dry poly(ethylene glycol) (PEG; molecular weight (MW) 3400 or 6000) in anhydrous dichloromethane (DCM) under argon as described previously (Mann et al., 2001b). The scheme is given in Figure 4.1.

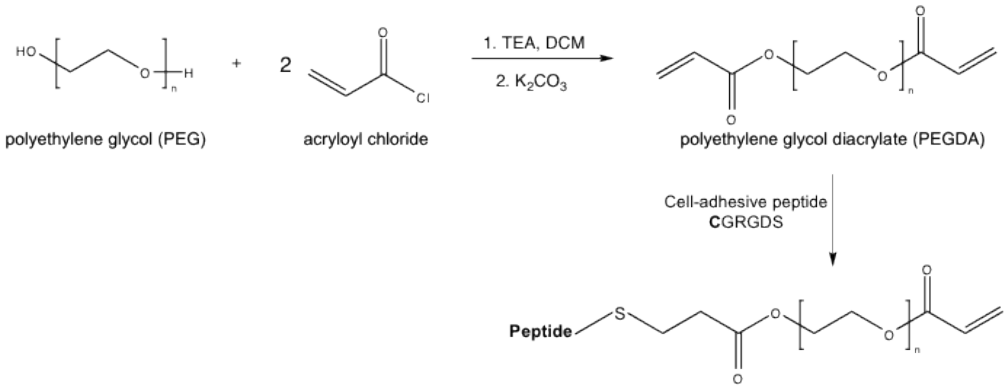

Figure 4.1. Detailed synthesis scheme of PEGDA and Acrylate-PEG-CGRGDS. PEG (MW 3400) was acrylated and then reacted with CGRGDS via Michael-type addition to synthesize the desired adhesive gel precursor.

4.3.2 Synthesis of poly(ethylene glycol) diacrylamide (PEGDAAm)

The reaction scheme for the synthesis of Polyethylene glycol diacrylamide (PEGDAAm; MW, 3400) from polyethylene glycol (PEG) was adapted from Elbert et al. (Elbert and Hubbell, 2001). Anhydrous triethylamine (TEA, 6 molar excess to PEG, 34.4 mL, 0.2471 mol) was added to a solution of dry PEG (MW 3400, 140 g, 0.0412 mol) and 4-dimethylaminopyridine (DMAP, 0.1 molar equivalent to mesyl chloride, .0247 moles,

3.0183 g) in anhydrous dichloromethane (DCM, 150 mL) under argon. After mixing for 10 min, a concentrated solution of mesyl chloride (MsCl, 6 molar excess to PEG, 19.1 mL, 0.2471 mol) in DCM was added dropwise with rapid stirring. The reaction proceeded overnight under argon. PEG dimesylate was purified by filtering the solution through filter paper under vacuum, followed by precipitation in diethyl ether (1 L). The product was again filtered and dried under vacuum to yield PEG dimesylate. To synthesize PEG diamine from PEG dimesylate, the entire PEG dimesylate product was added to 800 mL 25% aqueous ammonia solution within 2 days of completing the previous reaction. The container was closed and sealed tightly with Parafilm, and the reaction proceeded for 4 days with vigorous stirring at room temperature. The container was then opened to atmosphere to allow the ammonia to evaporate over 3 days. To remove remaining ammonia, NaOH was used to raise the pH of the solution to 13, and the solution was extracted with DCM (1:5 DCM volume to ammonia solution) 3 times. The DCM washes were pooled and concentrated under rotary evaporation. The product was then precipitated in diethyl ether, filtered, and dried under vacuum. Yields were typically ~80%, and percent amination was 99% as verified by ^{1}H NMR for the characteristic peak (3.1 ppm) of the PEG methylene protons adjacent to the amine end group. To synthesize PEG diacrylamide from PEG diamine, anhydrous DCM (75 mL) was added to PEG diamine (70 g, .0206 mol) and stirred until the solution became clear. The mixture was cooled to 4 ºC on ice. To this cooled solution was added Diisopropylethylamine (DIPEA, 2 molar excess to PEG diamine, 5.7 mL, .0412 mol), followed by acryloyl chloride (4 molar excess to PEG diamine, 6.5 mL, 0.083 mol) dropwise with rapid stirring. The reaction proceeded overnight under argon protected from light and allowed to warm to room temperature. Aqueous reaction byproducts were removed by using aqueous 2M K_2CO_3 (2 molar excess to acryloyl chloride, 82.4 mL, 0.164 mol) to phase

separate the solution overnight. The lower organic phase was dried over $MgSO_4$ to remove residual aqueous solution, filtered, precipitated in diethyl ether and dried under vacuum to yield PEG diacrylamide. Yields were typically ~70%, and percent amidation was >90% as verified by ^{1}H NMR for the characteristic peaks (5.6, 6.1, and 6.3 ppm) of the vinyl protons on the acrylamide end groups. This scheme is given in Figure 4.2a.

4.3.3 Synthesis of MMP-sensitive PEGDAAm-peptide hydrogels

To make degradable photoactive hydrogel precursors, PEGDAAm was reacted in 1.6 molar excess with the collagenase-sensitive peptide CGPQGIWGQGCR (Aapptec, Louisville, KY; 95% pure by HPLC) by dissolution in sodium borate (100 mM, pH 9.0). The reaction was sterile filtered (0.22 μm PVDF membrane, Millipore, Billerica, MA), protected from light, and incubated at 37 ºC to yield macromers of the type acrylamide–PEG–(peptide–PEG)$_n$–acrylamide. Reaction products were dialyzed, frozen and lyophilized, and stored at −80 °C until use. This scheme and a schematic of the hydrogel mesh is shown in Figure 4.2b,c. MMP-sensitive PEGDAAm-based hydrogels were created by photopolymerization of aqueous solutions of PEGDAAm (10 wt%) and Acrylate-PEG-CGRGDS (10 mM) with 0.1% (w/v) Irgacure 2959 photoinitiator (I-2959, Ciba) at 100 mW/cm^2 (320 – 520 nm, 60 sec, EXFO).

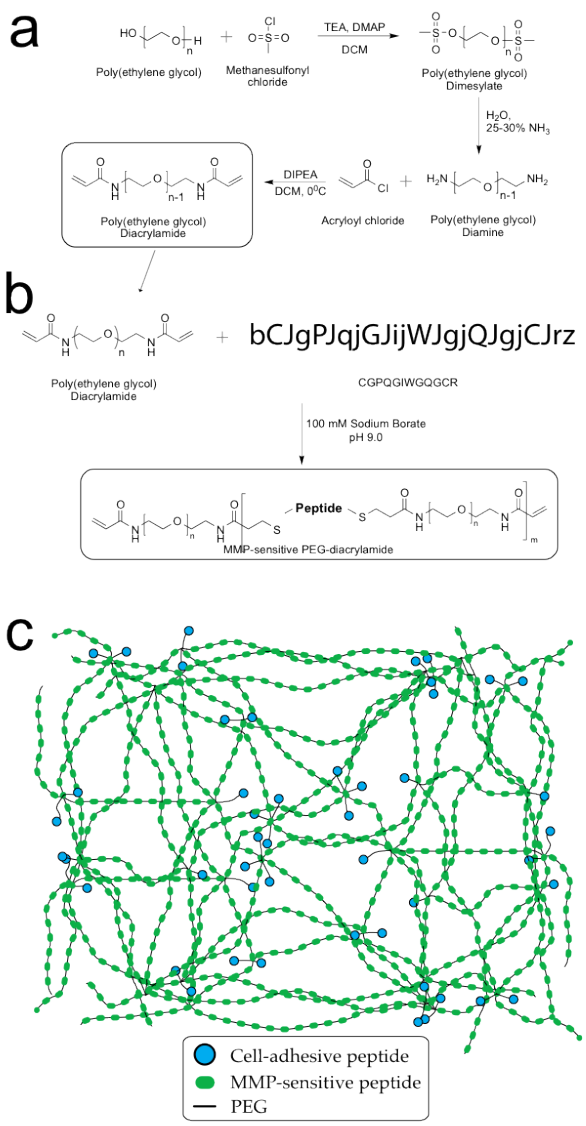

Figure 4.2. Synthesis scheme of MMP-degradable PEGDAAm gel precursor and gel architecture.

Detailed synthesis scheme of PEGDAAm (a) and the MMP-degradable gel precursor (b). (c) Schematic of hydrogel mesh network resulting from photopolymerization of MMP-sensitive PEGDAAm from (b) with cell-adhesive peptides conjugated to PEGDA and tethered as pendant chains. Image reprinted from (Miller et al., 2010).

4.3.4 Isolation of aortic arch tissue explants

Chick aortas were isolated from 12-day-old chick embryos (Charles River Labs, Preston, CT). Aortic arches were cleaned of excess fibroadipose tissue, sectioned into approximately 0.5 mm sized rings, and submerged inside a droplet of hydrogel prepolymer solution captured in the micropatterned molds as described in 4.3.5. Polymerization was performed for 60 seconds as described above, and culture media (EGM-2; 0.75 mL per hydrogel) was changed on day 1 and every 3 days thereafter. Hydrogels were photographed daily with oblique lighting phase contrast microscopy to optically exclude 2D cell migration on the surface of hydrogels and instead visualize only those cells which migrated in 3D within the hydrogels. The length of sprouts was measured manually using ImageJ.

4.3.5 Generation of micropatterned gels to guide aortic arch sprouts

PDMS molds were prepared as previously described (Yang et al., 2011). Briefly, SU-8 photoresist was spun onto silicon wafers in two layers to generate 100 μm tall channels and 800 μm tall central wells. Liquid 1:10 PDMS (ratio reflects curing agent to base) precursor was poured over the masters and cured. PDMS molds were sterilized in ethanol and UV prior to tissue encapsulation.

Prior to tissue encapsulation, the PDMS molds were placed over silane-acrylated glass coverslips. A drop gel precursor (MMP-degradable PEGDAAm and Acrylate-PEG-CGRGDS as decribed in 4.3.3) was placed over the central well in the PDMS mold. The PDMS mold with the PEG gel precursor over the central channel was then placed under vacuum. After the vacuum was released, the PEG precursor was then pulled into the channels. The arch explants were placed over the central channel prior to exposing the gel to UV for polymerization (as described in 4.3.3). The mold was then removed leaving

the patterned PEG gels with the arch on the coverslip. The gel-encapsulated arches were cultured in complete Endothelial Growth Medium-2 (EGM-2, Lonza).

4.4 Results

4.4.1 Synthesis of PEGDA and PEGDAAm Precursors

PEGDA yields were typically in the range 80-90% (~120 g), and percent acrylation was 99% as verified by ^{1}H NMR for the characteristic peak (4.32 ppm) of the PEG methylene protons adjacent to the acrylate (Mann et al., 2001b). Yields of PEG-diamine, a precursor to PEGDAAm, were typically ~80%, and percent amination was 99% as verified by ^{1}H NMR for the characteristic peak (3.1 ppm) of the PEG methylene protons adjacent to the amine end group. PEGDAAm yields were typically ~70%, and percent amidation was >90% as verified by ^{1}H NMR for the characteristic peaks (5.6, 6.1, and 6.3 ppm) of the vinyl protons on the acrylamide end groups (Figure 4.3). Protein conjugated gel precursors was confirmed and the MW characterized by gel permeation chromatography (GPC) (Miller et al., 2010).

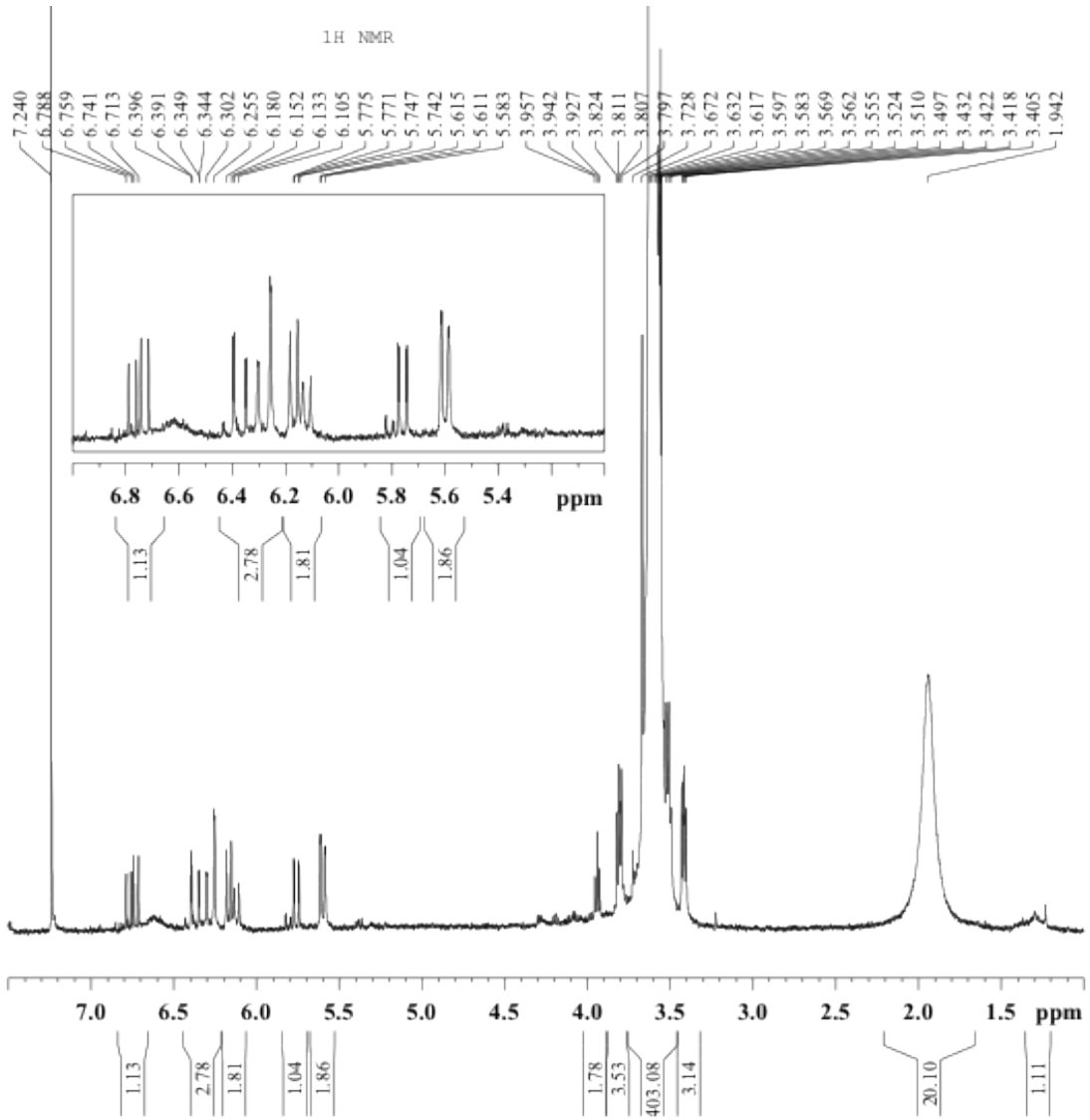

Figure 4.3. ^{1}H NMR Spectra of PEGDAAm.

Characteristic peaks of vinyl protons of acrylamide moiety confirm synthesis of PEGDAAm.

4.4.2 Generation of micropatterned gels to guide aortic arch sprouts

Bioactive PEG gels were successfully micromolded in various geometries to control angiogenic sprouting from aortic arch explants. Using microfabrication, PDMS

molds were bound to silanized coverslips in which the liquid gel precursor was aspirated into to form channels of defined widths. We sought to investigate whether channel geometries of these bioactive hydrogels determined sprouting velocity. Images of the micromolded gels are given in Figure 4.4. Arches were encapsulated at the base of defined PEGDAAm channels of various widths. During culture, the gels were imaged to measure sprouting lengths.

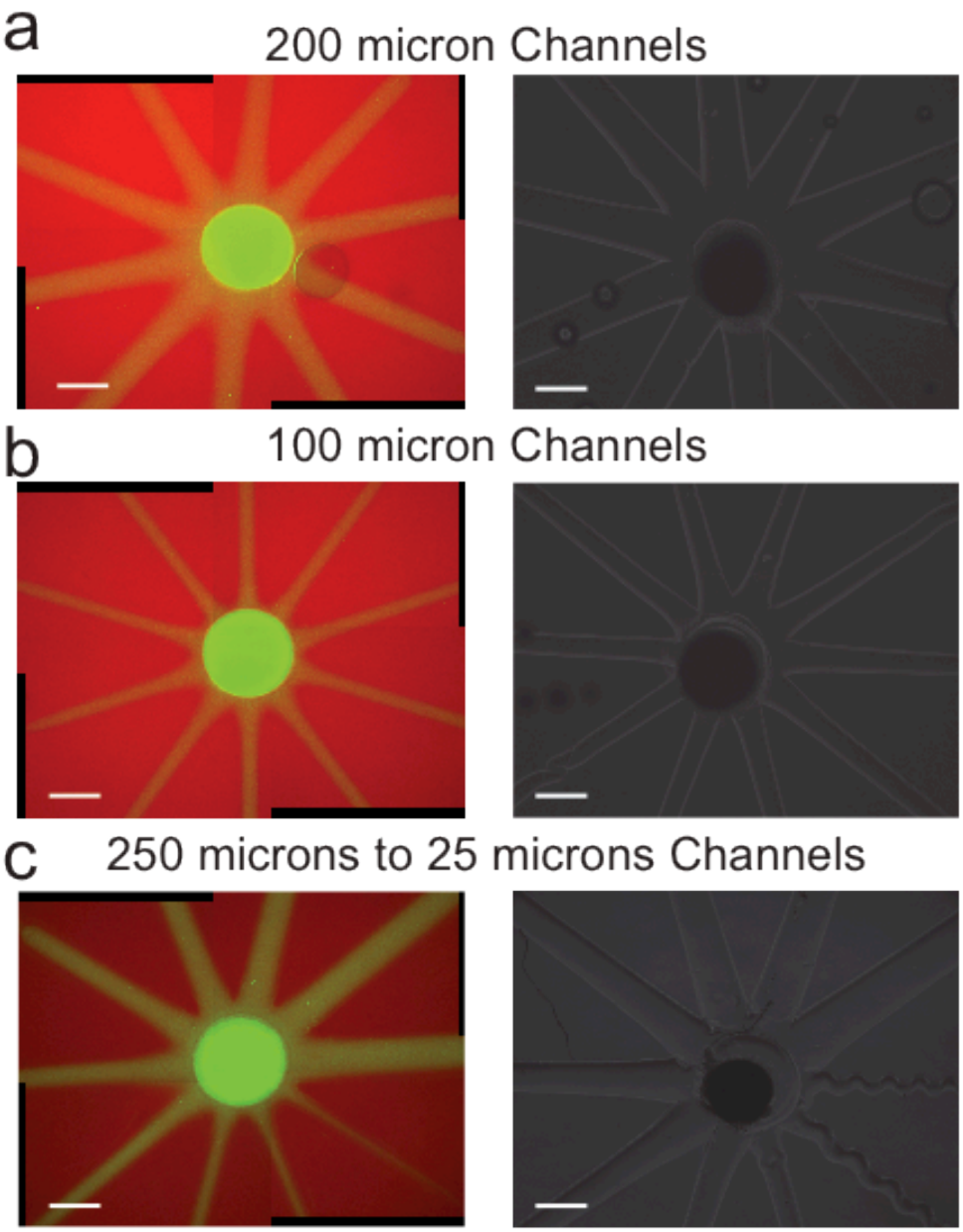

Figure 4.4. Micromolded bioactive PEG gels to pattern angiogenic sprouting. (Left column) Fluorescently labeled bioactive PEGDAAm gels (green) micromolded in radiating channels of 200 μm (a) 100 μm (b) and a range of channel diameters form 250 to 25 μM. (Right column) Aortic arch tissue explants encapsulated in bioactive gels. Scale bars 400 μm.

Arches embedded in these gels began sprouting when cultured in EGM-2. Angiogenic sprouts emerged from the explants over the course of several days. Sprouts in both 100 μm and 200 μm channels reached approximately a millimeter in length by day thirteen. However, by day fifteen, sprouts in the 100 μm channels began to reach higher sprouting velocity reaching nearly two millimeters by day nineteen (Figure 4.5).

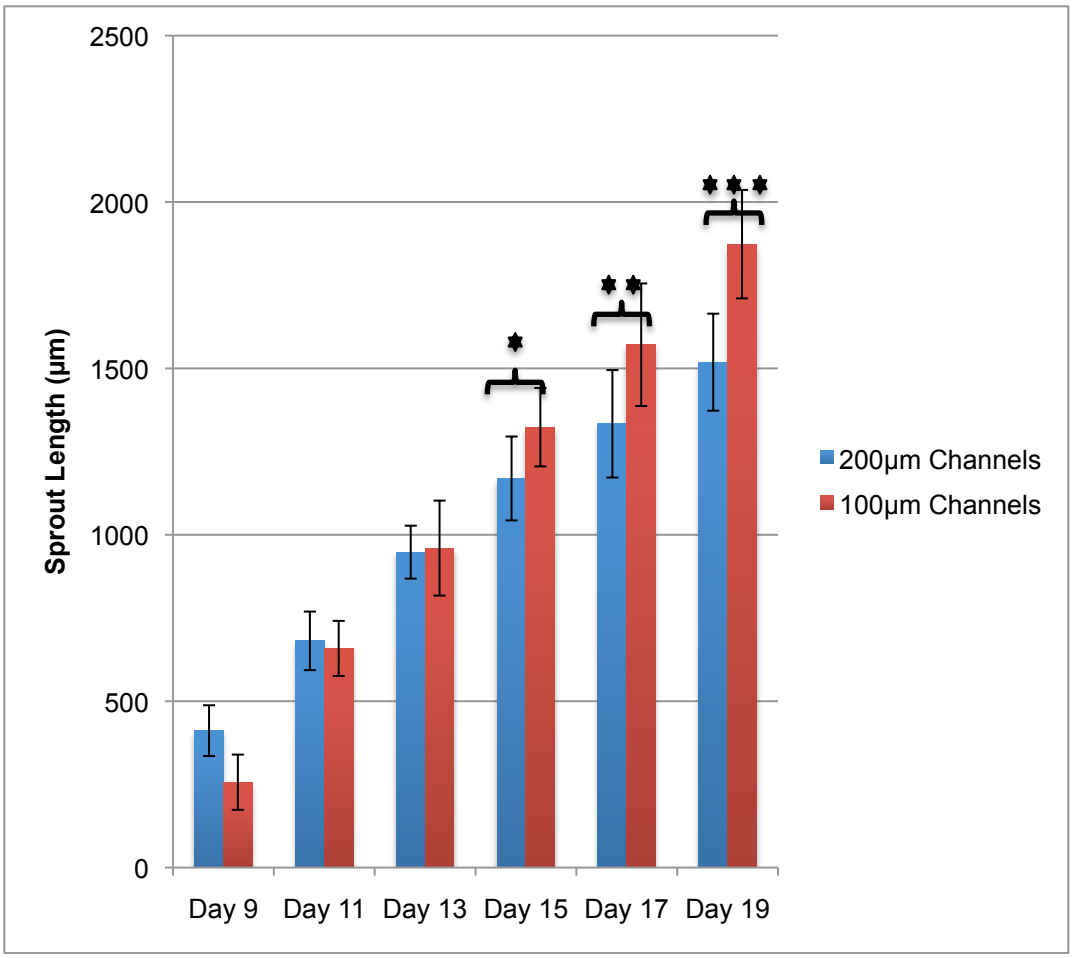

Figure 4.5. Sprouting lengths in different PEGDAAm width channels. Angiogenic sprout length over 19 days in culture in 100 μm and 200 μm channels. Sprouts in 100 μm channels reached nearly two millimeters by day nineteen compared to 1.5 millimeters in 200 μm channels. *p<0.05, **p<0.001, ***p<1e-4 (using Tukey's Test).

4.5 Discussion

In this section, we present a flexible hydrogel system to generate bioactive scaffolds. PEGDAAm step-wise growth polymers are MMP-degradable allowing encapsulated tissues to degrade and remodel these scaffolds and attach to pendant acrylate-PEG-RGD moieties. Furthermore, we presented a method to micromold patterns to study 3D geometry effects on angiogenic sprouting from aortic arch explants. This *ex vivo* assay in this synthetic matrix offers design considerations for tissue engineering scaffolds, which must be designed with vascularization in mind. We have shown that confining angiogenic sprouts to 100 μm hydrogel channels leads to more rapid sprout growth than 200 μm channels.

CHAPTER 5

Conclusions and Future Directions

In this work, we have proposed and developed a DNA-based force probe to measure cellular traction forces in real-time. We utilized the higher spatial resolution of this method to reveal that forces are located at the distal edges of focal adhesions. As an extension, we've shown that this method can be expanded to substrate geometries previously not amenable to force measurements. Then, we summarized the development of a bioactive PEG scaffold micromolded to pattern angiogenic sprouting.

While measurements of cellular forces obtained by bead displacements in gels and displacements of elastomeric posts have provided a great deal of insights into cellular force generation and their role in cellular functions, the work detailed here will provide pixel-resolution measurements of forces in real-time. Previous studies have coupled elastic worm-like chains and FRET probes to report forces across vinculin and EGFR (Grashoff et al., 2010; Stabley et al., 2012). The FPs developed here, by contrast, generate a much higher signal-to-noise ratio increase following unfolding, due to the substantial change in fluorescence as a function of fluorophore-quencher distance. Another recent study reports the tension required to irreversibly separate non-fluorescent DNA duplexes and detach cells from a surface, without visualizing the spatial distribution of force within adhesions (Wang and Ha, 2013). In relating the two studies, it is not clear whether the detachment forces reported in this work reflect the peak forces we observe in our adhesions, the mean force across adhesions, or an average force

over time experienced at a bound ligand. Thus, we believe both are distinct and likely complementary approaches.

Further, the understanding of DNA sequences and their impact on folding energetics enables the rational design of FPs for sensing force ranges of interest. While the investigation of DNA mechanics to date has largely been used to establish fundamental models of polymer physics, using these insights to now engineer DNA-based probes that report molecular forces may give rise to a new class of measurement tools. We envision that other (non-peptide) ligands can be coupled to the hairpin and used with the current approach, as long as the molecule does not unfold at a lower force than the hairpin.

In chapter two, we overviewed the development of our DNA force probes. We found that several modifications additional to the dye and quencher pair were needed to give viable cell attachment and signal. We found however that these modifications did not alter the molecular response of these probes to forces as measured previously (Woodside et al., 2006b) giving further credence to our contention that this method could lead to deliberate design of probes for a range of forces. There are some potential issues that other approaches may overcome. For instance, fluorescent-based probes are limited by irreversible photobleaching. Microscopy techniques and oxygen scavengers can minimize this problem, but other techniques are beginning to emerge such as plasmon coupling between metal nanoparticles, which is limited by the large particles needed but free from concerns of photobleaching (Sonnichsen et al., 2005). We found that the yield of the syntheses of these probes was in the 100 μg range. If yield or efficiency of peptide attachment to the oligonucleotides is an issue, newer chemical approaches, including the thiol-ester mediated Native Chemical Ligation (NCL) reaction performed for solid state synthesis, offers an alternative route to functionalize the

hairpins with the RGD peptide (Takeda et al., 2004). Finally, we only investigated constructing force probes with RGD as the integrin ligand. However, there are a range of adhesive peptides whose varied behaviors in regulating integrin activation are little understood (Staatz et al., 1991). In fact RGD is a relatively weak activator of integrins and future force probes including cyclic RGD would likely better activate cell forces as well as allowing a means to measure potential changes into the nature of forces generated (Kato and Mrksich, 2004).

In chapter three we described the methods found to best conjugate our force probes to glass surfaces and measure cellular traction forces. We found that the monofunctional silane-coupling scheme was the optimal approach to achieve low background signal and higher cell attachment. By stamping silane, we found that PDMS substrates could be functionalized with our force probes. We utilized this new setting to investigate the possible polarity of forces that cells exert when cultured on aligned μm-sized grooves in the surface. Pervious studies have demonstrated that cells align along such topographical cues, but other methods of traction force measurement are not amenable to these settings (Meyle et al., 1991). Coupling the FPs to a traditional TFM substrate would be highly beneficial towards validating this new approach by comparing the forces measured by the FPs with better-characterized measurements. So, we then tried to combine the mPAD and FP measurements. However, we found that these PDMS surfaces required plasma cleaning to achieve sufficient functionalization. This leads to an irreversible glass transition of the PDMS substrate (Ye et al., 2006). While we extended this technique to functionalize the PDMS micropost mPAD substrates to simultaneously measure cellular force using the FP fluorescence concurrently with post deflection, the posts did not show any measurable deflection despite FP fluorescence suggesting that the PDMS elastic modulus had irreversibly been altered (Figure 5.1).

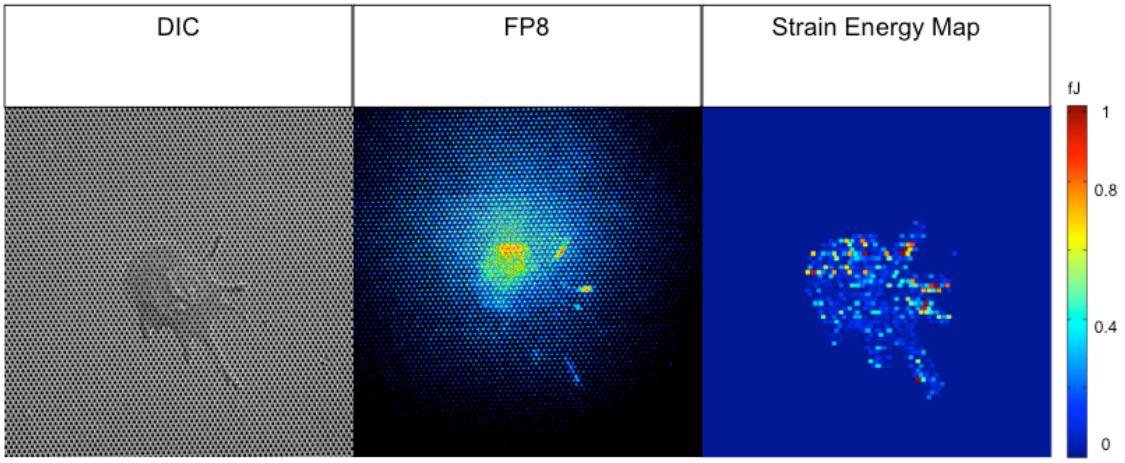

Figure 5.1. mPAD substrate functionalized with force probes.

DIC (left) and FP fluorescence (middle) images of a cell spread on mPAD substrates functionalized with FPs. The strain map (right) shows negligible displacement indicating that plasma treatment of posts led to glass transition of the posts.

As an alternative to stamping silanes, we sought a method to stamp proteins onto PDMS surfaces cleaned with an ultraviolet ozone (UVO) cleaner. UVO cleaning makes PDMS temporarily hydrophilic allowing proteins to be transferred from an inked stampe a standard method to constrain cell spreading to desired regions of a substrate (Tan et al., 2004; Tan et al., 2001). To achieve an analogous approach to using amino-silane, we stamped poly-l-lysine (PLL) into patterns and then reacted with the SM(PEG)$_2$ crosslinker and force probes as described in chapter two. We plated cells onto 250 μm x 250 μm square patterns of FP, and did observe pattern fidelity in terms of cell attachment and fluorescence (Figure 5.2). However, the background relative to the signal was high, and we abandoned this approach to patterning the FP onto PDMS. An alternative method to achieve the functionality of PDMS stamping with the force probes

would be to stamp an avidin protein and then react the FPs to a maleimide-tagged biotin for binding to the avidin surface.

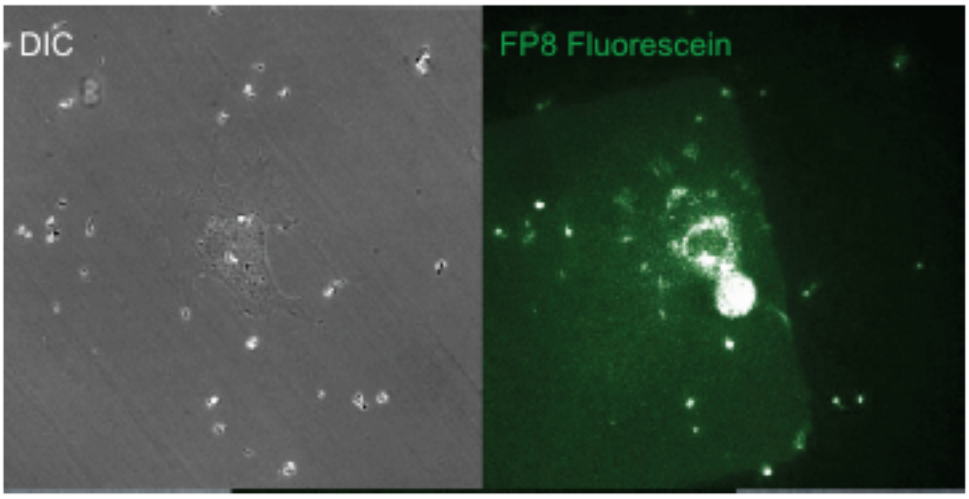

Figure 5.2. FP conjugated to stamped PLL patterns on PDMS.
DIC (left) and FP fluorescence (right) images of cells cultured on PDMS substrates stamped with 250 μm square patterns of PLL then reacted with $SM(PEG)_2$ then reacted with FP8 fluorescein.

By using the intensity of the fluorescence in each pixel, we estimated the number of open hairpins to give an approximation of the force. We measured peak tractions up to approximately 30 kPa, which is in line with the literature values on gels ranging from 0.5-10 kPa (Legant et al., 2013; Sabass et al., 2008). These scaled to 1000-5000 nN per cell and 10-150 pN per adhesion, and previous studies have found roughly 200-1200 nN per cell and 10-30 pN per adhesion (Fu et al., 2010). The discrepancies may be attributable to either the uncertainty in either measurement (whether from FPs, bead

displacements in gels, or micropost deflections) or the predicted increase in force that the cells would exert in our setting given that they are imaged on glass.

During live-cell imaging, any cellular medium containing serum completely rid the surface of FP fluorescence. Serum contains DNAse, and this is a major limitation to using DNA as a force probe. Adding DNAse to surfaces conjugated with FPs led to rapid loss of fluorescence and cell detachment. An alternative would be to use synthetic peptide nucleic acids as a foundation of the FPs as these are DNAse insensitive. Also, the FPs when unfolded lead to a rapid lengthening of the molecular conformation of the DNA and a temporary increase in the conformation length of the connection between the integrins and the cell surface. Such molecular details between the ECM and integrins has recently been shown to be crucial to mechanotransduction (Trappmann et al., 2012). Studying these potential complications further will be critical to fully ascertaining the effectiveness of FPs to measure cellular tractions neutrally without them in and of themselves affecting cell attachment.

To correlate the fluorescence intensity with a value of force in a given pixel, we estimated the number of fluorescing hairpins in a pixel by linearly interpolating the intensity from fluorescent BSA. The utility of using surface-bound molecular beacons to measure traction forces would surely be enhanced with a more mechanistic understanding of the relationship between force and intensity within a pixel. The hairpins under the duress of force would most likely unfold under mechanical load in a stochastic fashion similar to the studies by Woodside *et al*. Within a given pixel, we estimate that on the order of 10^2 hairpins are unfolded from traction forces in response to cellular force. Furthermore, while a given pixel intensity in an image may represent the total value of stress in the given pixel area, the forces are actually distributed among the many hairpins engaged by integrins. We can then imagine then that for some given total cell

traction force in a given pixel, this force is then dispersed stochastically among the engaged hairpins. We suggest that this total force within a pixel emerges as a probability density function of *molecular* forces that each hairpin experiences. Thus, for a given molecular force experienced by a hairpin, there is a corresponding frequency of hairpins experiencing this force as dictated by the probability density function. To illustrate this, a hypothetical probability density curve is shown in Figure 5.3.

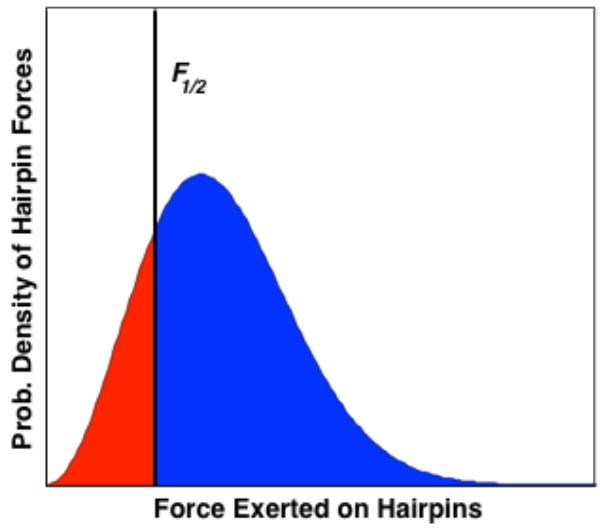

Figure 5.3. Hypothetical probability distribution of molecular forces on hairpins. Potential probability distribution of molecular forces on surface bound hairpins in response to cellular traction forces. For a given total cell force in a pixel, the hairpins experience a probabilistic distribution of forces at each integrin-bound force probe. The red region represents hairpins experiencing forces below the $F_{1/2}$ and thus below the detection limit. The blue region represents hairpins experiencing forces above the $F_{1/2}$ value, and only these hairpins would contribute to the fluorescent intensity.

To estimate the total force in the pixel, F_{Total}, we then must account for the number of hairpins experiencing each molecular force value F. To calculate the pixel force we would then need to integrate the probability density curve as follows

$$F_{Total} \propto \int_0^\infty F \cdot freq \, dF \tag{5.1}$$

where *freq* is the number of hairpins at a given molecular force F, and the entire force spectrum is considered. It is also reasonable to presume that the total force is proportional in some way to the fluorescent intensity

$$F_{Total} \propto I \tag{5.2}$$

where I is the fluorescent intensity of each pixel. However, as represented as the red region of the graph in Figure 5.3 the fluorescence of unfolded hairpins does not occur until the molecular force on a particular hairpin reaches $F_{1/2}$. This means that the lower levels of molecular force do not directly result in fluorescence. Thus the intensity of fluorescence is most likely of the integral form

$$I \propto \int_{F_{1/2}}^\infty freq \, dF \tag{5.3}$$

where the integral range only begins at the $F_{1/2}$ of the hairpin force probe.

While the scope of the present studies did not provide an explicit expression for the molecular force probability density distribution on particular hairpins for a given pixel force, we can suggest some possibilities and then consider the implications. For example, it is possible that the probability density function is some form of a Boltzmann distribution. Figure 5.4 shows some potential molecular force probability density curves and their alteration due to increases in total pixel force if they follow a Boltzmann distribution. The bottom panel shows the change in the integral of these curves to provide an estimate of change in fluorescence given a change in total force akin to Equation 5.3. Particularly of note is that this type of probability distribution would then

lead to a non-linear estimate of total force for a given intensity. However, there is a linear region of this relation near the origin also annotated on the graph. Since the relationship to force and intensity seems to be linear in our case (see Figure 3.9), it is also possible that we are measuring cellular traction forces in this linear region.

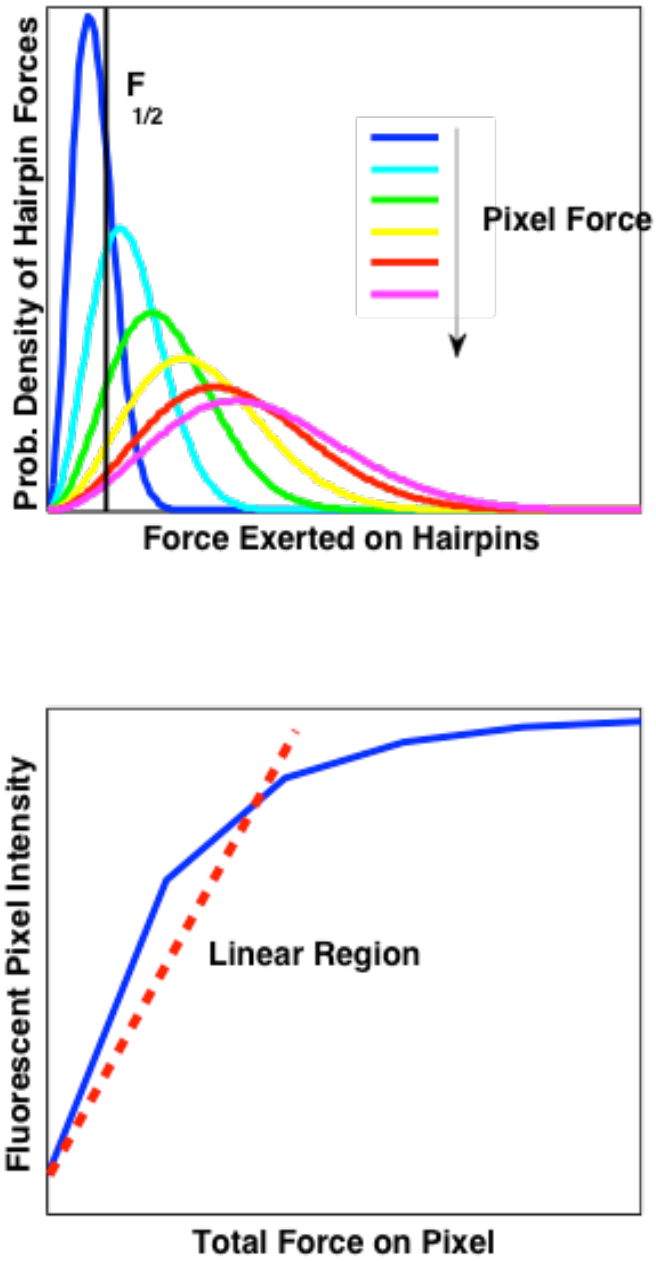

Figure 5.4. Change in fluorescent intensity if hairpins experience molecular forces as a Boltzmann distribution.

Top graph shows the probability distribution of molecular forces experienced by integrin –bound hairpins at given total pixel forces. The different colored curves represent how these probability distributions of molecular force would shift as the total pixel force

increases. Only hairpins experiencing forces above the $F_{1/2}$ value would contribute to the fluorescence. The bottom graph plots the change in fluorescent intensity, found by integrating the curves in the top graph from the $F_{1/2}$ at the lower bound to infinity. The global relationship between total force and fluorescent intensity is non-linear, but there exists a linear region near the origin.

However, another potential case is that of subsets of hairpins that unfold and fluoresce at different molecular forces during adhesion maturation. In this arrangement perhaps as the adhesion develops, engaged integrins exert higher and higher levels of force on their respective bound hairpin probes. We can then propose that as forces in a given pixel increase, there are hairpin subsets that experience increasing thresholds of force shown in Figure 5.5.In this arrangement the increase in fluorescence in response to total force is linear throughout the domain of forces. Future studies should examine these relations in detail and mechanistically describe how the force probes unfold stochastically in response to cellular traction forces.

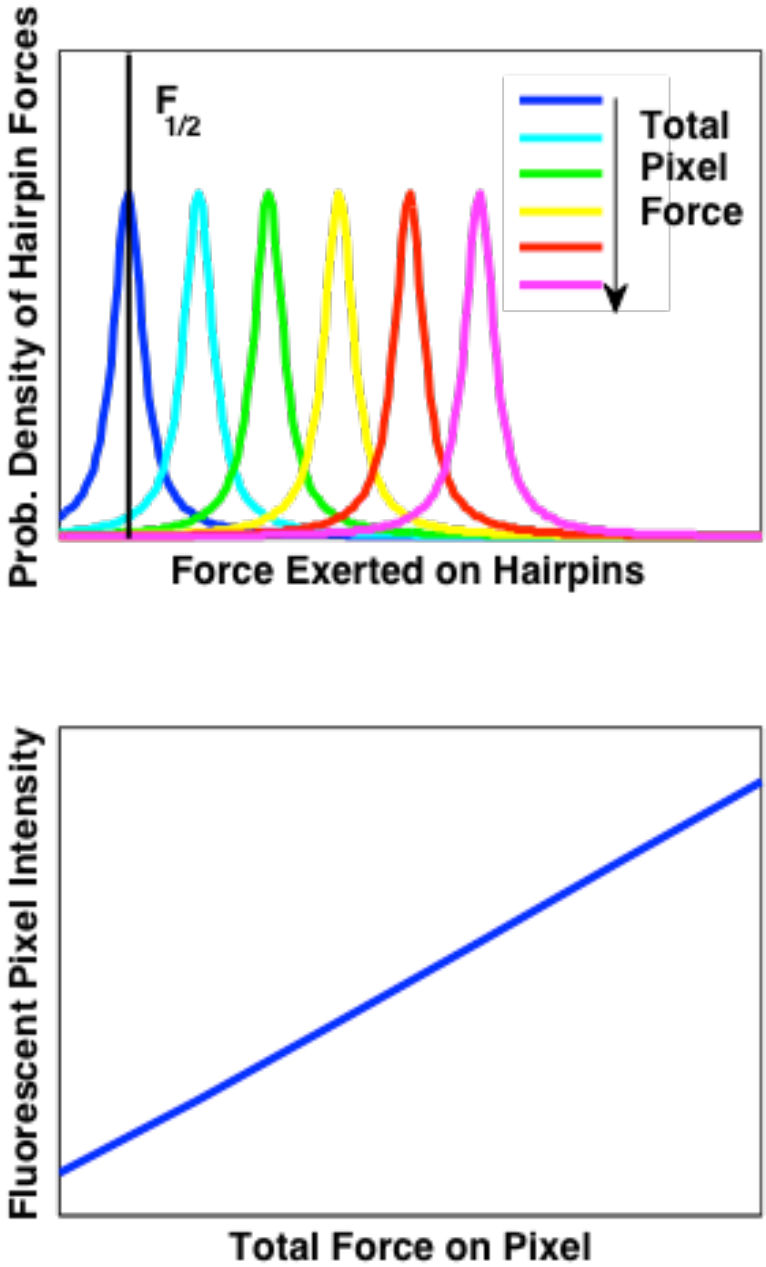

Figure 5.5. Change in fluorescent intensity if hairpins experience molecular forces as a different subsets.

Top graph shows the probability distribution of molecular forces experienced by integrin –bound hairpins at given total pixel forces. The different colored curves represent how these probability distributions of molecular force would shift as the total pixel force

increases. Only hairpins experiencing forces above the $F_{1/2}$ value would contribute to the fluorescence. The bottom graph plots the change in fluorescent intensity, found by integrating the curves in the top graph from the $F_{1/2}$ at the lower bound to infinity. The global relationship between total force and fluorescent intensity is linear.

Finally, by transfecting cells with fluorescently labeled proteins, we demonstrated that force is localized to the distal edge of focal adhesions. Another recent study has used TFM to show that tractions are located at the distal edge of FAs, and that FAs transition between stable and fluctuating states which are key for cellular durotaxis (Plotnikov et al., 2012). The report of distal forces in this study validates the observations reported by our methods, but it is noted that their 'high resolution traction force microscopy' method (Sabass et al., 2008) provides at best a 1 μm spatial resolution when no regularization is used and forces are highly localized. But no traction strain data gives a stable traction stress solution without some regularization, so the resolution actually is worse. Thus, even with distal forces previously reported, we contend that the new method offered here provides much higher spatial resolution and that we observed additional insights to focal adhesion structure not reported previously. Of note, is that while we measured a typical dislocation of the centroids of adhesion from the geometric center of traction forces to be ~200 nm, the authors in the 2012 study found a displacement of 1 μm. While these differences may be due to the relative strengths and weaknesses of the two force measurement methods, another possibility is due to the use of soft gels in the cited study (~10 kPA PA gels) compared to glass in our case.

In chapter 4, we presented a versatile hydrogel system to study angiogenesis in 3D environments. These gels are MMP-degradable as they incorporate PEGDAAm

monomers grown step-wise with bis-cysteine degradable peptide sequences. These gels also include pendant acrylate-PEG-CGRDS moieties to allow for cell adhesion. We used microfabrication technology to micromold these gels into defined channel widths to confine angiogenic sprouting from chick aortic arch explants. We found that 100 μm diameter hydrogel channels led to faster angiogenic sprouting than 200 μm diameter sprouting. This informs tissue-engineering strategies to accelerate the vascularization of *ex vivo* scaffolds.

BIBLIOGRAPHY

Adams, R.H., and Alitalo, K. (2007). Molecular regulation of angiogenesis and lymphangiogenesis. Nature Reviews Molecular Cell Biology *8*, 464-478.

Ahn, A., Frishman, W.H., Gutwein, A., Passeri, J., and Nelson, M. (2008). Therapeutic Angiogenesis A New Treatment Approach for Ischemic Heart Disease - Part II. Cardiol Rev *16*, 219-229.

Akbulatov, S., Tian, Y., and Boulatov, R. (2012). Force,ÄìReactivity Property of a Single Monomer Is Sufficient To Predict the Micromechanical Behavior of Its Polymer. Journal of the American Chemical Society *134*, 7620-7623.

Ali, M.B., Bessueille, F., Chovelon, J.M., Abdelghani, A., Jaffrezic-Renault, N., Maaref, M.A., and Martelet, C. (2008). Use of ultra-thin organic silane films for the improvement of gold adhesion to the silicon dioxide wafers for (bio)sensor applications. Materials Science and Engineering: C *28*, 628-632.

Anthony, P.C., Sim, A.Y.L., Chu, V.B., Doniach, S., Block, S.M., and Herschlag, D. (2012a). Electrostatics of Nucleic Acid Folding under Conformational Constraint. J Am Chem Soc *134*, 4607-4614.

Anthony, P.C., Sim, A.Y.L., Chu, V.B., Doniach, S., Block, S.M., and Herschlag, D. (2012b). Electrostatics of Nucleic Acid Folding under Conformational Constraint. Journal of the American Chemical Society *134*, 4607-4614.

Arnold, M., Cavalcanti-Adam, E.A., Glass, R., Blümmel, J., Eck, W., Kantlehner, M., Kessler, H., and Spatz, J.P. (2004). Activation of Integrin Function by Nanopatterned Adhesive Interfaces. ChemPhysChem *5*, 383-388.

Avraamides, C.J., Garmy-Susini, B., and Varner, J.A. (2008). Integrins in angiogenesis and lymphangiogenesis. Nature Reviews Cancer *8*, 604-617.

Azzaroni, O., Trappmann, B., van Rijn, P., Zhou, F., Kong, B., and Huck, W.T.S. (2006). Mechanically induced generation of counterions inside surface-grafted charged macromolecular films: Towards enhanced mechanotransduction in artificial systems. Angew Chem Int Edit *45*, 7440-7443.

Balaban, N.Q., Schwarz, U.S., Riveline, D., Goichberg, P., Tzur, G., Sabanay, I., Mahalu, D., Safran, S., Bershadsky, A., Addadi, L.*, et al.* (2001). Force and focal adhesion assembly: a close relationship studied using elastic micropatterned substrates. Nat Cell Biol *3*, 466-472.

Bell, S.E., Mavila, A., Salazar, R., Bayless, K.J., Kanagala, S., Maxwell, S.A., and Davis, G.E. (2001). Differential gene expression during capillary morphogenesis in 3D collagen matrices: regulated expression of genes involved in basement membrane matrix assembly, cell cycle progression, cellular differentiation and G-protein signaling. Journal of Cell Science *114*, 2755-2773.

Bellis, S.L., Miller, J.T., and Turner, C.E. (1995). Characterization of Tyrosine Phosphorylation of Paxillin in Vitro by Focal Adhesion Kinase. J Biol Chem *270*, 17437-17441.

Beningo, K.A., and Wang, Y.-L. (2002a). Flexible substrata for the detection of cellular traction forces. Trends in Cell Biology *12*, 79-84.

Beningo, K.A., and Wang, Y.L. (2002b). Flexible substrata for the detection of cellular traction forces. Trends Cell Biol *12*, 79-84.

Berrier, A.L., and Yamada, K.M. (2007). Cell–matrix adhesion. J Cell Physiol *213*, 565-573.

Bhadriraju, K., Yang, M., Alom Ruiz, S., Pirone, D., Tan, J., and Chen, C.S. (2007a). Activation of ROCK by RhoA is regulated by cell adhesion, shape, and cytoskeletal tension. Exp Cell Res *313*, 3616-3623.

Bhadriraju, K., Yang, M., Ruiz, S.A., Pirone, D., Tan, J., and Chen, C.S. (2007b). Activation of ROCK by RhoA is regulated by cell adhesion, shape, and cytoskeletal tension. Experimental Cell Research *313*, 3616-3623.

Bhatia, S.K., Hickman, J.J., and Ligler, F.S. (1992). New approach to producing patterned biomolecular assemblies. Journal of the American Chemical Society *114*, 4432-4433.

Bhushan, B., Hansford, D., and Lee, K.K. (2006). Surface modification of silicon and polydimethylsiloxane surfaces with vapor-phase-deposited ultrathin fluorosilane films for biomedical nanodevices. Journal of Vacuum Science & Technology A: Vacuum, Surfaces, and Films *24*, 1197-1202.

Blum, Y., Belting, H.G., Ellertsdottir, E., Herwig, L., Luders, F., and Affolter, M. (2008). Complex cell rearrangements during intersegmental vessel sprouting and vessel fusion in the zebrafish embryo. Dev Biol *316*, 312-322.

Bockelmann, U. (2004). Single-molecule manipulation of nucleic acids. Curr Opin Struct Biol *14*, 368-373.

Bunsow, J., Kelby, T.S., and Huck, W.T.S. (2010). Polymer Brushes: Routes toward Mechanosensitive Surfaces. Accounts Chem Res *43*, 466-474.

Burdick, J.A., Khademhosseini, A., and Langer, R. (2004). Fabrication of gradient hydrogels using a microfluidics/photopolymerization process. Langmuir *20*, 5153-5156.

Burridge, K., and Chrzanowska-Wodnicka, M. (1996). Focal adhesions, contractility, and signaling. Annu Rev Cell Dev Biol *12*, 463-518.

Burridge, K., and Wittchen, E.S. (2013). The tension mounts: stress fibers as force-generating mechanotransducers. J Cell Biol *200*, 9-19. doi: 10.1083/jcb.201210090.

Bustamante, C., Chemla, Y.R., Forde, N.R., and Izhaky, D. (2004). Mechanical processes in biochemistry. Annu Rev Biochem *73*, 705-748.

Calderwood, D.A., Campbell, I.D., and Critchley, D.R. (2013). Talins and kindlins: partners in integrin-mediated adhesion. Nature Reviews Molecular Cell Biology *14*, 503-517.

Cavalcanti-Adam, E.A., Volberg, T., Micoulet, A., Kessler, H., Geiger, B., and Spatz, J.P. (2007). Cell Spreading and Focal Adhesion Dynamics Are Regulated by Spacing of Integrin Ligands. Biophysical Journal *92*, 2964-2974.

Chen, C.S., Mrksich, M., Huang, S., Whitesides, G.M., and Ingber, D.E. (1997). Geometric Control of Cell Life and Death. Science *276*, 1425-1428.

Childs, S., Chen, J.N., Garrity, D.M., and Fishman, M.C. (2002). Patterning of angiogenesis in the zebrafish embryo. Development *129*, 973-982.

Choi, C.K., Vicente-Manzanares, M., Zareno, J., Whitmore, L.A., Mogilner, A., and Horwitz, A.R. (2008). Actin and alpha-actinin orchestrate the assembly and maturation of nascent adhesions in a myosin II motor-independent manner. Nat Cell Biol *10*, 1039-1050. doi: 1010.1038/ncb1763.

Cluzel, P., Lebrun, A., Heller, C., Lavery, R., Viovy, J.L., Chatenay, D., and Caron, F. (1996). DNA: An extensible molecule. Science *271*, 792-794.

Conroy, R.S., and Danilowicz, C. (2004). Unravelling DNA. Contemp Phys *45*, 277-302.

Coultas, L., Chawengsaksophak, K., and Rossant, J. (2005). Endothelial cells and VEGF in vascular development. Nature *438*, 937-945.

Craig, D., Krammer, A., Schulten, K., and Vogel, V. (2001). Comparison of the early stages of forced unfolding for fibronectin type III modules. P Natl Acad Sci USA *98*, 5590-5595.

Cukierman, E., Pankov, R., Stevens, D.R., and Yamada, K.M. (2001). Taking cell-matrix adhesions to the third dimension. Science *294*, 1708-1712.

Cumpston, B.H., Ananthavel, S.P., Barlow, S., Dyer, D.L., Ehrlich, J.E., Erskine, L.L., Heikal, A.A., Kuebler, S.M., Lee, I.Y.S., McCord-Maughon, D.*, et al.* (1999). Two-photon polymerization initiators for three-dimensional optical data storage and microfabrication. Nature *398*, 51-54.

Davis, D.A., Hamilton, A., Yang, J.L., Cremar, L.D., Van Gough, D., Potisek, S.L., Ong, M.T., Braun, P.V., Martinez, T.J., White, S.R.*, et al.* (2009). Force-induced activation of covalent bonds in mechanoresponsive polymeric materials. Nature *459*, 68-72.

DeForest, C.A., Polizzotti, B.D., and Anseth, K.S. (2009). Sequential click reactions for synthesizing and patterning three-dimensional cell microenvironments. Nature Materials *8*, 659-664.

Delanoe-Ayari, H., Rieu, J.P., and Sano, M. (2010). 4D Traction Force Microscopy Reveals Asymmetric Cortical Forces in Migrating Dictyostelium Cells. Phys Rev Lett *105*, 248103.

DeLong, S.A., Gobin, A.S., and West, J.L. (2005). Covalent immobilization of RGDS on hydrogel surfaces to direct cell alignment and migration. Journal of Controlled Release *109*, 139-148.

DeMali, K.A., Wennerberg, K., and Burridge, K. (2003). Integrin signaling to the actin cytoskeleton. Curr Opin Cell Biol *15*, 572-582.

Dembo, M., and Wang, Y.-L. (1999). Stresses at the Cell-to-Substrate Interface during Locomotion of Fibroblasts. Biophys J *76*, 2307-2316.

Denk, W., Strickler, J.H., and Webb, W.W. (1990). Two-photon laser scanning fluorescence microscopy. Science *248*, 73-76.

Deroanne, C.F., Lapiere, C.M., and Nusgens, B.V. (2001). In vitro tubulogenesis of endothelial cells by relaxation of the coupling extracellular matrix-cytoskeleton. Cardiovasc Res *49*, 647-658.

Desgrosellier, J.S., and Cheresh, D.A. (2010). Integrins in cancer: biological implications and therapeutic opportunities. Nat Rev Cancer *10*, 9-22.

Dike, L., Chen, C., Mrksich, M., Tien, J., Whitesides, G., and Ingber, D. (1999). Geometric control of switching between growth, apoptosis, and differentiation during angiogenesis using micropatterned substrates. In Vitro Cellular & Developmental Biology - Animal *35*, 441-448.

Dobrescu, G. (1998). Intercellular communication. Rev Med Chir Soc Med Nat Iasi *102*, 17-24.

Drake, C.J., Cheresh, D.A., and Little, C.D. (1995). An Antagonist of Integrin Alpha(V)Beta(3) Prevents Maturation of Blood-Vessels during Embryonic Neovascularization. Journal of Cell Science *108*, 2655-2661.

E. McGovern, M., and Thompson, M. (1998). Self-assembled silanes and the thiol functionalization of surfaces. Anal Commun *35*, 391-393.

Elbert, D.L., and Hubbell, J.A. (2001). Conjugate addition reactions combined with free-radical cross-linking for the design of materials for tissue engineering. Biomacromolecules *2*, 430-441.

Eliceiri, B.P., and Cheresh, D.A. (2001). Adhesion events in angiogenesis. Curr Opin Cell Biol *13*, 563-568.

Essevaz-Roulet, B., Bockelmann, U., and Heslot, F. (1997). Mechanical separation of the complementary strands of DNA. Proc Natl Acad Sci U S A *94*, 11935-11940.

Farge, E. (2003). Mechanical induction of twist in the Drosophila foregut/stomodeal primordium. Current Biology *13*, 1365-1377.

Folkman, J., and Moscona, A. (1978). Role of cell shape in growth control. Nature *273*, 345-349.

Fong, G.H. (2008). Mechanisms of adaptive angiogenesis to tissue hypoxia. Angiogenesis *11*, 121-140.

Fortuin, F.D., Vale, P., Losordo, D.W., Symes, J., DeLaria, G.A., Tyner, J.J., Schaer, G.L., March, R., Snell, R.J., Henry, T.D.*, et al.* (2003). One-year follow-up of direct myocardial gene transfer of vascular endothelial growth factor-2 using naked plasmid deoxyribonucleic acid by way of thoracotomy in no-option patients. Am J Cardiol *92*, 436-439.

Franck, C., Maskarinec, S.A., Tirrell, D.A., and Ravichandran, G. (2011). Three-Dimensional Traction Force Microscopy: A New Tool for Quantifying Cell-Matrix Interactions. PLoS ONE *6*, e17833.

Frieda, K.L., and Block, S.M. (2012). Direct Observation of Cotranscriptional Folding in an Adenine Riboswitch. Science *338*, 397-400.

Friedland, J.C., Lee, M.H., and Boettiger, D. (2009). Mechanically Activated Integrin Switch Controls alpha 5 Function. Science *323*, 642-644.

Friedlander, M., Brooks, P.C., Shaffer, R.W., Kincaid, C.M., Varner, J.A., and Cheresh, D.A. (1995). Definition of Two Angiogenic Pathways by Distinct alpha(v) Integrins. Science *270*, 1500-1502.

Fu, J., Wang, Y.K., Yang, M.T., Desai, R.A., Yu, X., Liu, Z., and Chen, C.S. (2010). Mechanical regulation of cell function with geometrically modulated elastomeric substrates. Nat Methods *7*, 733- 736.

Galbraith, C.G., and Sheetz, M.P. (1997). A micromachined device provides a new bend on fibroblast traction forces. P Natl Acad Sci USA *94*, 9114-9118.

Galbraith, C.G., Yamada, K.M., and Sheetz, M.P. (2002). The relationship between force and focal complex development. J Cell Biol *159*, 695-705.

Gardel, M.L., Kasza, K.E., Brangwynne, C.P., Liu, J., and Weitz, D.A. (2008). Mechanical response of cytoskeletal networks. Methods in cell biology *89*, 487-519.

Geiger, B., Spatz, J.P., and Bershadsky, A.D. (2009a). Environmental sensing through focal adhesions. Nature Reviews Molecular Cell Biology *10*, 21-33.

Geiger, B., Spatz, J.P., and Bershadsky, A.D. (2009b). Environmental sensing through focal adhesions. Nat Rev Mol Cell Biol *10*, 21-33.

Giannone, G.g., Dubin-Thaler, B.J., Rossier, O., Cai, Y., Chaga, O., Jiang, G., Beaver, W., Dbereiner, H.G., Freund, Y., Borisy, G.*, et al.* (2007). Lamellipodial Actin Mechanically Links Myosin Activity with Adhesion-Site Formation. Cell *128*, 561-575.

Gobin, A.S., and West, J.L. (2002). Cell migration through defined, synthetic extracellular matrix analogues. Faseb J *16*, 751-+.

Goldman, D. (2008). Theoretical Models of Microvascular Oxygen Transport to Tissue. Microcirculation *15*, 795-811.

Granger, H.J., Goodman, A.H., and Cook, B.H. (1975). Metabolic Models of Microcirculatory Regulation. Fed Proc *34*, 2025-2030.

Grashoff, C., Hoffman, B.D., Brenner, M.D., Zhou, R.B., Parsons, M., Yang, M.T., McLean, M.A., Sligar, S.G., Chen, C.S., Ha, T.*, et al.* (2010). Measuring mechanical tension across vinculin reveals regulation of focal adhesion dynamics. Nature *466*, 263-U143.

Greco, N.J., and Tor, Y. (2007). Synthesis and site-specific incorporation of a simple fluorescent pyrimidine. Nat Protoc *2*, 305-316.

Greenleaf, W.J., Woodside, M.T., Abbondanzieri, E.A., and Block, S.M. (2005). Passive All-Optical Force Clamp for High-Resolution Laser Trapping. Phys Rev Lett *95*, 208102.

Grieshaber, S.E., Farran, A.J.E., Lin-Gibson, S., Kiick, K.L., and Jia, X.Q. (2009). Synthesis and Characterization of Elastin-Mimetic Hybrid Polymers with Multiblock, Alternating Molecular Architecture and Elastomeric Properties. Macromolecules *42*, 2532-2541.

Hahn, M.S., Miller, J.S., and West, J.L. (2005). Laser scanning lithography for surface micropatterning on hydrogels. Adv Mater *17*, 2939.

Hahn, M.S., Miller, J.S., and West, J.L. (2006a). Three-dimensional biochemical and biomechanical patterning of hydrogels for guiding cell behavior. Adv Mater *18*, 2679.

Hahn, M.S., Taite, L.J., Moon, J.J., Rowland, M.C., Ruffino, K.A., and West, J.L. (2006b). Photolithographic patterning of polyethylene glycol hydrogels. Biomaterials *27*, 2519-2524.

Harris, A., Wild, P., and Stopak, D. (1980). Silicone rubber substrata: a new wrinkle in the study of cell locomotion. Science *208*, 177-179.

Hern, D.L., and Hubbell, J.A. (1998). Incorporation of adhesion peptides into nonadhesive hydrogels useful for tissue resurfacing. Journal of Biomedical Materials Research *39*, 266-276.

Hong, H.G., Jiang, M., Sligar, S.G., and Bohn, P.W. (1994). Cysteine-specific surface tethering of genetically engineered cytochromes for fabrication of metalloprotein nanostructures. Langmuir *10*, 153-158.

Hu, K., Ji, L., Applegate, K.T., Danuser, G., and Waterman-Stirer, C.M. (2007a). Differential transmission of actin motion within focal adhesions. Science *315*, 111-115.

Hu, K., Ji, L., Applegate, K.T., Danuser, G., and Waterman-Storer, C.M. (2007b). Differential transmission of actin motion within focal adhesions. Science *315*, 111-115.

Huang, S., Chen, C.S., and Ingber, D.E. (1998). Cell-shape-dependent central of cyclin D1, p27Kip and cell cycle progression in primary capillary endothelial cells. Mol Biol Cell *9*, 1755.

Hynes, R.O. (2009). The Extracellular Matrix: Not Just Pretty Fibrils. Science *326*, 1216-1219.

Ingber, D.E. (1990). fibronectin controls capillary endothelial-cell growth by modulating cell-shape. P Natl Acad Sci USA *87*, 3579-3583.

Ingber, D.E. (1997). Tensegrity: the architectural basis of cellular mechanotransduction. Annual Review of Physiology *59*, 575-599.

Ingber, D.E., and Folkman, J. (1989a). Mechanochemical switching between growth and differentiation during fibroblast growth factor-stimulated angiogenesis in vitro: role of extracellular matrix. J Cell Biol *109*, 317-330.

Ingber, D.E., and Folkman, J. (1989b). mechanochemical switching between growth and differentiation during fibroblast growth factor-stimulated angiogenesis in vitro - role of extracellular-matrix. J Cell Biol *109*, 317-330.

Ingber, D.E., Prusty, D., Sun, Z., Betensky, H., and Wang, N. (1995). Cell shape, cytoskeletal mechanics, and cell cycle control in angiogenesis. J Biomech *28*, 1471-1484.

Itoga, K., Yamato, M., Kobayashi, J., Kikuchi, A., and Okano, T. (2004a). Cell micropatterning using photopolymerization with a liquid crystal device commercial projector. Biomaterials *25*, 2047-2053.

Itoga, K., Yamato, M., Kobayashi, J., Kikuchi, A., and Okano, T. (2004b). Micropatterned surfaces prepared using a liquid crystal projector-modified photopolymerization device and microfluidics. J Biomed Mater Res A *69A*, 391-397.

Jain, R.K. (1999). Transport of molecules, particles, and cells in solid tumors. Annual Review of Biomedical Engineering *1*, 241-263.

Janmey, P.A., Winer, J.P., Murray, M.E., and Wen, Q. (2009). The hard life of soft cells. Cell Motil Cytoskeleton *66*, 597-605. doi: 510.1002/cm.20382.

Jeon, N.L., Baskaran, H., Dertinger, S.K.W., Whitesides, G.M., Van de Water, L., and Toner, M. (2002). Neutrophil chemotaxis in linear and complex gradients of interleukin-8 formed in a microfabricated device. Nat Biotechnol *20*, 826-830.

Jones, F.S., and Jones, P.L. (2000). The tenascin family of ECM glycoproteins: Structure, function, and regulation during embryonic development and tissue remodeling. Dev Dynam *218*, 235-259.

Kanchanawong, P., Shtengel, G., Pasapera, A.M., Ramko, E.B., Davidson, M.W., Hess, H.F., and Waterman, C.M. (2010a). Nanoscale architecture of integrin-based cell adhesions. Nature *468*, 580-584.

Kanchanawong, P., Shtengel, G., Pasapera, A.M., Ramko, E.B., Davidson, M.W., Hess, H.F., and Waterman, C.M. (2010b). Nanoscale architecture of integrin-based cell adhesions. Nature *468*, 580-U262.

Kato, M., and Mrksich, M. (2004). Using Model Substrates To Study the Dependence of Focal Adhesion Formation on the Affinity of Integrin,àíLigand Complexes,Ä†. Biochemistry-Us *43*, 2699-2707.

Khademhosseini, A., Yeh, J., Jon, S., Eng, G., Suh, K.Y., Burdick, J.A., and Langer, R. (2004). Molded polyethylene glycol microstructures for capturing cells within microfluidic channels. Lab Chip *4*, 425-430.

Kim, S.J., and Reneker, D.H. (1993). A Mechanochromic Smart Material. Polym Bull *31*, 367-374.

Klein, E.A., Yin, L.Q., Kothapalli, D., Castagnino, P., Byfield, F.J., Xu, T.N., Levental, I., Hawthorne, E., Janmey, P.A., and Assoian, R.K. (2009). Cell-Cycle Control by Physiological Matrix Elasticity and In Vivo Tissue Stiffening. Current Biology *19*, 1511-1518.

Kloxin, A.M., Kasko, A.M., Salinas, C.N., and Anseth, K.S. (2009). Photodegradable Hydrogels for Dynamic Tuning of Physical and Chemical Properties. Science *324*, 59-63.

Kniazeva, E., and Putnam, A.J. (2009). Endothelial cell traction and ECM density influence both capillary morphogenesis and maintenance in 3-D. Am J Physiol-Cell Ph *297*, C179-C187.

Kong, F., Garcia, A.J., Mould, A.P., Humphries, M.J., and Zhu, C. (2009). Demonstration of catch bonds between an integrin and its ligand. J Cell Biol *185*, 1275-1284.

Kumar, A., Larsson, O., Parodi, D., and Liang, Z. (2000). Silanized nucleic acids: a general platform for DNA immobilization. Nucleic Acids Res *28*, E71.

Kuzuya, M., Satake, S., Ai, S., Asai, T., Kanda, S., Ramos, M.A., Miura, H., Ueda, M., and Iguchi, A. (1998). Inhibition of angiogenesis on glycated collagen lattices. Diabetologia *41*, 491-499.

Lauffenburger, D.A., and Horwitz, A.F. (1996). Cell migration: a physically integrated molecular process. Cell *84*, 359-369.

Laukaitis, C.M., Webb, D.J., Donais, K., and Horwitz, A.F. (2001). Differential Dynamics of alpha-5 Integrin, Paxillin, and alpha-Actinin during Formation and Disassembly of Adhesions in Migrating Cells. The Journal of Cell Biology *153*, 1427-1440.

Lee, J., Leonard, M., Oliver, T., Ishihara, A., and Jacobson, K. (1994). Traction forces generated by locomoting keratocytes. The Journal of Cell Biology *127*, 1957-1964.

Lee, S.H., Moon, J.J., and West, J.L. (2008). Three-dimensional micropatterning of bioactive hydrogels via two-photon laser scanning photolithography for guided 3D cell migration. Biomaterials *29*, 2962-2968.

Legant, W.R., Choi, C.K., Miller, J.S., Shao, L., Gao, L., Betzig, E., and Chen, C.S. (2013). Multidimensional traction force microscopy reveals out-of-plane rotational moments about focal adhesions. Proceedings of the National Academy of Sciences *110*, 881-886.

Legant, W.R., Pathak, A., Yang, M.T., Deshpande, V.S., McMeeking, R.M., and Chen, C.S. (2009). Microfabricated tissue gauges to measure and manipulate forces from 3D microtissues. Proc Natl Acad Sci U S A *106*, 10097-10102.

Lenigk, R., Carles, M., Ip, N.Y., and Sucher, N.J. (2001). Surface Characterization of a Silicon-Chip-Based DNA Microarray. Langmuir *17*, 2497-2501.

Levental, K.R., Yu, H.M., Kass, L., Lakins, J.N., Egeblad, M., Erler, J.T., Fong, S.F.T., Csiszar, K., Giaccia, A., Weninger, W.*, et al.* (2009). Matrix Crosslinking Forces Tumor Progression by Enhancing Integrin Signaling. Cell *139*, 891-906.

Li, P.T.X., Collin, D., Smith, S.B., Bustamante, C., and Tinoco, I. (2006). Probing the mechanical folding kinetics of TAR RNA by hopping, force-jump, and force-ramp methods. Biophysical Journal *90*, 250-260.

Ling, T.G.I., Beck, M., Bunk, R., Forson, E., Tegenfeldt, J.O., Zakharov, A.A., and Montelius, L. (2003). Fabrication and characterization of a molecular adhesive layer for micro- and nanofabricated electrochemical electrodes. Microelectronic Engineering *67,68*, 887-892.

Liphardt, J., Onoa, B., Smith, S.B., Tinoco, I., Jr., and Bustamante, C. (2001). Reversible Unfolding of Single RNA Molecules by Mechanical Force. Science *292*, 733-737.

Liu, V.A., and Bhatia, S.N. (2002). Three-dimensional photopatterning of hydrogels containing living cells. Biomed Microdevices *4*, 257-266.

Lutolf, M.P. (2009). Integration column: Artificial ECM: expanding the cell biology toolbox in 3D. Integr Biol *1*, 235-241.

Lutolf, M.P., and Hubbell, J.A. (2003). Synthesis and physicochemical characterization of end-linked poly(ethylene glycol)-co-peptide hydrogels formed by Michael-type addition. Biomacromolecules *4*, 713-722.

Lutolf, M.P., and Hubbell, J.A. (2005). Synthetic biomaterials as instructive extracellular microenvironments for morphogenesis in tissue engineering. Nat Biotechnol *23*, 47-55.

Lutolf, M.R., Weber, F.E., Schmoekel, H.G., Schense, J.C., Kohler, T., Muller, R., and Hubbell, J.A. (2003). Repair of bone defects using synthetic mimetics of collagenous extracellular matrices. Nat Biotechnol *21*, 513-518.

Madan, R.A., and Dahut, W.L. (2009). Angiogenesis Inhibition in the Treatment of Prostate Cancer. Anti-Cancer Agents Med Chem *9*, 1070-1078.

Mammoto, A., Connor, K.M., Mammoto, T., Yung, C.W., Huh, D., Aderman, C.M., Mostoslavsky, G., Smith, L.E.H., and Ingber, D.E. (2009). A mechanosensitive transcriptional mechanism that controls angiogenesis. Nature *457*, 1103-U1157.

Mammoto, A., and Ingber, D.E. (2009). Cytoskeletal control of growth and cell fate switching. Curr Opin Cell Biol *21*, 864-870.

Mammoto, T., and Ingber, D.E. (2010). Mechanical control of tissue and organ development. Development *137*, 1407-1420.

Mann, B.K., Gobin, A.S., Tsai, A.T., Schmedlen, R.H., and West, J.L. (2001a). Smooth muscle cell growth in photopolymerized hydrogels with cell adhesive and proteolytically degradable domains: synthetic ECM analogs for tissue engineering. Biomaterials *22*, 3045-3051.

Mann, B.K., Gobin, A.S., Tsai, A.T., Schmedlen, R.H., and West, J.L. (2001b). Smooth muscle cell growth in photopolymerized hydrogels with cell adhesive and proteolytically degradable domains: synthetic ECM analogs for tissue engineering. Biomaterials *22*, 3045-3051.

Mann, B.K., Schmedlen, R.H., and West, J.L. (2001c). Tethered-TGF-beta increases extracellular matrix production of vascular smooth muscle cells. Biomaterials *22*, 439-444.

Mapili, G., Lu, Y., Chen, S.C., and Roy, K. (2005). Laser-layered microfabrication of spatially patterned functionalized tissue-engineering scaffolds. J Biomed Mater Res B *75B*, 414-424.

Martin, A.C., Kaschube, M., and Wieschaus, E.F. (2009). Pulsed contractions of an actin-myosin network drive apical constriction. Nature *457*, 495-U411.

Martino, M.M., Mochizuki, M., Rothenfluh, D.A., Rempel, S.A., Hubbell, J.A., and Barker, T.H. (2009). Controlling integrin specificity and stem cell differentiation in 2D and 3D environments through regulation of fibronectin domain stability. Biomaterials *30*, 1089-1097.

Mauriz, J.L., and Gonzalez-Gallego, J. (2008). Antiangiogenic drugs: Current knowledge and new approaches to cancer therapy. J Pharm Sci *97*, 4129-4154.

McBeath, R., Pirone, D.M., Nelson, C.M., Bhadriraju, K., and Chen, C.S. (2004). Cell Shape, Cytoskeletal Tension, and RhoA Regulate Stem Cell Lineage Commitment. Dev Cell *6*, 483-495.

Mertz, D., Vogt, C., Hemmerle, J., Mutterer, J., Ball, V., Voegel, J.C., Schaaf, P., and Lavalle, P. (2009). Mechanotransductive surfaces for reversible biocatalysis activation. Nature Materials *8*, 731-735.

Meyle, J., von Recum, A.F., Gibbesch, B., Hüttemann, W., Schlagenhauf, U., and Schulte, W. (1991). Fibroblast shape conformation to surface micromorphology. Journal of Applied Biomaterials *2*, 273-276.

Miller, J.S., Shen, C.J., Legant, W.R., Baranski, J.D., Blakely, B.L., and Chen, C.S. (2010). Bioactive hydrogels made from step-growth derived PEG-peptide macromers. Biomaterials.

Mironov, V., Boland, T., Trusk, T., Forgacs, G., and Markwald, R.R. (2003). Organ printing: computer-aided jet-based 3D tissue engineering. Trends in Biotechnology *21*, 157-161.

Miyamoto, S., Akiyama, S.K., and Yamada, K.M. (1995). Synergistic roles for receptor occupancy and aggregation in integrin transmembrane function. Science *267*, 883-885.

Moon, J.J., Hahn, M.S., Kim, I., Nsiah, B.A., and West, J.L. (2009). Micropatterning of poly(ethylene glycol) diacrylate hydrogels with biomolecules to regulate and guide endothelial morphogenesis. Tissue Eng Part A *15*, 579-585.

Mossa, A., Manosas, M., Forns, N., Huguet, J.M., and Ritort, F. (2009). Dynamic force spectroscopy of DNA hairpins: I. Force kinetics and free energy landscapes. J Stat Mech-Theory E, -.

Moulton, K.S. (2006). Angiogenesis in atherosclerosis: gathering evidence beyond speculation. Curr Opin Lipidology *17*, 548-555.

Nallicheri, R.A., and Rubner, M.F. (1991). Investigations of the Mechanochromic Behavior of Poly(Urethane Diacetylene) Segmented Copolymers. Macromolecules *24*, 517-525.

Nelson, C.M., Jean, R.P., Tan, J.L., Liu, W.F., Sniadecki, N.J., Spector, A.A., and Chen, C.S. (2005). Emergent patterns of growth controlled by multicellular form and mechanics. P Natl Acad Sci USA *102*, 11594-11599.

Neuman, K.C., and Block, S.M. (2004). Optical trapping. Rev Sci Instrum *75*, 2787-2809.

Ng, S.P., Billings, K.S., Ohashi, T., Allen, M.D., Best, R.B., Randles, L.G., Erickson, H.P., and Clarke, J. (2007). Designing an extracellular matrix protein with enhanced mechanical stability. Proc Natl Acad Sci U S A *104*, 9633-9637.

O'Donnell, M.J., Tang, K., Koster, H., Smith, C.L., and Cantor, C.R. (1997). High-density, covalent attachment of DNA to silicon wafers for analysis by maldi-tof mass spectrometry. Anal Chem *69*, 2438-2443. doi: 2410.1021/ac961007v.

Pandya, N.M., Dhalla, N.S., and Santani, D.D. (2006). Angiogenesis - a new target for future therapy. Vasc Pharmacol *44*, 265-274.

Parsons, J.T., Horwitz, A.R., and Schwartz, M.A. (2010). Cell adhesion: integrating cytoskeletal dynamics and cellular tension. Nat Rev Mol Cell Biol *11*, 633-643.

Pasapera, A.M., Schneider, I.C., Rericha, E., Schlaepfer, D.D., and Waterman, C.M. (2010). Myosin II activity regulates vinculin recruitment to focal adhesions through FAK-mediated paxillin phosphorylation. The Journal of Cell Biology *188*, 877-890.

Pelham, R.J., Jr., and Wang, Y. (1997). Cell locomotion and focal adhesions are regulated by substrate flexibility. Proc Natl Acad Sci USA *94*, 13661-13665.

Pirone, D.M., Liu, W.F., Ruiz, S.A., Gao, L., Raghavan, S., Lemmon, C.A., Romer, L.H., and Chen, C.S. (2006). An inhibitory role for FAK in regulating proliferation: a link between limited adhesion and RhoA-ROCK signaling. J Cell Biol *174*, 277-288.

Plotnikov, S.V., Pasapera, A.M., Sabass, B., and Waterman, C.M. (2012). Force Fluctuations within Focal Adhesions Mediate ECM-Rigidity Sensing to Guide Directed Cell Migration. Cell *151*, 1513-1527.

Pollard, T.D., and Borisy, G.G. (2003). Cellular motility driven by assembly and disassembly of actin filaments. Cell *112*, 453-465.

Provenzano, P.P., Inman, D.R., Eliceiri, K.W., and Keely, P.J. (2009). Matrix density-induced mechanoregulation of breast cell phenotype, signaling and gene expression through a FAK-ERK linkage. Oncogene *28*, 4326-4343.

Rauzi, M., Verant, P., Lecuit, T., and Lenne, P.F. (2008). Nature and anisotropy of cortical forces orienting Drosophila tissue morphogenesis. Nature Cell Biology *10*, 1401-U1457.

Revzin, A., Russell, R.J., Yadavalli, V.K., Koh, W.G., Deister, C., Hile, D.D., Mellott, M.B., and Pishko, M.V. (2001). Fabrication of poly(ethylene glycol) hydrogel microstructures using photolithography. Langmuir *17*, 5440-5447.

Ribas-Arino, J., Shiga, M., and Marx, D. (2009). Understanding Covalent Mechanochemistry. Angew Chem Int Edit *48*, 4190-4193.

Richardson, A., Malik, R.K., Hildebrand, J.D., and Parsons, J.T. (1997). Inhibition of cell spreading by expression of the C-terminal domain of focal adhesion kinase (FAK) is rescued by coexpression of Src or catalytically inactive FAK: a role for paxillin tyrosine phosphorylation. Molecular and Cellular Biology *17*, 6906-6914.

Rief, M., Clausen-Schaumann, H., and Gaub, H.E. (1999). Sequence-dependent mechanics of single DNA molecules. Nat Struct Biol *6*, 346-349.

Rogers, Y.H., Jiang-Baucom, P., Huang, Z.J., Bogdanov, V., Anderson, S., and Boyce-Jacino, M.T. (1999). Immobilization of oligonucleotides onto a glass support via disulfide bonds: A method for preparation of DNA microarrays. Anal Biochem *266*, 23-30.

Rosenbloom, J., Abrams, W.R., and Mecham, R. (1993). Extracellular-Matrix .4. The Elastic Fiber. Faseb J *7*, 1208-1218.

Ruoslahti, E., and Pierschbacher, M.D. (1986). Arg-Gly-Asp: A versatile cell recognition signal. Cell *44*, 517-518.

Sabass, B., Gardel, M.L., Waterman, C.M., and Schwarz, U.S. (2008). High Resolution Traction Force Microscopy Based on Experimental and Computational Advances. Biophys J *94*, 207-220.

Sanchez Carbayo, M., Bornmann, W., and Cordon Cardo, C. (2000). DNA Microchips: Technical and Practical Considerations. Current Organic Chemistry *4*, 945-971.

Santangelo, P.J. (2010). Molecular beacons and related probes for intracellular RNA imaging. Wiley Interdisciplinary Reviews: Nanomedicine and Nanobiotechnology *2*, 11-19.

Schaller, M.D., and Parsons, J.T. (1995). pp125FAK-dependent tyrosine phosphorylation of paxillin creates a high-affinity binding site for Crk. Molecular and Cellular Biology *15*, 2635-2645.

Sellers, J.R. (2000). Myosins: a diverse superfamily. Biochimica et Biophysica Acta (BBA) - Molecular Cell Research *1496*, 3-22.

Short, S.M., Talbott, G.A., and Juliano, R.L. (1998). Integrin-mediated signaling events in human endothelial cells. Mol Biol Cell *9*, 1969-1980.

Shroff, H., Reinhard, B.M., Siu, M., Agarwal, H., Spakowitz, A., and Liphardt, J. (2005). Biocompatible force sensor with optical readout and dimensions of 6 nm(3). Nano Lett *5*, 1509-1514.

Shroff, H., Sivak, D., Siegel, J.J., McEvoy, A.L., Siu, M., Spakowitz, A., Geissler, P.L., and Liphardt, J. (2008). Optical measurement of mechanical forces inside short DNA loops. Biophysical Journal *94*, 2179-2186.

Sieminski, A.L., Hebbel, R.P., and Gooch, K.J. (2004). The relative magnitudes of endothelial force generation and matrix stiffness modulate capillary morphogenesis in vitro. Experimental Cell Research *297*, 574-584.

Sigal, G.B., Mrksich, M., and Whitesides, G.M. (1998). Effect of Surface Wettability on the Adsorption of Proteins and Detergents. J Am Chem Soc *120*, 3464-3473.

Smith, M.L., Gourdon, D., Little, W.C., Kubow, K.E., Eguiluz, R.A., Luna-Morris, S., and Vogel, V. (2007). Force-induced unfolding of fibronectin in the extracellular matrix of living cells. Plos Biol *5*, 2243-2254.

Smith, S.B., Cui, Y.J., and Bustamante, C. (1996). Overstretching B-DNA: The elastic response of individual double-stranded and single-stranded DNA molecules. Science *271*, 795-799.

Smith, S.B., Finzi, L., and Bustamante, C. (1992). Direct Mechanical Measurements of the Elasticity of Single DNA-Molecules by Using Magnetic Beads. Science *258*, 1122-1126.

Sniadecki, N.J., Anguelouch, A., Yang, M.T., Lamb, C.M., Liu, Z., Kirschner, S.B., Liu, Y., Reich, D.H., and Chen, C.S. (2007). Magnetic microposts as an approach to apply forces to living cells. Proc Natl Acad Sci U S A *104*, 14553-14558.

Sniadecki, N.J., and Chen, C.S. (2007). Microfabricated silicone elastomeric post arrays for measuring traction forces of adherent cells. Methods Cell Biol *83*, 313-328.

Sonnichsen, C., Reinhard, B.M., Liphardt, J., and Alivisatos, A.P. (2005). A molecular ruler based on plasmon coupling of single gold and silver nanoparticles. Nat Biotech *23*, 741-745.

Staatz, W.D., Fok, K.F., Zutter, M.M., Adams, S.P., Rodriguez, B.A., and Santoro, S.A. (1991). Identification of a tetrapeptide recognition sequence for the alpha 2 beta 1 integrin in collagen. J Biol Chem *266*, 7363-7367.

Stabley, D.R., Jurchenko, C., Marshall, S.S., and Salaita, K.S. (2012). Visualizing mechanical tension across membrane receptors with a fluorescent sensor. Nat Methods *9*, 64-U172.

Strick, T.R., Croquette, V., and Bensimon, D. (2000). Single-molecule analysis of DNA uncoiling by a type II topoisomerase. Nature *404*, 901-904.

Stricker, J., Aratyn-Schaus, Y., Oakes, P.W., and Gardel, M.L. (2011). Spatiotemporal Constraints on the Force-Dependent Growth of Focal Adhesions. Biophys J *100*, 2883-2893.

Stricker, J., Sabass, B., Schwarz, U.S., and Gardel, M.L. (2010). Optimization of traction force microscopy for micron-sized focal adhesions. Journal of Physics: Condensed Matter *22*, 194104.

Su, S.C., Mendoza, E.A., Kwak, H.I., and Bayless, K.J. (2008). Molecular profile of endothelial invasion of three-dimensional collagen matrices: insights into

angiogenic sprout induction in wound healing. Am J Physiol-Cell Ph *295*, C1215-C1229.

Suh, K.Y., Seong, J., Khademhosseini, A., Laibinis, P.E., and Langer, R. (2004). A simple soft lithographic route to fabrication of poly(ethylene glycol) microstructures for protein and cell patterning. Biomaterials *25*, 557-563.

Sun, Z., Martinez-Lemus, L.A., Trache, A., Trzeciakowski, J.P., Davis, G.E., Pohl, U., and Meininger, G.A. (2005). Mechanical properties of the interaction between fibronectin and alpha(5)beta(1)-integrin on vascular smooth muscle cells studied using atomic force microscopy. Am J Physiol-Heart C *289*, H2526-H2535.

Takeda, S., Tsukiji, S., and Nagamune, T. (2004). Site-specific conjugation of oligonucleotides to the C-terminus of recombinant protein by expressed protein ligation. Bioorganic & Medicinal Chemistry Letters *14*, 2407-2410.

Tan, J.L., Liu, W., Nelson, C.M., Raghavan, S., and Chen, C.S. (2004). Simple approach to micropattern cells on common culture substrates by tuning substrate wettability. Tissue Eng *10*, 865-872.

Tan, J.L., Tien, J., and Chen, C.S. (2001). Microcontact Printing of Proteins on Mixed Self-Assembled Monolayers. Langmuir *18*, 519-523.

Tan, J.L., Tien, J., Pirone, D.M., Gray, D.S., Bhadriraju, K., and Chen, C.S. (2003). Cells lying on a bed of microneedles: an approach to isolate mechanical force. Proc Natl Acad Sci USA *100*, 1484-1489.

Tan, W., and Desai, T.A. (2003). Microfluidic patterning of cellular biopolymer matrices for biomimetic 3-D structures. Biomed Microdevices *5*, 235-244.

Tonra, J.R., and Hicklin, D.J. (2007). Targeting the vascular endothelial growth factor pathway in the treatment of human malignancy. Immunol Invest *36*, 3-23.

Trappmann, B., Gautrot, J.E., Connelly, J.T., Strange, D.G., Li, Y., Oyen, M.L., Cohen Stuart, M.A., Boehm, H., Li, B., Vogel, V.*, et al.* (2012). Extracellular-matrix tethering regulates stem-cell fate. Nat Mater *11*, 642-649. doi: 610.1038/nmat3339.

Tsang, V.L., Chen, A.A., Cho, L.M., Jadin, K.D., Sah, R.L., DeLong, S., West, J.L., and Bhatia, S.N. (2007). Fabrication of 3D hepatic tissues by additive photopatterning of cellular hydrogels. Faseb J *21*, 790-801.

Tyagi, S., and Kramer, F.R. (1996). Molecular Beacons: Probes that Fluoresce upon Hybridization. Nat Biotech *14*, 303-308.

Uehata, M., Ishizaki, T., Satoh, H., Ono, T., Kawahara, T., Morishita, T., Tamakawa, H., Yamagami, K., Inui, J., Maekawa, M.*, et al.* (1997). Calcium sensitization of smooth muscle mediated by a Rho-associated protein kinase in hypertension. Nature *389*, 990-994.

Vailhé, B., Ronot, X., Tracqui, P., Usson, Y., and Tranqui, L. (1997). In vitro angiogenesis is modulated by the mechanical properties of fibrin gels and is related to αvβ3 integrin localization In Vitro Cellular and Developmental Biology - Animal *33*, 763-773.

van Weel, V., van Tongeren, R.B., van Hinsbergh, V.W.M., van Bockel, J.H., and Quax, P.H.A. (2008). Vascular growth in ischemic limbs: A review of mechanisms and possible therapeutic stimulation. Ann Vasc Surg *22*, 582-597.

Vicente-Manzanares, M., Webb, D.J., and Horwitz, A.R. (2005). Cell migration at a glance. Journal of Cell Science *118*, 4917-4919.

Wang, X., and Ha, T. (2013). Defining Single Molecular Forces Required to Activate Integrin and Notch Signaling. Science *340*, 991-994.

Weibel, D.B., DiLuzio, W.R., and Whitesides, G.M. (2007). Microfabrication meets microbiology. Nat Rev Microbiol *5*, 209-218.

West, J.L., and Hubbell, J.A. (1999). Polymeric biomaterials with degradation sites for proteases involved in cell migration. Macromolecules *32*, 241-244.

Woodside, M.T., Anthony, P.C., Behnke-Parks, W.M., Larizadeh, K., Herschlag, D., and Block, S.M. (2006a). Direct measurement of the full, sequence-dependent folding landscape of a nucleic acid. Science *314*, 1001-1004.

Woodside, M.T., Behnke-Parks, W.M., Larizadeh, K., Travers, K., Herschlag, D., and Block, S.M. (2006b). Nanomechanical measurements of the sequence-dependent folding landscapes of single nucleic acid hairpins. Proc Natl Acad Sci USA *103*, 6190-6195.

Woodside, M.T., Garcia, C.M., and Block, S.M. (2008). Folding and unfolding single RNA molecules under tension. Current Opinion in Chemical Biology *12*, 640-646.

Yang, M.T., Fu, J., Wang, Y.-K., Desai, R.A., and Chen, C.S. (2011). Assaying stem cell mechanobiology on microfabricated elastomeric substrates with geometrically modulated rigidity. Nat Protoc *6*, 187-213.

Ye, H., Gu, Z., and Gracias, D.H. (2006). Kinetics of Ultraviolet and Plasma Surface Modification of Poly(dimethylsiloxane) Probed by Sum Frequency Vibrational Spectroscopy. Langmuir *22*, 1863-1868.

Yee, J.K., Parry, D.B., Caldwell, K.D., and Harris, J.M. (1991). Modification of quartz surfaces via thiol-disulfide interchange. Langmuir *7*, 307-313.

Zaidel-Bar, R., Itzkovitz, S., Ma'ayan, A., Iyengar, R., and Geiger, B. (2007). Functional atlas of the integrin adhesome. Nature Cell Biology *9*, 858-868.

Zhang, X., Jiang, G., Cai, Y., Monkley, S.J., Critchley, D.R., and Sheetz, M.P. (2008). Talin depletion reveals independence of initial cell spreading from integrin activation and traction. Nat Cell Biol *10*, 1062-1068.

Zhuang, S.L., Peng, Q., Cao, Y., and Li, H.B. (2009). Modulating the Mechanical Stability of Extracellular Matrix Protein Tenascin-C in a Controlled and Reversible Fashion. J Mol Biol *390*, 820-829.

Zimmermann, J.L., Nicolaus, T., Neuert, G., and Blank, K. (2010a). Thiol-based, site-specific and covalent immobilization of biomolecules for single-molecule experiments. Nat Protocols *5*, 975-985.

Zimmermann, J.L., Nicolaus, T., Neuert, G., and Blank, K. (2010b). Thiol-based, site-specific and covalent immobilization of biomolecules for single-molecule experiments. Nat Protoc *5*, 975-985.

Zipfel, W.R., Williams, R.M., and Webb, W.W. (2003). Nonlinear magic: multiphoton microscopy in the biosciences. Nat Biotechnol *21*, 1368-1376.